Modeling the Impact of Fuel Composition on Aircraft Engine NO_x, CO and Soot Emissions

by

Lukas Frederik Jakob Brink

Submitted to the Department of Aeronautics and Astronautics
in partial fulfillment of the requirements for the degree of

Master of Science in Aeronautics and Astronautics

at the

MASSACHUSETTS INSTITUTE OF TECHNOLOGY

September 2020

© Massachusetts Institute of Technology 2020. All rights reserved.

Author .....
Department of Aeronautics and Astronautics
June 25, 2020

Certified by .....
Steven R. H. Barrett
Professor of Aeronautics and Astronautics
Thesis Supervisor

Accepted by .....
Zoltán S. Spakovszky
Professor of Aeronautics and Astronautics
Chair, Graduate Program Committee

Modeling the Impact of Fuel Composition on Aircraft Engine NO_x, CO and Soot Emissions

by

Lukas Frederik Jakob Brink

Submitted to the Department of Aeronautics and Astronautics
on June 25, 2020, in partial fulfillment of the
requirements for the degree of
Master of Science in Aeronautics and Astronautics

Abstract

Aircraft NO_x, CO and soot emissions contribute to climate change and lead to negative air quality impacts. With the aim of quantifying the effects of fuel composition on NO_x, CO and soot emissions, a combustor model named Pycaso is developed.

The combustor model consists of a 0D/1D reactor network, coupled with a soot model. The model predicts NO_x, CO and soot emissions at sea level conditions for a CFM56-7B engine using conventional jet fuel. The model matches existing methods to predict cruise NO_x emissions within 5% and cruise CO emissions within 30%. It is shown that the volume — and thus time — over which secondary air is mixed with the fuel-air mixture in the combustor is the most important factor in determining the magnitudes of the modeled emissions. The sensitivity of modeled NO_x and CO emissions to thrust at thrust settings below 15% is shown to be the consequence of "cold" unburned fuel entering the secondary zone of the combustor.

The model is used to assess two possible emission mitigation solutions: removing naphthalene from jet fuel and replacing conventional jet fuel with 50:50 biofuel blends. The removal of naphthalene through hydrotreating is found to lead to mean reductions in soot emissions of 15% [12%–20%] for mass and 9% [5%–19%] for number. The range captures variations in engine operating conditions, soot model configurations and compositions of the baseline jet fuel. Similarly, the removal of naphthalene through extractive distillation reduces soot mass emissions by 32% [29%–48%] and number emissions by 23% [14%–45%]. The mean reductions associated with using 50:50 biofuel blends are 43% [34%–59%] for soot mass and 35% [14%–45%] for soot number. Using biofuel blends is also predicted to result in a reduction in NO_x emissions of 5% [4%–7%] and a 3% [2%–4%] decrease in CO emissions.

Thesis Supervisor: Steven R. H. Barrett
Title: Professor of Aeronautics and Astronautics

Acknowledgments

To my parents, Corry and Martin, and my brother, Thomas: thank you for all your support and for always being there for me.

I would like to thank my advisor, Steven, for his confidence, support and guidance over the past two years.

I would like to thank my supervisor, Ray, for everything he taught me about combustors, Cantera and research in general.

I would like to thank Prashanth, for his collaboration and the countless hours of brainstorming combustor design ideas together.

I would like to say "dankjewel" to Wouter and Vincent, for their ideas, support and feedback on this thesis.

I would like to thank my flatmates and friends Matt, Ondrej and Josh, for all the cookies, cocktails and banana cake.

I would like to thank my friends in the Laboratory for Aviation and the Environment: Inés, Haofeng, Wilhelm, Laurens, Guillaume, Carla, Akshat, Thibaud, Grace, Cassandre, Stewart, Walter, Yash, Nico, Arthur, Ruoyu, TJ and Nick. Thank you all for making our lab such a great place.

Contents

Chapter 1

Introduction

Air traffic revenue passenger kilometers (RPK) has doubled over the past twenty years and, not taking into account major disturbances, is expected to do so again over the next 15-20 years [1]. This increase in air travel also leads to an increase in aircraft emissions. These emissions primarily consist of carbon dioxide (CO_2), water (H_2O), unburned hydrocarbons (UHC), sulfur oxides (SO_x), nitrogen oxides (NO_x), carbon monoxide (CO) and soot. Through their direct and indirect effects, aircraft emissions are responsible for approximately 4% of the total radiative forcing (RF) induced by humans [2]. Furthermore, aircraft emissions negatively impact (surface) air quality, leading to an estimated ∼16,000 premature mortalities annually [3]. In order to reduce these emissions, it is important to understand how they respond to changes in combustor design and fuel composition. This research aims to provide a better understanding of the formation processes of NO_x, CO and soot as well as to quantify the effect of combustor design and fuel composition.

1.1 NO_x and CO Emissions

1.1.1 Background

NO_x emissions leaving the engine are 90% NO during cruise [4]. NO is formed in hot regions of the combustor (temperatures higher than 1850 K) [5]. NO_x emissions

increase with thrust and range from approximately 4 g/kg_{fuel} at idle to over 20 g/kg_{fuel} at maximum rated thrust [6].

CO forms as a result of incomplete combustion inside the combustion chamber of the engine [5]. In contrast to NO_x emissions, CO emissions decrease with increasing thrust and range from over 40 g/kg_{fuel} at idle to below 1 g/kg_{fuel} at maximum rated thrust [6]. The emissions quantity of a species in g/kg_{fuel} is referred to as the emission index (EI).

1.1.2 Impacts of NO_x and CO Emissions

Aircraft NO_x emissions cause tropospheric ozone formation and methane depletion, both greenhouse gases [7]. Aircraft NO_x emissions are the main anthropogenic source of ozone in the upper troposphere and are thought to be responsible for approximately 12% of ozone between altitudes of 8 and 12 km [4, 8]. The formation of ozone and depletion of methane due to aviation NO_x emissions have been estimated to result in net RF of 23 mW/m^2 and -14 mW/m^2, respectively, causing a net warming effect [9].

The ozone production attributable to aviation emissions also leads to negative air quality impacts and is estimated to result in ∼6800 premature mortalities per year [4].

The environmental impact of CO emissions is primarily through affecting air quality near airports since CO emissions predominantly occur at low thrust conditions [7, 10].

1.1.3 Reducing NO_x and CO Emissions

The focus of aircraft engine development over the last three decades has been on reducing the fuel consumption (and therefore CO_2 emissions) and noise impacts [11]. While manufacturers have made major progress in doing so (over 50% reductions for both), the fleet average EI NO_x has increased by approximately 14% over the same period [1, 12–14]. This effect can be ascribed to the use of higher overall pressure ratios (OPR) for increased engine thermal efficiency and the associated higher combustor

peak temperatures, which lead to higher NO_x emissions [15]. A 1%–2% decrease in CO_2 emissions achieved through increases in overall pressure ratio has been estimated to cause a 20% increase in EI NO_x [15, 16].

However, regulations set by the International Civil Aviation Organization (ICAO), providing upper limits for both NO_x and CO emissions during landing and takeoff (LTO), are becoming increasingly stringent [11]. ICAO regulations follow the technology goals set by the ICAO's Committee on Aviation Environmental Protection (CAEP) [17]. The current recommendation for 2027 is a 54% reduction in LTO NO_x emissions with respect to CAEP/8 [17].

These reductions in LTO NO_x emissions would have to be achieved along with future improvements in fuel efficiencies which are expected to focus on increasing the OPR and turbine inlet temperature [17]. Higher OPR and turbine inlet temperatures cause an increase in LTO NO_x emissions [17]. Whereas the LTO-based NO_x goals are dependent on OPR, no direct dependence on turbine inlet temperature is used. CAEP has recommended that future LTO NO_x should be based on a methodology reflecting both the dependence on OPR and turbine inlet temperature.

A model able to predict NO_x and CO emissions for both the LTO cycle as well as cruise, based on the OPR, turbine inlet temperature, engine design and combustor design, could quantify the potential of changing combustor designs and fuel compositions [17]. It could therefore be used in developing regulations, as well as in the development of engines complying with them.

1.2 Soot Emissions

1.2.1 Background

Soot is a solid substance consisting of a mixture of carbon and hydrogen with typical carbon-to-hydrogen (C/H) molar ratios between 8.3 and 18.3 [18]. It is formed during incomplete combustion processes, for example in parts of the combustor where air and fuel are poorly mixed [19]. Soot is also referred to as black carbon (BC) because of its

dark appearance. Soot particles are built up of necklace-like agglomerates, which are branched chains of spherical or near-spherical particles with diameters of 10–60 nm [20–23]. Soot falls in the category of non-volatile particulate matter (nvPM) and is the main nvPM found in aircraft engine emissions, as emissions of other nvPM such as metal particles are currently thought to be negligible [19]. Therefore, the terms soot, BC and nvPM will be used interchangeably in the following.

1.2.2 Impacts of Soot Emissions

The impacts of soot can be divided into three categories: air quality and health impacts, climate impacts, and engine performance impacts.

Starting with air quality and health impacts, soot particles fall in the category of $PM_{2.5}$ (diameter$<$2.5 µm), and, more specifically, belong to the group of ultrafine particulate matter (diameter$<$0.1 µm) [24, 25]. Research suggests that, due their small diameter ($<$0.1 µm) and high mass percentage of carbon, the toxicity of soot is up to a factor of ten higher than for other $PM_{2.5}$ species [26–28]. Evidence shows that soot particles result in an increased health risk and are associated with respiratory and cardiovascular disease, birth defects and cancer [29].

The climate impacts of soot emissions can be divided into two subcategories. First, soot particles absorb solar radiation causing a positive RF [30]. This positive RF is enhanced by the increased lifetime (up to ten days) of soot at altitude compared to soot near the surface [31–33]. The total direct RF of soot has been estimated to be approximately 2.5-9.5 mW/m^2, compared to a total aviation-attributable RF (without cirrus) of approximately 50 mW/m^2 [9, 30, 32, 34]. Second, soot particles provide nuclei for contrail formation in the wake of the aircraft [25]. Water vapor first condenses on the soot particles and then freezes, leading to the formation of contrail cirrus [35]. These clouds cause a net warming effect and they may be the most important radiative forcing contributor of aviation, their contribution to warming thus exceeding the effect of CO_2 emissions [36–38]. As a consequence of the rapid growth of aviation and a shift to flying at higher altitudes, the radiative forcing due to contrail cirrus has been forecast to increase by a factor of three in 2050 relative to

2006 [38].

Reducing the number of emitted soot particles by up to one order of magnitude, and thus the number of available ice condensation nuclei, has been shown to cause a reduction of approximately one order of magnitude in the number of ice crystals formed [35, 39]. This, in turn, leads to a larger average ice crystal size (assuming a constant amount of available water vapor) and consequently to a decrease in mean optical depth and lifetime [40–43]. It was found that, for a 2050 scenario, a 50% reduction in aircraft soot emissions could cause the contrail radiation forcing effects to decrease by 15% [38, 39].

Besides their air quality and climate impacts, soot emissions also negatively impact engine performance. Soot particles increase the wall radiant heat load and therefore affect the durability of the engine, decreasing the combustor lifetime [44–46].

1.2.3 Reducing Soot Emissions

Concerns about the impact of soot on local air quality led to the introduction of regulations for soot emissions in 1981, through the use of a maximum smoke number (SN) [19]. The smoke number is a measure for smoke plume visibility and is measured by a filter in the engine exhaust, with a higher smoke number implying higher soot emissions [19]. However, the SN does not capture the physical, chemical and optical properties of the emitted soot, which are considered important factors in assessing the impacts of soot [24, 47]. Consequently, new nvPM emission standards have been developed and agreement on a conceptual system to measure nvPM emissions was reached in 2010 [23]. Next, in 2016, CAEP/10 agreed on the first nvPM standard, providing a limit on the mass concentration of nvPM emissions. This limit was developed using statistical relationships between the SN and the nvPM mass concentration, implying that any engine passing the SN standards would also pass the new nvPM standards [23]. This standard is applied to all in-production engines with a minimum rated thrust of 26.7 kN from 1 January 2020 onwards. The regulations were further developed through CAEP/11, which recommended LTO nvPM mass and number regulatory levels for in-production and new engines based on exten-

sive measurements from 25 engines, and which was reviewed by the ICAO in March 2020 [23]. Furthermore, CAEP/11 recommends moving away from using the SN and to completely transition to nvPM mass and number concentrations, starting on 1 January 2023 [48].

The increased knowledge about the negative impacts of soot emissions has made reducing soot emissions an important topic for both regulators and engine manufacturers [17]. A possible way to do so is by changing the fuel composition. Brem et al. [49] found that a ≈20% reduction in naphthalene volume fraction could lead to reductions of ≈15% and ≈5% in soot mass and number emissions, respectively. A study by Moore et al. [40] estimated that removing naphthalene from jet fuel has the potential of reducing the nvPM number EI by a factor of 10.

Studies evaluating the effect of replacing conventional fuels with a biofuel - Jet A (50:50) blend have found reductions of approximately 25%-60% in mass and 10%-40% in number emissions [47, 50–53].

The ability to model soot formation inside an aircraft engine may allow for more rapidly quantifying the effects of different fuel compositions than experimental approaches, especially. Furthermore, it could help to quantify the effects of combustor and engine design changes in an effort to comply with new ICAO nvPM mass and number standards. It would potentially also allow for predicting soot emissions during cruise (and at other operating conditions), where it is technically challenging and expensive to collect accurate data experimentally [54].

1.3 Existing Models for Predicting Emissions

The previously described need to predict NO_x, CO and soot emissions has led to the development of a variety of different prediction methods. They can be roughly divided into three categories: correlation-based methods, P3T3 and fuel flow methods, and combustor models. The former two are mostly used for NO_x and, to a lesser extent, CO predictions, whereas methods to predict soot emissions generally fall in the latter category.

1.3.1 Correlation-Based Methods

Correlation-based methods use data for specific combustors to establish relationships between engine parameters and the measured emission indices. An example of a correlation-based method for NO_x predictions (primarily for single- and dual-annular combustors) is given by [55, 56]

$$\mathrm{EI}_{\mathrm{NO}_x} = \frac{1.5 \times 10^{15}(\tau - 0.5\tau_{\mathrm{evap}})^{0.5} \exp(\frac{-71{,}100}{T_{\mathrm{st}}})}{P_3^{0.05}(\frac{\Delta P_3}{P_3})^{0.5}}, \tag{1.1}$$

where τ represents the residence time [s], τ_{evap} is the evaporation time [s], T_{st} is the stoichiometric flame temperature [K] and P_3 is the total pressure at the compressor exit [Pa].

Even though these relations might work well for a specific combustor, they are not generalizable and cannot effectively be used to evaluate the effects of combustor or engine design changes and changes in fuel composition [11].

1.3.2 P3T3 Method and Fuel Flow Methods

This set of methods is used for predicting NO_x and CO emissions in response to changes in engine or ambient conditions, which result in different inputs to the combustor. For example, when changing the combustor inlet temperature (T_3) but keeping the combustor design the same, the new EI NO_x can be calculated using this category of methods.

The most accurate and well-known method within this category is the P3T3 method. The P3T3 method is used by engine manufacturers to estimate EI NO_x and EI CO using the difference in combustor inlet pressures and fuel-to-air ratio (FAR) between the LTO points, for which the emissions are known, and the conditions of interest, for which the emissions are unknown [57]. However, the required input parameters for the P3T3 method are proprietary and not publicly available.

To avoid the need for proprietary information, fuel flow methods were developed. Two fuel flow methods are the Boeing Fuel Flow Method 2 (BFFM2) and the DLR method [57, 58]. Although less accurate than the P3T3 method, they only require the

ambient pressure and temperature, as well as the fuel flow, all of which are publicly available [15, 57].

A limitation of the P3T3 method and fuel flow methods is that they cannot directly be used to evaluate fuel composition effects. Furthermore, since they rely on a set of reference data for a specific engine-combustor combination, challenges exist in using these methods to evaluate the effects of design changes to the combustor. Lastly, the curve fits cannot be extrapolated with confidence to estimate emissions at engine conditions where T_3 and/or P_3 are outside the range of data used in calculating the polynomial fits.

The P3T3 method, BFFM2 and DLR method will be used to evaluate the cruise predictions of the current work. They are described in detail in Appendix A.

1.3.3 Combustor Models

This category contains methods that aim to predict gas turbine emissions by modeling the combustion processes inside the engine. The most detailed combustor models are (3D) large eddy simulation (LES) models [59, 60]. However, these methods are computationally expensive and are therefore not considered practical for rapidly quantifying the impact of a variety of different fuel compositions as well as combustor designs.

As a consequence, simplified 0D/1D models have been developed based on reactor networks [19, 61–63]. In these models, the combustor is divided into a number of zones. Each zone is then modeled using a 0D or 1D reactor coupled with a kinetic mechanism to model reactions in the gas phase. Previous work on reactor network models includes the model for NO_x and CO predictions developed by Allaire [61] and extended to include soot by Martini [19], as well as the models developed for NO_x, CO and soot emissions by Bisson et al. [63] and Moniruzzaman et al. [62]. In the first two, mixing of air and fuel is assumed to occur instantaneously and a separate mixing parameter is optimized for every flight condition. The work by Moniruzzaman et al. [62] models the mixing in more detail but only considers the idle operating condition, where soot formation is generally low [6, 49]. Another limitation in the previous work

is the uncertainty in engine-related combustor input conditions such as P_3, T_3 and the mass flows of fuel and air. Furthermore, none of these existing models have been used to quantify the effect of fuel composition on NO_x, CO and soot emissions.

1.4 Current Work

The goal of this work is to develop and evaluate a combustor model able to predict NO_x, CO and soot emissions, and to use it to quantify the effects of changes in fuel composition on NO_x, CO and soot emissions. In particular, the effects of removing naphthalene from jet fuel and using biofuels will be assessed. Other potential applications of the model could be to quantify changes in emissions due to changing engine and combustor designs and varying atmospheric conditions. The model could potentially be used to inform decision-making by regulators and also by engine developers to evaluate the potential of design changes before running expensive experiments or simulations.

The combustor model consists of a reactor network coupled with a gas-phase kinetic mechanism, which is modeled using Cantera [64]. A soot model is added to the reactor network and the interactions between the gas phase and the solid soot phase are modeled in detail. The model is called Pycaso: Python Cantera Soot.

1.5 Thesis Outline

This thesis starts with providing an overview of soot formation and discussing the soot mechanisms used in the soot model in Chapter 2. In Chapter 3, the combustor model, its inputs and the integration of the soot model are described. The quantification of dominant mechanisms for NO_x, CO and soot formation, as well as the quantified impacts of using different fuel compositions, are presented in Chapter 4. Lastly, conclusions and ideas for future work are discussed in Chapter 5.

Chapter 2

Soot Modeling

Modeling aircraft soot formation is complex as its detailed chemical and physical processes are poorly understood [46, 65]. Thousands of reactions with more than a hundred precursor species are involved and complex transitions between the gas phase and solid phase take place [20, 66]. Furthermore, measurements of soot formation inside gas turbines are rare due to the highly turbulent flows, quick chemistry, and limited optical access [46, 67]. Applying soot models that are calibrated using experimental flames to gas turbine combustors has been shown to result in predictions spanning up to four orders of magnitude [19, 46, 68]. In order to account for these differences, multiple soot mechanisms from literature are combined and scaled in this model.

This chapter starts with a general overview of soot formation, followed by an explanation of the role of the fuel composition herein. Then, the soot mechanisms implemented in the model are presented and the scaling methods are explained.

2.1 Steps in Soot Formation

Soot is formed during incomplete combustion processes where there is a shortage of air to completely burn all hydrocarbons in the fuel [33]. In practice, these conditions exist in fuel-rich pockets in the combustor [25]. The process of soot formation is complex and happens in the order of milliseconds [20]. Due to its complexity, the

exact formation process is still unclear. However, soot formation is divided into four steps: nucleation, surface growth, coagulation and oxidation.

The first step of soot formation is nucleation. During nucleation, the inception of soot particles happens through collisions of precursor species [69]. These precursor species are considered to primarily consist of heavy polycyclic aromatic hydrocarbon (PAH) molecules [70, 71]. PAH species are hydrocarbons consisting of at least two aromatic rings [72]. When two PAH molecules collide and stick together, they form a PAH dimer, which again increases in size through collisions with other PAH species and dimers. This growth through collisions allows for transitioning from the gas phase to the solid phase and results in the first solid incipient soot particle [19]. Nucleation is the least well-understood step in the soot formation process due to the large number of contributing species, high number of reactions, low initial soot diameters ($\approx$1-2nm), and the difficulty of capturing the transition from the gas phase to the solid phase that takes place [19, 73].

Nucleation is followed by surface growth and coagulation. During surface growth, the soot particles grow in size and mass due to the adsorption of gas phase molecules, mainly acetylene [20, 74]. This growth increases as a function of temperature, soot surface area and concentration of the precursor species [75]. Growth rates are found to be much higher than nucleation rates and most of the soot mass is thought to form during this step in the process [19].

During coagulation, soot particles grow further in size through particle-particle collisions [20, 69]. The total number of soot particles decreases during coagulation whereas the total particle mass stays constant.

In contrast to the previous three steps, soot is destroyed during oxidation. Carbon and hydrogen atoms are removed from the soot agglomerates by reactions with primarily diatomic oxygen (O_2) and hydroxyl radicals (OH) [76, 77]. Oxidation significantly reduces the amount of soot and measurements suggest that most of the soot formed at the start of the combustion process is oxidized before reaching the combustor exit [78]. For diesel engines, for example, over 90% of soot formed is oxidized before the flow leaves the combustor [21]. This implies that it might be possible to

decrease soot emissions by improving the way air is added in the combustor [45].

2.2 Effect of Fuel Composition on Soot Formation

Since the concentration of PAH species and their growth is understood to mainly depend on the fuel composition, fuel composition is expected to significantly affect soot emissions [20]. This effect can be divided into two categories. First, the concentration of PAH species (e.g. naphthalene) in the fuel directly influences soot formation by affecting nucleation rates. Second, the formation of the first aromatic ring from hydrocarbons in the fuel is found to be the rate-limiting step towards PAH formation [19]. Therefore, the presence of aromatics in the fuel allows for bypassing this rate-limiting step and thus increases PAH concentrations in the combustor, which then leads to higher soot formation rates [19]. Consequently, fuels with higher fractions of aromatics are associated with increased soot emissions [25, 79].

This gives rise to two possible opportunities to reduce soot formation. The first is the removal of PAH species, such as naphthalene, from jet fuel, and the second is the use of alternative (bio)fuels with lower aromatic contents. In this thesis, the effects on soot formation of both naphthalene removal and the use of biofuels are evaluated.

2.3 Soot Model Overview

Soot models based on the four soot formation steps can be roughly divided into three categories: two-equation models, method of moments models and sectional models.

Two-equation models are the most computationally efficient, but assume spherical soot particles with a single particle size [80, 81]. Method of moments models and sectional models both differentiate between particle size classes of soot particles. In the former, average properties (moments) of the number density function (NDF) are solved for [82, 83]. The latter, which is more detailed and computationally expensive, divides the NDF into a finite number of bins. Equations for soot mass and number are subsequently solved for each bin separately [84].

The source terms in each of the three models are determined by specific mechanisms for each of the four soot formation steps. These mechanisms are based on experiments, conducted for a specific flame structure, fuel composition, flow type and temperature and pressure range. For oxidation rates, for example, these measurements have been shown to span seven orders of magnitude [85]. Variations such as these have led to the development of different soot mechanisms, as well as the scaling of coefficients within a specific soot mechanism by factors over two orders of magnitude [19, 63, 86, 87]. The combination of these variations within soot mechanisms and the higher temperatures, pressures and flow velocities inside a gas turbine combustor has caused the previously described prediction range of four orders of magnitude when different soot mechanisms were applied to a gas turbine. Even for possible experiments at conditions similar to those in gas turbine combustors, measurements for different combustors at identical conditions could lead to different soot formation rates due to factors including the air mixing pattern, spray cone angle, swirl and recirculation inside the combustor [22].

Due to this uncertainty, a two-equation model, which is less complex but still captures the four soot formation and depletion processes is selected. In a two-equation model, the soot number density (N) [particles/m^3] and mass density (M) [kg/m^3] are modeled using two equations which represent the change in soot N and M in response to the four soot formation steps. They are given by [88]

$$\left(\frac{dN}{dt}\right)_{\text{mech}} = \left(\frac{dN}{dt}\right)_{\text{nuc}} + \left(\frac{dN}{dt}\right)_{\text{coag}}, \tag{2.1}$$

and

$$\left(\frac{dM}{dt}\right)_{\text{mech}} = \left(\frac{dM}{dt}\right)_{\text{nuc}} + \left(\frac{dM}{dt}\right)_{\text{sg}} + \left(\frac{dM}{dt}\right)_{\text{ox}}, \tag{2.2}$$

where the subscript "mech" indicates that the term is dependent on the specific mechanisms used to model nucleation ("nuc"), surface growth ("sg"), coagulation ("coag") and oxidation ("ox").

As stated previously, N is only affected by nucleation and coagulation. Coagu-

lation reduces N as consequence of particles colliding and sticking together. In the equation for M, coagulation is not present as the total mass during these collisions stays constant. The negative contribution in the equation for M is associated with oxidation as soot mass is destroyed here.

Due to the uncertainty in the soot mechanisms, a scaling factor is introduced for each step of the soot formation process. These factors are assumed to be constants and do not vary with temperature, mean particle size or thrust.

The standard two-equation model assumes that oxidation solely affects the mass density and does not directly destroy soot particles. However, experiments have shown that oxidation can destroy particles and can thus reduce the number density [89, 90]. Therefore, an additional term is included in the number density equation capturing the effect of particle destruction through oxidation. It is assumed that for every change in soot mass equivalent to the average soot particle mass, a variable fraction $\mathrm{ox}_{\mathrm{num,fac}}$ of a particle is destroyed as well.

The updated equations for soot number and mass density are given by

$$\begin{aligned}\left(\frac{dN}{dt}\right)_{\mathrm{mech}} = \; & \mathrm{nuc}_{\mathrm{fac}}\left(\frac{dN}{dt}\right)_{\mathrm{nuc}} + \mathrm{coag}_{\mathrm{fac}}\left(\frac{dN}{dt}\right)_{\mathrm{coag}} \\ & + \mathrm{ox}_{\mathrm{num,fac}}\frac{N}{M}\mathrm{ox}_{\mathrm{fac}}\left(\frac{dM}{dt}\right)_{\mathrm{ox}},\end{aligned} \tag{2.3}$$

and

$$\left(\frac{dM}{dt}\right)_{\mathrm{mech}} = \mathrm{nuc}_{\mathrm{fac}}\left(\frac{dM}{dt}\right)_{\mathrm{nuc}} + \mathrm{sg}_{\mathrm{fac}}\left(\frac{dM}{dt}\right)_{\mathrm{sg}} + \mathrm{ox}_{\mathrm{fac}}\left(\frac{dM}{dt}\right)_{\mathrm{ox}}. \tag{2.4}$$

The specific mechanisms used to compute the nucleation, surface growth, coagulation and oxidation terms in Equations 2.3 and 2.4 are described in the subsequent sections.

2.4 Nucleation

The first soot particles are formed during nucleation by collisions of PAH molecules. Two main families of nucleation mechanisms exist. The first assumes nucleation is a

first-order function of the acetylene concentration [79, 91]. The reason behind this is that these methods were primarily developed for fuels containing aliphatic hydrocarbons [92]. For these fuels, the rate-limiting step in soot formation is the formation of single-ring aromatic species, which occurs through reactions with acetylene [92]. However, since Jet A consists of up to 25% v/v of aromatic species, and this work aims to quantify the effect of aromatic species on soot emissions, acetylene-based nucleation models are not considered [93]. Instead, nucleation rates directly dependent on the concentrations of PAH species are used. Only PAH-PAH collisions are considered for nucleation in the model and PAH-soot collisions are modeled as surface growth and are described in the subsequent sections. The nucleation rate resulting from collisions of PAH species i and j is based on the collision frequency $\beta_{i,j}$ defined as [94]

$$\beta_{i,j} = N_i N_j \pi (r_i + r_j)^2 \sqrt{\frac{8 k_B T}{\pi \mu_{i,j}}}, \tag{2.5}$$

resulting in the following expression for the nucleation rate [69, 87]

$$\left(\frac{dN}{dt}\right)_{\text{nuc},ij} = \frac{(\gamma_i + \gamma_j)}{2} \epsilon \sqrt{\frac{8\pi k_B T}{\mu_{i,j}}} N_A^2 (r_i + r_j)^2 [\text{PAH}_i][\text{PAH}_j], \tag{2.6}$$

where $\epsilon = 2.2$ is the Van der Waals enhancement factor, k_B is the Boltzmann constant [J/K], N_A is Avogadro's constant [kmol^{-1}], r_i and r_j are the radii of PAH species i and j [m], $\mu_{i,j}$ is the reduced mass of PAH species i and j [kg] and [PAH$_i$] is the concentration of PAH species i [kmol/m^3]. Due to the low binding energy of the dimer formed from the PAH-PAH collisions (e.g. 19.6 kJ/mol for a pyrene dimer) and its small lifetime (2-20 ps), assuming every collision leads to the formation of a soot particle would result in an overprediction of N [69, 70]. Therefore a sticking coefficient γ ($<$1) is used to scale down the number of soot particles formed [69]. This sticking coefficient has been shown to increase with PAH size and is assumed to scale with the PAH mass to the fourth power [69, 95]

$$\gamma_i = C_N m_i^4. \tag{2.7}$$

Based on sample values for γ in literature, C_N is found to be approximately 1.48×10^{-11}, resulting in sticking coefficients of the PAH species in the model as shown in Table 2.1 [69]. The PAH species are chosen such that no direct pathways from species in the fuel surrogates to soot mass through nucleation exist, as these pathways might result in an overestimation of sensitivities to fuel composition. Naphthalene is thus not used as one of the nucleating species in the soot model and is therefore not shown in Table 2.1.

Table 2.1: Sticking coefficients of the PAH species (γ) and their radicals ($\gamma^\bullet$) in the soot model.

PAH name	**Formula**	γ ($\gamma^\bullet$)
Acenaphthylene	$C_{12}H_8$	0.0079 (0.0077)
Biphenyl	$C_{12}H_{10}$	0.0084 (0.0081)
Fluorene	$C_{13}H_{10}$	0.011
Phenathrene	$C_{14}H_{10}$	0.015 (0.015)
Pyrene	$C_{16}H_{10}$	0.025 (0.024)

The total nucleation rate is calculated by taking the sum over all the L PAH species in the gas-phase mechanism using

$$\left(\frac{dN}{dt}\right)_{\text{nuc}} = \sum_{i=1}^{L}\sum_{j=1}^{i}\left(\frac{dN}{dt}\right)_{\text{nuc},ij}. \tag{2.8}$$

The nucleation term for the equation for M is then computed via

$$\left(\frac{dM}{dt}\right)_{\text{nuc}} = \sum_{i=1}^{L}\sum_{j=1}^{i}\frac{n_{\text{C},ij}W_{\text{C}}}{N_A}\left(\frac{dN}{dt}\right)_{\text{nuc},ij}, \tag{2.9}$$

where $n_{\text{C},ij}$ is the combined number of carbon atoms in PAH species i and j and W_{C} is the atomic weight of carbon. By using $n_{\text{C},ij}$, soot is assumed to only consist of carbon atoms. This assumption is made as carbon mass percentages in soot have been found to lie between 90%–98% [33].

2.5 Surface Growth

Surface growth is responsible for the majority of soot mass formation [77]. During surface growth, the mass of soot particles grows by the adsorption of other species. The most important of those species is acetylene, but PAH species also play a role [74, 96]. In this work, two types of surface growth mechanisms are implemented. Mechanism A assumes surface growth solely by acetylene, whereas mechanism B also includes surface growth through condensation of PAH species on the soot surface. Even though acetylene adsorption might have a larger effect on the soot mass than PAH condensation, the latter might increase competition for PAH species between surface growth and nucleation, which leads to a decrease in nucleation rates. Reducing the number density also reduces the available soot surface area (larger particles) and, as will be discussed in subsequent sections, therefore reduces oxidation rates.

In mechanism A, surface growth is approximated as a first-order reaction with acetylene, given by [74, 77, 79, 81]

$$\mathrm{C_2H_2} \longrightarrow 2\,\mathrm{C_{soot}} + \mathrm{H_2}, \tag{2.10}$$

for which the corresponding source term for the mass density equation is [77]

$$\left(\frac{dM}{dt}\right)_{\mathrm{sg}} = 2W_{\mathrm{C}}k_G(T)[\mathrm{C_2H_2}]f(A_s), \tag{2.11}$$

where W_{C} is the atomic weight of carbon [kg/kmol], $k_G(T)$ is the surface growth reaction rate constant [m/s] and $f(A_s)$ represents a function of the total available soot surface area A_s [$\mathrm{m^2/m^3}$], which is calculated using [80]

$$A_s = N\pi d_p^2, \tag{2.12}$$

where d_p is the soot mean particle diameter [m], computed via [80]

$$d_p = \left(\frac{6M}{\pi\rho_{\mathrm{soot}}N}\right)^{\frac{1}{3}}. \tag{2.13}$$

Soot mass formation is sensitive to the surface area function $f(A_s)$. However, no consensus exists over the form of the surface area function [89]. Examples of proposed forms of $f(A_s)$ in literature are: $f(A_s) = A_s$, $f(A_s) = \chi A_s$, $f(A_s) = \sqrt{A_s}$, and $f(A_s) = 0$ [77]. The former two, representing an unscaled dependence on soot surface area and scaled dependence based on a surface chemistry correction factor χ, are used in this thesis. The first is described in this section and the second is discussed in Section 2.8.

For the case with unscaled dependence on A_s, $k_G(T)$ is computed using

$$k_G(T) = A_{k_G} \exp\left(\frac{E_A}{R_u T}\right), \tag{2.14}$$

where E_A is the activation energy [J/kmol] and R_u is the universal gas constant [J/(kmol·K)]. A ratio E_a/R_u of 12,100 K and a pre-exponential constant A_{k_G} of 7.50×10^2 m/s are used in this thesis [89, 97].

In mechanism B, the surface growth source term is expanded with a term for soot growth by adsorption of PAH species. This reaction is summarized as

$$\mathrm{C_{soot}} + \mathrm{PAH} \longrightarrow \mathrm{C_{soot}{-}C_{PAH}} + \mathrm{H_{PAH}}. \tag{2.15}$$

The corresponding source term for the soot mass density equation is based on the collision frequency of soot particles with PAH species i and is given by

$$\left(\frac{dM}{dt}\right)_{\mathrm{sg},i} = n_{\mathrm{C},i} W_{\mathrm{C}} \frac{\gamma_{\mathrm{soot}} + \gamma_i}{2} \epsilon \sqrt{\frac{8\pi k_B T}{\mu_{\mathrm{soot},i}}} \left(\frac{d_p}{2} + r_i\right)^2 N[\mathrm{PAH}_i], \tag{2.16}$$

where $n_{\mathrm{C},i}$ represents the number of carbon atoms of PAH_i and γ_{soot} is assumed to be equal to 0.3 [66]. The other symbols are equivalent to those presented in the previous sections. The total surface growth source term due to adsorption of L types of PAH species is then calculated using

$$\left(\frac{dM}{dt}\right)_{\mathrm{sg,PAH}} = \sum_{i=1}^{L} \left(\frac{dM}{dt}\right)_{\mathrm{sg},i}. \tag{2.17}$$

2.6 Coagulation

The implemented coagulation mechanism is based on the collision of two spherical particles with a collision rate as defined by Puri et al. [98]. The resulting source term for the number density equation is given by

$$\left(\frac{dN}{dt}\right)_{\text{coag}} = -C_{\text{coag}}\sqrt{\frac{24R_uT}{\rho_{\text{soot}}N_A}}d_p^{\frac{1}{2}}N^2, \tag{2.18}$$

where ρ_{soot} is assumed to be equal to 2000 kg/m^3, R_u is the universal gas constant and C_{coag} is a constant ranging between 1 and 9 in literature [81, 92]. These values of C_{coag} were determined through comparing experiments of (laminar) flame data with a numerical soot model [81]. Since the flow in a gas turbine combustor is turbulent, the values from literature might be an underestimation for coagulation.

2.7 Oxidation

The two primary species involved in soot oxidation are OH and O_2 with their (simplified) oxidation reactions given by [77]

$$\text{C}_{\text{soot}} + \text{OH} \longrightarrow \text{CO} + \text{H}, \tag{2.19}$$

and

$$\text{C}_{\text{soot}} + \text{O}_2 \longrightarrow \text{CO} + \text{O}. \tag{2.20}$$

From other oxygen-containing species such as O, H_2O and CO_2, only O has been observed to significantly contribute to oxidation. Its oxidation reaction can be simplified to [77]

$$\text{C}_{\text{soot}} + \text{O} \longrightarrow \text{CO}. \tag{2.21}$$

Assuming gas phase diffusion occurs fast, the general soot oxidation rate due to

oxidizing species i can be expressed as [85]

$$\left(\frac{dM}{dt}\right)_{\text{ox},i} = -0.25 W_{\text{C}} \eta_i [i] \sqrt{\frac{8 R_u T}{\pi W_i}} \exp\left(\frac{-E_{A,i}}{R_u T}\right) A_s, \tag{2.22}$$

where η_i represents the collision efficiency [-], $[i]$ is the concentration of oxidizing species i [kmol/m^3], W_i is the molecular weight of the oxidizing species i [kg/kmol] and $E_{A,i}$ is the activation energy for the oxidation reaction by species i [J/kmol]. Considering oxidation by hydroxide and assuming a negligible activation energy $E_{A,\text{OH}}$, Equation 2.22 reduces to [19, 85]

$$\left(\frac{dM}{dt}\right)_{\text{ox,OH}} = -8.82 \eta_{\text{OH}} W_{\text{C}} T^{0.5} [\text{OH}] A_s. \tag{2.23}$$

Collision efficiency values ranging from 0.01 to 0.65 have been proposed [76, 80, 85, 96, 99–101]. A value of 0.13, determined by Neoh et al. [76], is used as baseline value in this model.

The general form of the oxidation rate due to oxidation by O_2 resulting from Equation 2.22 is given by [80]

$$\left(\frac{dM}{dt}\right)_{\text{ox},\text{O}_2} = -\eta_{\text{O}_2} W_{\text{C}} k_{\text{O}_2}(T) [\text{O}_2] A_s, \tag{2.24}$$

where the collision efficiency η_{O_2} is assumed to be unity [80, 92]. In this thesis, $k_{\text{O}_2}(T)$ is assumed to be $745.88 T^{0.5} \exp(\text{-}19{,}680/\text{T})$ [m/s] [77, 89, 92].

Lastly, the general equation for the reaction rate of oxidation by O again follows from Equation 2.22. Assuming a negligible activation energy, it is given by [80]

$$\left(\frac{dM}{dt}\right)_{\text{ox,O}} = -\eta_{\text{O}} W_{\text{C}} k_{\text{O}}(T) [\text{O}] A_s, \tag{2.25}$$

where $k_{\text{O}}(T)$ is taken to be equal to $1.82\sqrt{T}$ [m/s] and the collision efficiency η_{O} is assumed to be unity [80].

2.8 Combined Surface Growth and Oxidation

In the surface growth and oxidation mechanisms described so far, reaction rates are assumed to depend on the total soot surface area directly without taking into account surface chemistry properties. The combined surface growth and oxidation mechanism, represented by the H-abstraction/C_2H_2-addition (HACA) mechanism, does so by estimating the number of available surface sites on the soot surface [102]. Two types of carbon atoms on the soot surface are identified: hydrogen-saturated carbon atoms and radical carbon atoms [102].

Multiple variants of the HACA mechanism exist. The mechanism implemented in this work is summarized in Table 2.2 [103].

Table 2.2: Overview of reactions and reaction rate coefficients for the HACA mechanism with $k = AT^n \exp\left(\frac{E_A}{R_u T}\right)$.

No.	**Reaction**	**A** $\left[\frac{\mathbf{m^3}}{\mathbf{kmol \cdot s}}\right]$	**n** [-]	**E** $\left[\frac{\mathbf{J}}{\mathbf{kmol}}\right]$
1a	$C_{soot}{-}H + H \longrightarrow C_{soot}^{\bullet} + H_2$	4.2×10^{10}	-	5.44×10^{7}
1b	$C_{soot}{-}H + H \longleftarrow C_{soot}^{\bullet} + H_2$	3.9×10^{9}	-	4.60×10^{7}
2a	$C_{soot}{-}H + OH \longrightarrow C_{soot}^{\bullet} + H_2O$	1.0×10^{7}	0.734	5.98×10^{6}
2b	$C_{soot}{-}H + OH \longleftarrow C_{soot}^{\bullet} + H_2O$	3.7×10^{5}	1.139	7.15×10^{6}
3	$C_{soot}^{\bullet} + H \longrightarrow C_{soot}{-}H$	2.0×10^{10}	-	-
4	$C_{soot}^{\bullet} + C_2H_2 \longrightarrow C_{soot}{-}H + H$	8.0×10^{4}	1.560	1.59×10^{7}
5	$C_{soot}^{\bullet} + O_2 \longrightarrow 2\,CO + \text{products}$	2.2×10^{9}	-	3.14×10^{7}
6	$C_{soot}{-}H + OH \longrightarrow CO + \text{products}$	Calculated using Equation 2.23		

Using the reaction rate constants from Table 2.2, while assuming steady state and using a number density of $C_{soot} - H$ sites ($\chi_{C_{soot}-H}$) of 2.3×10^{19} sites/m^2, the number density of radical carbon atoms is calculated from [102]

$$\chi_{C_{soot}^{\bullet}} = \frac{k_{1a}[H] + k_{2a}[OH]}{k_{1b}[H_2] + k_{2b}[H_2O] + k_3[H] + k_4[C_2H_2] + k_5[O_2]} \chi_{C_{soot}-H}. \tag{2.26}$$

The general form of the reaction rate expression (r_i) for the HACA mechanism is given by [102]

$$r_i = k_{g,s} C_g \alpha \chi_s A_s, \tag{2.27}$$

where $k_{g,s}$ is the (per-site) rate coefficient as shown in Table 2.2 and C_g is the concentration of gas species g. α represents the fraction of available surface sites and is dependent on the temperature. The soot agglomerates are expected to be more mobile at elevated temperatures and consequently align themselves concentrically [104]. This limits the access of gas species to the reactive carbon sites and therefore α decreases [104]. Taking into account this temperature effect, α is calculated using [105]

$$\alpha = \frac{1}{2}\left(\tanh\left(\frac{8,168}{T[\mathrm{K}]} - 4.57\right) + 1\right). \tag{2.28}$$

The expression for the surface growth and oxidation rates used in the two-equation model are derived to be

$$\left(\frac{dM}{dt}\right)_{\mathrm{sg,C_2H_2}} = 2W_{\mathrm{C}} k_4 [\mathrm{C_2H_2}] \alpha \frac{\chi_{\mathrm{C^\bullet_{soot}}}}{N_A} A_s, \tag{2.29}$$

and

$$\left(\frac{dM}{dt}\right)_{\mathrm{ox,O_2}} = -W_{\mathrm{C}} k_5 [\mathrm{O_2}] \alpha \frac{\chi_{\mathrm{C^\bullet_{soot}}}}{N_A} A_s. \tag{2.30}$$

Similarly to the surface growth mechanism described in Section 2.5, two variants of the HACA mechanism are used. Mechanism A again solely considers surface growth due to reactions with acetylene, whereas mechanism B also considers PAH condensation effects using Equation 2.17.

Even though the HACA mechanism does capture more detail than surface growth mechanisms that do not take into account surface properties, its performance is not always better than the less detailed models, and major uncertainty concerning the surface reactivity still exists [77, 106].

2.9 Soot Model Configurations Approach

The previously described variations in soot mechanisms and coefficients are combined into multiple soot model configurations. Each configuration consists of a different set of mechanisms (e.g. surface growth with or without PAH species) and a unique set of scaling coefficients. This method is selected as it allows for understanding differences between various mechanisms in the literature and increases the robustness of the predictions by relying on the predictions of multiple models and thus reducing the risk of overfitting one specific soot model.

Table 2.3 contains an overview of the parameters that are varied between different soot model configurations.

Table 2.3: Overview of the soot model input parameters that are varied in generating soot model configurations.

Parameter	**Description**
nuc_{fac}	Nucleation scaling factor
coag_{fac}	Coagulation scaling factor
sg_{fac}	Surface growth scaling factor
ox_{fac}	Oxidation scaling factor
$\text{ox}_{\text{num,fac}}$	Oxidation number reduction factor
sg species	Species used for surface growth
HACA	Surface growth through HACA switch
η_{OH}	Collision efficiency for oxidation through OH

Chapter 3

Combustor Model

A 0D/1D combustor model is developed to predict NO_x, CO and soot emissions. The model is split into two sections: a primary zone and a secondary zone. This allows one to account for different mixing effects related to ignition of the fuel droplets and mixing of cooling air with the fuel-air mixture further downstream in the combustor. This chapter starts with a description of the combustor architecture and an explanation of the model parameters. Then, the model equations are derived and the method of modeling interactions between the solid soot phase and the gas phase is presented. Next, the gas-phase mechanism used is discussed and the fuel modeling is explained. Lastly, the input conditions related to the engine operating conditions are summarized and the model calibration is explained.

3.1 Combustor Overview

The combustor model in this work represents the combustor of the CFM56 Tech Insertion engine family [107]. More specifically, the CFM56-7B Tech Insertion configuration is selected as it is one of the most sold engines at the moment and measurement data for soot has been published [108]. Over 8,000 CFM56-7B engines are in service now and this number is expected to increase as the engine will be used on Boeing's new generation of single-aisle aircraft [108].

The CFM56 Tech Insertion engines use a Rich-Burn Quick-Mix Lean-Burn (RQL)

combustor. The concept of RQL combustors was developed in 1980 in order to reduce NO_x emissions [109]. In an RQL combustor, as illustrated in Figure 3-1, air and fuel are first mixed at equivalence ratios ϕ (often) larger than 1 in the initial, rich zone. This increases the stability of combustion by providing high concentrations of energetic hydrogen and hydrocarbon radicals and limits the formation of NO_x due to the limited amount of available oxygen [110]. After the rich zone, air is added in the quenching zone and the overall equivalence ratio shifts from being rich to being lean. This addition of air happens quickly in order to minimize NO_x formation at (close-to) stoichiometric (ϕ =1) conditions where temperatures are generally highest [111]. After the rapid mixing in the quenching zone, additional air is added to further cool down the mixture before entering the turbine and to burn remaining partially pyrolized hydrocarbon species (such as CO) [110].

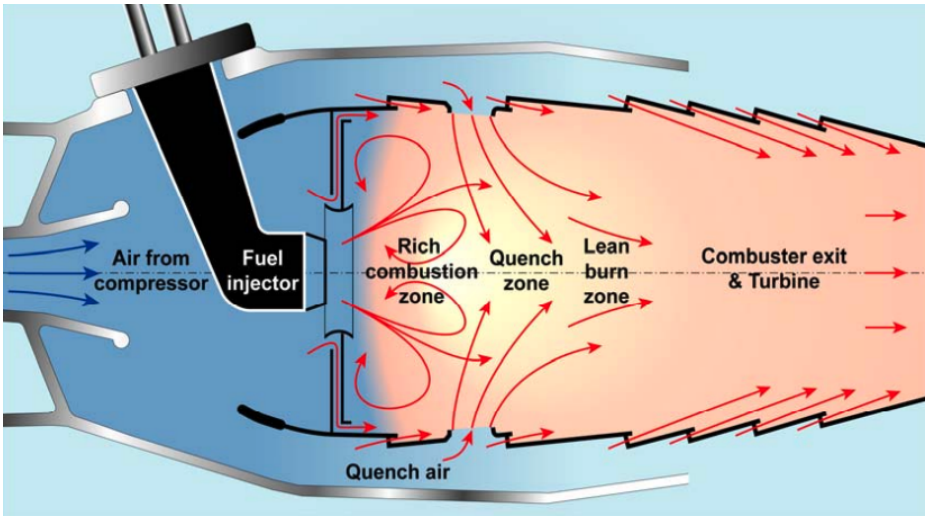

Figure 3-1: RQL combustor schematic [15].

To simulate an RQL combustor, the combustor model consists of a primary zone (PZ) and a secondary zone (SZ), coupled with a soot model. A schematic overview of the model is presented in Figure 3-2. In the primary zone, air and fuel are mixed at a certain equivalence ratio. Then, the quenching happens at the start of the secondary zone through to the addition of secondary air (SA). Here, the rapid transition from rich to lean conditions takes place. In the second part of the secondary zone, dilution air (DA) is added to represent the lean burn zone.

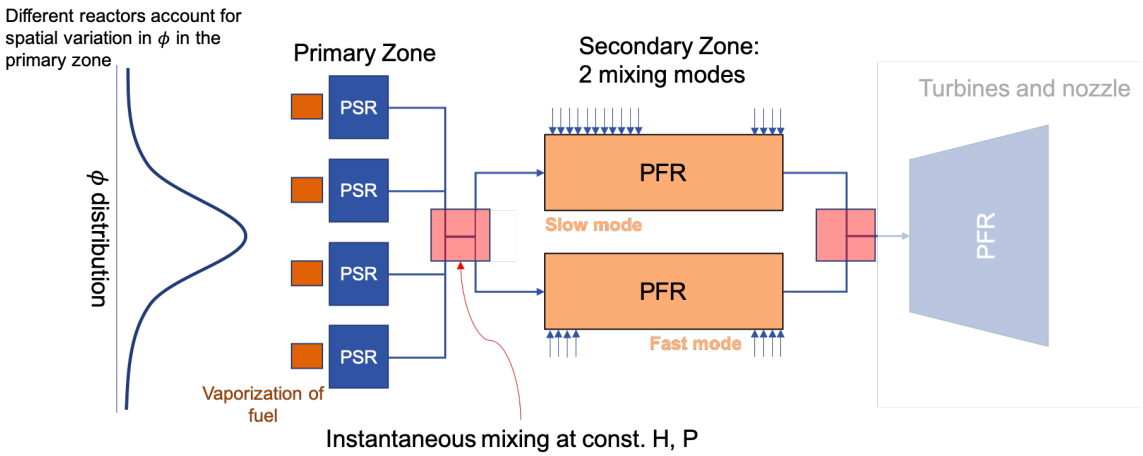

Figure 3-2: Schematic overview of the combustor model. Multiple well-stirred reactors (WSR) are used in the primary zone. The secondary zone uses a combination of plug flow reactors (PFR) to simulate different mixing times. The arrows represent secondary and dilution air entering the combustor.

3.1.1 Primary Zone Architecture

Given the combustor geometry, upstream conditions and fuel composition, the primary zone models the first part of the combustion process. The primary zone is modeled as a set of N_{PZ} well-stirred (or perfectly stirred) reactors at different equivalent ratios in order to capture mixture inhomogeneity. When using one well-stirred reactor, and thus one equivalence ratio, perfect mixing would be assumed. This is not realistic as the fuel and air are injected separately and pockets of combustible mixture with different fuel-to-air ratios (FAR) are formed upon vaporization of the fuel droplets. This leads to a non-uniform distribution of fuel droplets throughout the primary zone [22, 61]. Capturing this mixture inhomogeneity is considered important as the formation rates of NO_x, CO and soot all strongly depend on the local equivalence ratio [112].

The N_{PZ} reactors are modeled at different equivalence ratios according to a normal distribution with mean equivalence ratio $\bar{\phi}$ and standard deviation $\sigma_{\bar{\phi}}$. The latter represents the degree of mixing in the primary zone and thus captures inhomogeneity effects. In a perfectly mixed situation (i.e. $\sigma_{\bar{\phi}} = 0$), the distribution would thus approach the delta distribution. The fraction of mass flow entering reactor i at

equivalence ratio ϕ_i, $f(\phi_i)$, is calculated using a normal distribution [112]

$$f(\phi_i) = \frac{1}{\sigma_{\bar{\phi}}\sqrt{2\pi}} \exp\left(\frac{-(\phi_i - \bar{\phi})^2}{2\sigma_{\bar{\phi}}^2}\right) \Delta\phi. \tag{3.1}$$

where $\Delta\phi$ decreases when the number of PZ reactors increases. The value of $\sigma_{\bar{\phi}}$ is calculated using a mixing parameter S_{PZ}, which is defined as [112]

$$S_{\mathrm{PZ}} = \frac{\sigma_{\bar{\phi}}}{\bar{\phi}}. \tag{3.2}$$

The higher S_{PZ}, the larger the nonuniformity in the primary zone (S_{PZ}=0 implies perfect mixing) [112]. It is unclear whether S_{PZ} is a function of combustor geometry, equivalence ratio or both [61, 112–114]. In this model, S_{PZ} is solely a function of combustor design since it is assumed that most of the unmixedness effects are captured by the both the combustor-specific fuel injection process and the air flow pattern, while little is known about the potential dependency of S_{PZ} on the equivalence ratio [112, 113].

The mean equivalence ratio depends on engine thrust and the primary zone design equivalence ratio ($\phi_{\mathrm{PZ,des}}$), which is the equivalence ratio in the primary zone at maximum thrust. The PZ equivalence ratio at maximum thrust determines the fraction of total air present in the combustor that enters the primary zone $f_{\mathrm{air,PZ}}$ via

$$f_{\mathrm{air,PZ}} = \frac{\dot{m}_{\mathrm{fuel,takeoff}} F_{\mathrm{sc}}}{\phi_{\mathrm{PZ,des}} \dot{m}_{\mathrm{air,takeoff}} \mathrm{FAR}_{\mathrm{st}}}, \tag{3.3}$$

where $\dot{m}_{\mathrm{fuel,takeoff}}$ is the mass flow of fuel entering the combustor at takeoff and, likewise, $\dot{m}_{\mathrm{air,takeoff}}$ is the mass flow of air at takeoff. $\mathrm{FAR}_{\mathrm{st}}$ is the stoichiometric fuel-to-air ratio and F_{sc} represents a fuel scaler, which corrects the fuel flow in order to match the total heat addition from fuels used in generating the model input data. F_{sc} is defined as

$$F_{\mathrm{sc}} = \frac{\mathrm{LHV}_{\mathrm{inputfuel}}}{\mathrm{LHV}_{\mathrm{modelfuel}}}, \tag{3.4}$$

where $\mathrm{LHV}_{\mathrm{inputfuel}}$ is the lower heating value [MJ/kg] used in the engine model to

Table 3.1: Overview of primary zone architecture input variables.

Variable	Units	Description
$\phi_{\mathrm{PZ,des}}$	[-]	Primary zone design equivalence ratio
N_{PZ}	[-]	Number of primary zone reactors
S_{PZ}	[-]	Primary zone mixing parameter
V_{PZ}	[m^3]	Primary zone volume

generate the input conditions and $\mathrm{LHV}_{\mathrm{modelfuel}}$ is the lower heating value of the fuel used in the combustor model.

The fraction of total air entering the primary zone is assumed to be a consequence of the combustor design and is thus assumed to be constant for all thrust conditions and fuel compositions. Therefore, once a feasible value for $f_{\mathrm{air,PZ}}$ is found using the equations above, its value will be fixed. The mean equivalence ratio at thrust level j can then be calculated as

$$\bar{\phi}_{\mathrm{j}} = \frac{\dot{m}_{\mathrm{fuel},j} F_{\mathrm{sc}}}{f_{\mathrm{air,PZ}} \dot{m}_{\mathrm{air},j} \mathrm{FAR}_{\mathrm{st}}}. \tag{3.5}$$

Table 3.1 provides an overview of the input variables related to the primary zone architecture. $\phi_{\mathrm{PZ,des}}$ determines the amount of air entering the N_{PZ} reactors. The total primary zone volume V_{PZ} determines the total residence time and thus directly influences emission indices [5]. V_{PZ} is divided over the N_{PZ} reactors assuming the residence time in each reactor to be identical. The residence time in reactor i is calculated using

$$t_{\mathrm{res},i} = \frac{V_{\mathrm{PZ},i}}{\rho_i (\dot{m}_{\mathrm{fuel},i} + \dot{m}_{\mathrm{air},i})}. \tag{3.6}$$

where $V_{\mathrm{PZ},i}$ is the volume of PZ reactor i [m^3] and ρ_i is the density of the mixture in reactor i [$\mathrm{kg/m}^3$]. As will be discussed in Section 3.2, the total mass in reactor i stays approximately constant. Therefore the initial density in reactor i is used as ρ_i.

Table 3.2: Overview of secondary zone architecture input variables.

Variable	Units	Description
A_{SZ}	[m^2]	Secondary zone cross-sectional area
L_{SZ}	[m]	Secondary zone length
$\phi_{\mathrm{SZ,des}}$	[-]	Secondary zone design equivalence ratio
$\ell_{\mathrm{SA,SM}}$	[-]	Secondary air length fraction (of L_{SZ}) in slow mode
$\ell_{\mathrm{SA,FM}}$	[-]	Secondary air length fraction (of L_{SZ}) in fast mode
$\ell_{\mathrm{DA,start}}$	[-]	Dilution air start length fraction (of L_{SZ})
$\ell_{\mathrm{DA,end}}$	[-]	Dilution air end length fraction (of L_{SZ})
f_{SM}	[-]	Fraction of PZ mixture that enters the slow mode

3.1.2 Secondary Zone Architecture

The secondary zone is modeled as a combination of two parallel plug flow reactors (PFR). The flow exiting the N_{PZ} primary zones is mixed together at constant enthalpy and pressure and then split up into two zones, in order to simulate different mixing timescales. The first zone is referred to as the slow mixing zone (SM), in which secondary air is mixed in over a larger length and thus larger time. The second zone is the fast mixing zone (FM). Here, secondary air is mixed very quickly. After the two mixing zones, dilution air is added at the end of the secondary zone. Since temperatures will have significantly decreased towards the end of the secondary zone, the chemical effect of dilution air is expected to be insignificant. Therefore no distinction in mixing times is made in the dilution zone. Table 3.2 provides an overview of the secondary zone architecture variables.

As previously described, two types of air are added in the secondary zone. First, secondary air is added to cool down the mixture coming in from the primary zone. The secondary air is assumed to be inserted uniformly over a variable fraction ($\ell_{\mathrm{SA,SM}}$ and $\ell_{\mathrm{SA,FM}}$) of secondary zone length, starting from the secondary zone entrance. Second, dilution air is added towards the end of the secondary zone to further cool down the mixture so that it meets turbine inlet temperature limits. The start and

end points of the region where dilution air is added are calculated using $\ell_{\mathrm{DA,start}}$ and $\ell_{\mathrm{DA,end}}$. The magnitude of incoming airflow at any point in the secondary zone is called $\beta_{\mathrm{air,in}}$ [kg/(m·s)] , which is defined as

$$\beta_{\mathrm{air,in}} = \begin{cases} \beta_{\mathrm{SA,SM}}, & \text{if } 0 \leq z \leq \ell_{\mathrm{SA,SM}} L_{\mathrm{SZ}} \\ \beta_{\mathrm{SA,FM}}, & \text{if } 0 \leq z \leq \ell_{\mathrm{SA,FM}} L_{\mathrm{SZ}} \\ \beta_{\mathrm{DA}}, & \text{if } \ell_{\mathrm{DA,start}} L_{\mathrm{SZ}} \leq z \leq \ell_{\mathrm{DA,end}} L_{\mathrm{SZ}} \\ 0, & \text{otherwise.} \end{cases} \tag{3.7}$$

The magnitudes of $\beta_{\mathrm{SA,SM}}$, $\beta_{\mathrm{SA,FM}}$ and β_{SA} are calculated via

$$\begin{aligned} \beta_{\mathrm{SA,SM}} &= \frac{f_{\mathrm{air,SA}} f_{\mathrm{SM}} \dot{m}_{\mathrm{air}}}{\ell_{\mathrm{SA,SM}} L_{\mathrm{SZ}}} \\ \beta_{\mathrm{SA,FM}} &= \frac{f_{\mathrm{air,SA}} f_{\mathrm{FM}} \dot{m}_{\mathrm{air}}}{\ell_{\mathrm{SA,FM}} L_{\mathrm{SZ}}} \\ \beta_{\mathrm{DA}} &= \frac{f_{\mathrm{air,DA}} \dot{m}_{\mathrm{air}}}{(\ell_{\mathrm{DA,end}} - \ell_{\mathrm{DA,start}}) L_{\mathrm{SZ}}}, \end{aligned} \tag{3.8}$$

where f_{FM} is equal to $1 - f_{\mathrm{SM}}$ and the fraction of total air entering the secondary zone as secondary air ($f_{\mathrm{air,SA}}$) is calculated using the secondary zone design equivalence ratio $\phi_{\mathrm{SZ,des}}$ as

$$f_{\mathrm{air,SA}} = \frac{\dot{m}_{\mathrm{fuel,takeoff}}}{\phi_{\mathrm{SZ,des}} \mathrm{FAR}_{\mathrm{st}} \dot{m}_{\mathrm{air,takeoff}}}. \tag{3.9}$$

The dilution air fraction then follows from

$$f_{\mathrm{air,DA}} = 1 - f_{\mathrm{air,PZ}} - f_{\mathrm{air,SA}}. \tag{3.10}$$

The distance over, and consequently time in, which air is added in the secondary zone is important for emissions predictions, especially when the primary zone is fuel rich. In this case, the mixture transitions from being rich to lean in the secondary zone and stoichiometric conditions are thus reached while adding air. These stoichiometric conditions are expected to cause peaks in NO_x formation rates [112]. The rate at which air is added is expected to determine the duration of this stoichiometric peak

period. On the other hand, when conditions in the primary zone are stoichiometric or lean, the secondary air primarily acts as cooling and rapidly quenches the NO_x formation reactions [112]. The dilution air further downstream of the secondary zone is expected to primarily have a cooling and diluting effect [112].

3.2 Primary Zone Equations

The model equations for the model without soot are explained first, followed by a more extensive set of equations used to model the primary zone with soot. Each of the primary zone reactors is modeled as a perfectly stirred reactor (or well-stirred reactor). A perfectly stirred reactor is a reactor with an inlet, an outlet and a constant volume, where mixing occurs for a certain residence time t_{res} while chemical reactions take place [64].

3.2.1 Primary Zone Without Soot

The mixture in the primary zone is assumed to behave as an ideal gas under constant pressure conditions. The primary zone's three main equations are based on the conservation of mass, species and energy, and are solved in time (t) for each of the N_{PZ} reactors. The conservation of mass m [kg] is expressed by [64]

$$\frac{dm}{dt} = \dot{m}_{\text{in}} - \dot{m}_{\text{out}}, \tag{3.11}$$

where the mass flow leaving the reactor $\dot{m}_{\text{out}}$ is equal to the mass flow entering the reactor plus a correction accounting for the difference between the initial pressure (P_0) and the pressure inside the reactor (P). Hence, $\dot{m}_{\text{out}}$ is calculated using [64]

$$\dot{m}_{\text{out}} = \dot{m}_{\text{in}} + K_v(P - P_0), \tag{3.12}$$

where the proportionality constant K_v is set to 0.001 kg/(s·Pa). The equation for the conservation of species is given by [64]

$$\frac{dY_k}{dt} = \frac{\dot{\omega}_k W_k}{\rho_{\text{gas}}} + \frac{\dot{m}_{\text{in}}(Y_{k,\text{in}} - Y_k)}{m}, \tag{3.13}$$

where Y_k is the mass fraction of species k in the gas, $\dot{\omega}_k$ represents the formation rate of species k [kmol/(m^3·s)], W_k is the molecular weight [kg/kmol] and ρ_{gas} is the density of the gas inside the primary zone reactor [kg/m^3]. The subscript "in" relates to the flow entering the reactor.

The energy equation used for the ideal gas constant pressure reactor is [64]

$$\frac{dT}{dt} = \frac{1}{mc_p}\left[\dot{m}_{\text{in}}(h_{\text{in}} - \sum_{k=1}^{K} h_k Y_{k,\text{in}}) - \sum_{k=1}^{K} h_k \dot{m}_{k,\text{gen}}\right], \tag{3.14}$$

where K is the total number of species in the gas, c$_p$ is the specific heat capacity of the gas at constant pressure [J/(kg·K)] and h_k is the specific enthalpy of species k [J/kg]. $\dot{m}_{k,\text{gen}}$ represents the generated mass per second of species k [kg/s] and is defined as [64]

$$\dot{m}_{k,\text{gen}} = V_{\text{PZ}} \dot{\omega}_k W_k. \tag{3.15}$$

3.2.2 Primary Zone With Soot

The three equations (for m, Y and T) solved in the primary zone without soot are expanded in order to account for the presence of soot. Furthermore, two extra equations are introduced to account for the soot number and mass density.

Starting with conservation of mass, the soot mass m_{soot} is computed as

$$m_{\text{soot}} = M V_{\text{PZ}}, \tag{3.16}$$

where M is the mass density of soot [kg/m^3]. Next, the mass of the gas m_{gas} can be computed by subtracting the soot mass from the total reactor mass m_{tot}, or

$$m_{\text{gas}} = m_{\text{tot}} - m_{\text{soot}}. \tag{3.17}$$

The soot formation process adds two extra terms to the species conservation equa-

tion, resulting in the following expression for $\frac{dY_k}{dt}$

$$\frac{dY_k}{dt} = \frac{\dot{\omega}_k W_k}{\rho_{\text{gas}}} + \frac{\dot{m}_{\text{in}}}{m_{\text{gas}}}(Y_{k,\text{in}} - Y_k) + \left(\frac{dY_k}{dt}\right)_{\text{soot}} - Y_k \sum_{k=1}^{K} \left(\frac{dY_k}{dt}\right)_{\text{soot}}, \tag{3.18}$$

where $(\frac{dY_k}{dt})_{\text{soot}}$ represents the change in mass fractions in the gas due to species transitioning from the gas phase to the solid soot phase (and vice versa).

The equation for the temperature is derived in three steps. In step 1, the equation for change of total enthalpy (H) at constant pressure, given by [64]

$$\frac{dH}{dt} = -\dot{Q} + \sum_{\text{in}} \dot{m}_{\text{gas,in}} h_{\text{in}} - h \sum_{\text{out}} \dot{m}_{\text{out}}, \tag{3.19}$$

is modified by assuming the total rate of heat transfer through all walls $\dot{Q}$ [J/s] to be equal to zero and splitting $\dot{m}_{\text{out}}$ into a part consisting of gas ($\dot{m}_{\text{gas}}$) and a part consisting of soot ($\dot{m}_{\text{soot}}$). The resulting equation for the change in total enthalpy is

$$\frac{dH}{dt} = \dot{m}_{\text{in}} h_{\text{in}} - h_{\text{gas}} \dot{m}_{\text{gas,out}} - h_{\text{soot}} \dot{m}_{\text{soot,out}}, \tag{3.20}$$

where the specific enthalpy of soot h_{soot} is calculated using

$$h_{\text{soot}} = h_{\text{soot,ref}} + c_{p,\text{soot}}(T - T_{\text{ref}}). \tag{3.21}$$

$h_{\text{soot,ref}}$ is assumed to be equal to the specific enthalpy of graphite at T_{ref} (= 298 K) since soot and graphite have similar sheet-like molecular structures [33]. $c_{p,\text{soot}}$ is assumed to be equal to be 840 J/(kg·K) [115].

In step 2, the equation for the total enthalpy, given by [64]

$$H = m \sum_{k=1}^{K} Y_k h_k, \tag{3.22}$$

is expanded to include soot, resulting in

$$H = m_{\text{gas}} \sum_{k=1}^{K} Y_k h_k + m_{\text{soot}} h_{\text{soot}}. \tag{3.23}$$

In order to be able to use the result from step 1, the derivative of the total enthalpy with respect to time is computed as follows

$$\frac{dH}{dt} = h_{\text{gas}} \frac{dm_{\text{gas}}}{dt} + h_{\text{soot}} \frac{dm_{\text{soot}}}{dt} + (m_{\text{gas}} c_{p,\text{gas}} + m_{\text{soot}} c_{p,\text{soot}}) \frac{dT}{dt} + m_{\text{gas}} \sum_{k=1}^{K} h_k \frac{dY_k}{dt}, \tag{3.24}$$

where h is rewritten as $c_p \Delta T$. The time derivates of m_{gas} and m_{soot} are expanded using

$$\frac{dm_{\text{gas}}}{dt} = \dot{m}_{\text{gas,in}} - \dot{m}_{\text{gas,out}} + (\dot{m}_{\text{gas}})_{\text{soot}}, \tag{3.25}$$

and

$$\frac{dm_{\text{soot}}}{dt} = -\dot{m}_{\text{soot,out}} + (\dot{m}_{\text{soot}})_{\text{soot}}, \tag{3.26}$$

where $(\dot{m}_{\text{gas}})_{\text{soot}}$ is the total mass (in kg) of soot turning into gas on a per second basis. $(\dot{m}_{\text{soot}})_{\text{soot}}$, representing the amount of gas turning into soot [kg/s], is then defined as

$$(\dot{m}_{\text{soot}})_{\text{soot}} = -(\dot{m}_{\text{gas}})_{\text{soot}} = -m_{\text{gas}} \sum_{k=1}^{K} \left(\frac{dY_k}{dt} \right)_{\text{soot}}. \tag{3.27}$$

In step 3, Equations 3.20 and 3.24 are combined to arrive at an expression for $\frac{dT}{dt}$. First the two expressions for $\frac{dH}{dt}$ are set to be equal to each other, resulting in

$$
\begin{aligned}
-(m_{\text{gas}}c_{p,\text{gas}} + m_{\text{soot}}c_{p,\text{soot}})\frac{dT}{dt} = \quad & h_{\text{gas}}(\dot{m}_{\text{gas,in}} - \dot{m}_{\text{gas,out}} + (\dot{m}_{\text{gas}})_{\text{soot}}) \\
& + h_{\text{soot}}(-\dot{m}_{\text{soot,out}} + (\dot{m}_{\text{soot}})_{\text{soot}}) \\
& + m_{\text{gas}}\sum_{k=1}^{K} h_k \frac{dY_k}{dt} - \dot{m}_{\text{gas,in}}h_{\text{gas,in}} \\
& + h_{\text{gas}}\dot{m}_{\text{gas,out}} + h_{\text{soot}}\dot{m}_{\text{soot,out}}.
\end{aligned} \tag{3.28}
$$

Then, Equation 3.18 is substituted into Equation 3.28, leading to

$$
\begin{aligned}
-(m_{\text{gas}}c_{p,\text{gas}} + m_{\text{soot}}c_{p,\text{soot}})\frac{dT}{dt} = & \; h_{\text{gas}}(\dot{m}_{\text{gas,in}} - \dot{m}_{\text{gas,out}} + (\dot{m}_{\text{gas}})_{\text{soot}}) \\
& + h_{\text{soot}}(-\dot{m}_{\text{soot,out}} + (\dot{m}_{\text{soot}})_{\text{soot}}) \\
& + \frac{m_{\text{gas}}}{m_{\text{gas}}}\sum_{k=1}^{K} h_k \Bigg[\dot{\omega}W_k V_{\text{PZ}} + \dot{m}_{\text{gas,in}}(Y_{k,\text{in}} - Y_k) \\
& + m_{\text{gas}}\left(\frac{dY_k}{dt}\right)_{\text{soot}} - Y_k(\dot{m}_{\text{gas}})_{\text{soot}}\Bigg] \\
& + h_{\text{gas}}\dot{m}_{\text{gas,out}} + h_{\text{soot}}\dot{m}_{\text{soot,out}} - \dot{m}_{\text{gas,in}}h_{\text{gas,in}}.
\end{aligned} \tag{3.29}
$$

Lastly, using

$$
\sum_{k=1}^{K} h_k Y_k = h_{\text{gas}}, \tag{3.30}
$$

a final expression for $\frac{dT}{dt}$ is obtained, given by

$$
\begin{aligned}
(m_{\text{gas}}c_{p,\text{gas}} + m_{\text{soot}}c_{p,\text{soot}})\frac{dT}{dt} = \quad & -h_{\text{soot}}(\dot{m}_{\text{soot}})_{\text{soot}} - \sum_{k=1}^{K} h_k(\dot{m}_{k,\text{gen}}) \\
& + \dot{m}_{\text{gas,in}}\left(h_{\text{gas,in}} - \sum_{k=1}^{K} h_k Y_k\right) \\
& - \sum_{k=1}^{K} h_k m_{\text{gas}}\left(\frac{dY_k}{dt}\right)_{\text{soot}}.
\end{aligned} \tag{3.31}
$$

Two extra equations are solved for the primary zone with soot. These two equa-

tions represent the change in N and M over time. The equation for N is given by

$$\frac{dN}{dt} = \left(\frac{dN}{dt}\right)_{\text{mech}} + \left(\frac{dN}{dt}\right)_{\dot{m}}, \tag{3.32}$$

where the first term represents the soot-mechanism specific term $\left(\frac{dN}{dt}\right)_{\text{mech}}$ as defined in Chapter 2. The second term of Equation 3.32 represents a general term accounting for the decrease in N due to soot leaving the reactor with the outgoing massflow. It is defined as

$$\left(\frac{dN}{dt}\right)_{\dot{m}} = -\frac{\dot{m}_{\text{out}}}{\rho_{\text{tot}} V_{\text{PZ}}} N. \tag{3.33}$$

Similarly, the general equation for M is given by

$$\frac{dM}{dt} = \left(\frac{dM}{dt}\right)_{\text{mech}} + \left(\frac{dM}{dt}\right)_{\dot{m}}, \tag{3.34}$$

where the soot-mechanism specific term $\left(\frac{dM}{dt}\right)_{\text{mech}}$ as defined in Chapter 2 is again used. The second term is calculated as

$$\left(\frac{dM}{dt}\right)_{\dot{m}} = -\frac{\dot{m}_{\text{out}}}{\rho_{\text{tot}} V_{\text{PZ}}} M. \tag{3.35}$$

3.3 Secondary Zone Equations

The secondary zone is modeled as a plug flow reactor, which represents a steady-state channel where the mixture flows in the positive z-direction and the gas is considered to be completely homogeneous perpendicular to this flow direction [64]. The composition of the gas changes in the flow direction but all diffusion processes are neglected [64]. In this section, the equations for the model without soot are discussed first, followed by the extended set of equations used for the model with soot.

3.3.1 Secondary Zone Without Soot

The equations for the conservation of mass, species and energy are different for a plug flow reactor compared to a well-stirred reactor used in the primary zone, in particular integrating in space rather than in time. Since pressure and cross-sectional area are assumed to be constant throughout the secondary zone and it is also assumed that no species formation at the wall occurs, no additional equation for momentum in the axial direction needs to be solved.

The change in total mass flow in the secondary zone is caused by adding secondary and dilution air to the mixture in the reactor. The rate at which this insertion happens is expressed by $\beta_{\text{air,in}}$ [kg/(m·s)]. The mass (flow) conservation equation is consequently written as

$$\frac{d\dot{m}_{\text{gas}}}{dz} = \beta_{\text{air,in}}. \tag{3.36}$$

A general form of the species conservation for a PFR is used as starting point. It is expressed by [64]

$$\rho u \frac{dY_k}{dz} + Y_k P' \sum_{k=1}^{K} \dot{s}_k W_k = \dot{\omega}_k W_k + P' \dot{s}_k W_k, \tag{3.37}$$

where u is the axial velocity [m/s], $\dot{s}_k$ is the molar rate of formation of species k at the wall [kmol/(m^{2}s)] and P' is the chemically active channel perimeter [m]. When neglecting the wall terms as well as adding a term for $\beta_{\text{air,in}}$, the species conservation equation for the secondary zone without soot is

$$\frac{dY_k}{dz} = \frac{\beta_{\text{air,in}}(Y_{k,\text{in}} - Y_k)}{\rho_{\text{gas}} u A_{\text{SZ}}} + \frac{\dot{\omega} W_k}{\rho_{\text{gas}} u}. \tag{3.38}$$

Similarly, the equation for the temperature is derived using a general form of the temperature equation in a plug flow reactor expressed by [64]

$$\rho u A_{\text{SZ}} c_p \frac{dT}{dz} = -A_{\text{SZ}} \sum_{k=1}^{K} h_k \dot{\omega}_k W_k - P' \sum_{k=1}^{K} h_k \dot{s}_k W_k + UP(T_w - T), \tag{3.39}$$

where U is the heat transfer coefficient [W/(mK)] and T_w is the wall temperature [K]. When dropping the wall terms and adding a $\beta_{\text{air,in}}$ term, the resulting energy equation is

$$\begin{aligned}\dot{m}_{\text{gas}} c_{p,\text{gas}} \frac{dT}{dz} = &- A_{\text{SZ}} \sum_{k=1}^{K} h_k \dot{\omega}_k W_k \\ &+ \beta_{\text{air,in}} \left(h_{\text{air,in}} - \sum_{k=1}^{K} h_k Y_{k,\text{in}} \right).\end{aligned} \tag{3.40}$$

3.3.2 Secondary Zone With Soot

For the secondary zone with soot, a total of six main equations are solved in space (z). A major difference compared to the primary zone with soot is that the model solves for the soot mass flow $\dot{m}_{\text{soot}}$ [kg/s] and number flow $\dot{n}_{\text{soot}}$ [particles/s] instead of M and N. The conservation of total mass (flow) is defined as

$$\frac{d\dot{m}_{\text{tot}}}{dz} = \beta_{\text{air,in}}. \tag{3.41}$$

This is identical to the secondary zone without soot, except that the total mass flow now consists of both gas and solid soot. In order to distinguish between these two, a second expression, describing the change of the mass flow of soot, is formulated as

$$\frac{d\dot{m}_{\text{soot}}}{dz} = \frac{dM}{dt} A_{\text{SZ}}, \tag{3.42}$$

with

$$\frac{dM}{dt} = \left(\frac{dM}{dt} \right)_{\text{mech}}. \tag{3.43}$$

The mass flow of gas is then computed using

$$\dot{m}_{\text{gas}} = \dot{m}_{\text{tot}} - \dot{m}_{\text{soot}}. \tag{3.44}$$

The soot number flow is computed in a similar way as the soot mass flow, using

$$\frac{d\dot{m}_{\text{soot}}}{dz} = \frac{dN}{dt} A_{\text{SZ}}, \tag{3.45}$$

with

$$\frac{dN}{dt} = \left(\frac{dN}{dt}\right)_{\text{mech}}, \tag{3.46}$$

Using a volume flow $\dot{V}$ [m^3/s], defined as

$$\dot{V} = \frac{\dot{m}_{\text{gas}}}{\rho_{\text{gas}}}, \tag{3.47}$$

M and N in the secondary zone are computed using

$$M = \frac{\dot{m}_{\text{soot}}}{\dot{V}}, \tag{3.48}$$

and

$$N = \frac{\dot{n}_{\text{soot}}}{\dot{V}}. \tag{3.49}$$

Compared to the equation for $\frac{dY}{dz}$ in the case without soot, two extra terms are included to account for the formation and destruction of soot particles. The resulting expression is given by

$$\frac{dY_k}{dz} = \frac{\beta_{\text{air,in}}(Y_{k,\text{in}} - Y_k)}{\rho_{\text{gas}} u A_{\text{SZ}}} + \frac{\dot{\omega} W_k}{\rho_{\text{gas}} u} + \frac{1}{u}\left(\frac{dY_k}{dt}\right)_{\text{soot}} - \frac{Y_k}{u}\sum_{k=1}^{K}\left(\frac{dY_k}{dt}\right)_{\text{soot}}, \tag{3.50}$$

The velocity u is calculated using

$$u = \frac{\dot{m}_{\text{gas}}}{\rho_{\text{gas}} A_{\text{SZ}}}. \tag{3.51}$$

Similarly to the equation for species conservation, the energy equation is also expanded with two soot-specific terms resulting in the following expression

$$(\dot{m}_{\text{gas}}c_{p,\text{gas}} + \dot{m}_{\text{soot}}c_{p,\text{soot}})\frac{dT}{dz} = -A_{\text{SZ}}\sum_{k=1}^{K} h_k\dot{\omega}_k W_k - A_{\text{SZ}}\rho_{\text{gas}}\sum_{k=1}^{K} h_k\left(\frac{dY_k}{dt}\right)_{\text{soot}} - A_{\text{SZ}}h_{\text{soot}}\frac{dM}{dt} + \beta_{\text{air,in}}\left(h_{\text{air,in}} - \sum_{k=1}^{K} h_k Y_{k,\text{in}}\right). \tag{3.52}$$

3.4 Gas-Solid Phase Interactions

As soot forms and oxidizes, interactions between the gas phase and the solid soot phase take place. More specifically, carbon moves from the gas phase to the solid phase as soot is formed, whereas the opposite happens during oxidation. In order to conserve energy and to accurately model PAH, C_2H_2, O_2, OH and O concentrations, these phase interactions must be accounted for. Figure 3-3 illustrates the phase interactions taking place in the model.

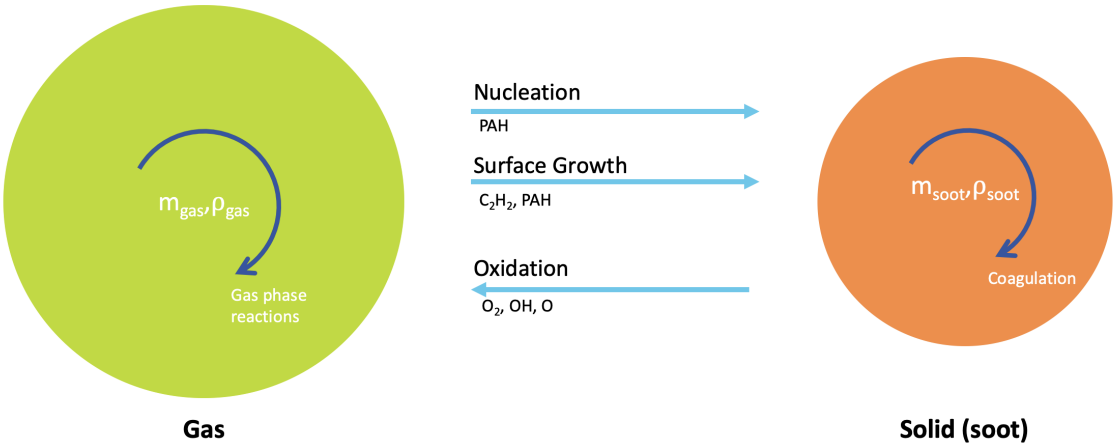

Figure 3-3: Overview of interactions between the gas phase and solid (soot) phase. Arrows indicate carbon atoms moving from one phase to another through reactions with the species listed.

The method of capturing the phase interactions consists of two parts. First, the rates of change of mass fractions of the reacting gas species ($\frac{dY_k}{dt}$) are adjusted according to the rate of soot formation. This process is illustrated as follows

$$\left(\frac{dY_k}{dt}\right)_{\text{soot}} = -\left(\frac{dM}{dt}\right)_k \frac{W_k k_f}{\rho_{\text{gas}} W_C}, \tag{3.53}$$

where $(\frac{dM}{dt})_k$ represents the rate of change in soot mass density due to reactions with species k of the soot formation process (e.g. surface growth through C_2H_2). Furthermore, W_C represents the atomic weight of carbon [kg/kmol], W_k the molecular weight of species k [kg/kmol] and k_f the molar ratio in which species k reacts to form or destroy soot (0.5 for surface growth through C_2H_2).

The second part of modeling the phase interactions assures that the sum of all the mass fractions remains equal to 1. The last term in Equations 3.18 and 3.50 is responsible for this. This term decreases the values for Y_k in the case of net soot depletion and increases the Y_k values in the case of net soot formation. The magnitude of the increase or decrease for species k is proportional to Y_k.

3.5 Gas Phase Mechanism

The gas phase chemistry inside the combustor is modeled using a kinetic mechanism. This mechanism determines the structure of the flame and specifies the species profile [116]. A Polimi high temperature kinetic mechanism for transportation fuels (POLIMI_PRF_PAH_RFUELS_HT_1412), consisting of 218 species and 7047 reactions, is used because it contains a relatively large amount of PAH species as well as the chemical pathways for their formation from the molecules found in jet fuel [117]. The NO_x reactions from GRI-Mech 3.0 were added to the kinetic mechanism [118]. Table 3.3 provides a list of the PAH species present in the gas phase mechanism.

3.6 Fuel Modeling

Jet fuel consists of thousands of chemical species, making it complicated and computationally expensive to model [119]. Therefore, Jet A surrogates from literature are used in the model. In order to accurately model the aircraft combustion process, the surrogate fuels used in the model must have similar gas phase combustion properties

Table 3.3: Overview of the PAH species in the kinetic mechanism, including their radicals between parentheses.

Name	**Formula**
Naphthalene	$C_{10}H_8$ ($C_{10}H_7$)
Acenaphthylene	$C_{12}H_8$ ($C_{12}H_7$)
Biphenyl	$C_{12}H_{10}$ ($C_{12}H_9$)
Fluorene	$C_{13}H_{10}$
Phenathrene	$C_{14}H_{10}$ ($C_{14}H_9$)
Pyrene	$C_{16}H_{10}$ ($C_{16}H_9$)

compared to Jet A fuel commonly used in aircraft. These properties include, amongst others, heating value, average carbon number, molecular weight, overall reactivity and sooting tendencies [120, 121].

Table 3.4 provides an overview of the compositions of the five jet fuel surrogates (S1 - S5) used in the model. The surrogates from literature are slightly altered by directly adding naphthalene to the fuel, as illustrated by the bottom row of Table 3.4. The mole fraction of naphthalene in the fuel (X_{naph}) is set equal to 0.02 for regular jet fuel [122].

Two methods of reducing naphthalene content in jet fuel are simulated: extractive distillation and hydrotreating. In the former, naphthalene is selectively removed from jet fuel using a polar solvent. To simulate this, the mole fractions of the species in the surrogate representing the naphthalene-depleted jet fuel (ND) are increased proportionally with respect to their baseline value X using

$$X_{\text{ND}} = \frac{X}{1 - X_{\text{naph}}}. \tag{3.54}$$

During hydrotreating, naphthalene is saturated and turned into tetralin (monoaromatic). This process is copied in the fuel modeling by adding tetralin to the surrogate.

When modeling the effects of using biofuels, the surrogates are adjusted to represent biofuel blends. The adjusted mole fractions resulting from turning a surrogate consisting of a total of I nonaromatic species and J aromatic species into a blend

Table 3.4: Jet fuel surrogates (S1–S5) composition in mole fractions.

Species	S1 [120]	S2 [121]	S3 [123]	S4 [123]	S5 [119]
n-dodecane	0.404	0.303	0.384	0.290	0.371
iso-octane	0.295	-	-	-	0.020
1,3,5-trimethylbenzene	0.073	-	-	-	-
n-propylbenzene	0.228	-	-	-	-
methylcyclohexane	-	0.485	0.234	-	-
m-xylene	-	0.212	-	-	-
iso-cetane	-	-	0.148	0.142	0.206
toluene	-	-	0.234	0.249	0.259
decalin	-	-	-	0.319	0.145
napthalene	X_{naph}	X_{naph}	X_{naph}	X_{naph}	X_{naph}

with a biofuel mole fraction of p are calculated using

$$\begin{aligned} X_{i,\text{bio}} &= X_i \left[1 + p \left(\frac{\sum_{j=1}^{J} X_j}{\sum_{i=1}^{I} X_i} \right) \right] \\ X_{j,\text{bio}} &= X_j (1 - p). \end{aligned} \tag{3.55}$$

3.7 Engine Conditions Inputs

Next to the input conditions related to the architecture of the combustor and the fuel inputs, another set of model inputs is related to the operating conditions of the engine. These include the pressure and temperature at the combustor entrance (P_3 and T_3), as well as the total mass flows of fuel and air in the combustor ($\dot{m}_{\text{fuel}}$ and $\dot{m}_{\text{air}}$). A detailed engine model developed in PyCycle that matches fuel flows, thrust levels and pressure ratios from the EDB is used to generate the engine input conditions [124, 125].

The combustor input conditions generated with the engine model are summarized in Figure 3-4. The fuel flow from the engine model closely matches the values in the EDB, with the exception of a slight deviation below approximately 10% thrust.

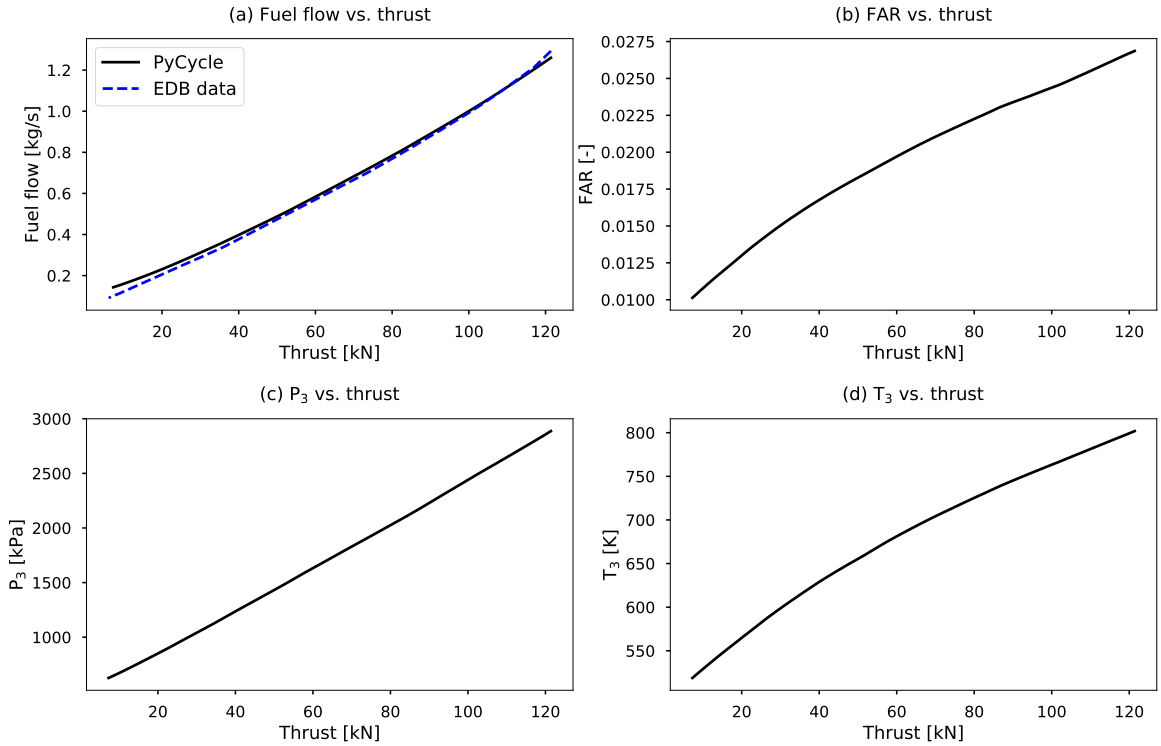

Figure 3-4: Model input data generated by the engine model: (a) fuel flow (b) FAR (c) P_3 and (d) T_3.

T_3 coming from the engine model only contains information about the incoming air, and not about the fuel. However, fuel enters as a liquid and its temperature does not increase when it is compressed (like it does for air). Therefore, it can be assumed that fuel enters the combustor at standard conditions. However, the fuel in the combustor model is vaporized and T_3 must therefore be corrected for vaporization of the fuel. This is done in the combustor model by adjusting the specific enthalpy of the gas-fuel mixture as follows

$$h_{\text{mix}} = \frac{1}{\dot{m}_{\text{mix}}}\left[\dot{m}_{\text{air}} h_{\text{air},P_3T3} + \dot{m}_{\text{fuel}} h_{\text{fuel},P_3T_3} - \dot{m}_{\text{fuel}}(L + \Delta h)\right], \tag{3.56}$$

where L represents the enthalpy of vaporization [J/kg] at standard conditions (T = 298.15 K and P = 101,325 Pa) and Δh is the change in specific enthalpy going from standard conditions to T_3 and P_3.

3.8 Model Parameter Calibration

Data from the International Civil Aviation Organization (ICAO) engine emissions databank (EDB) is used to calibrate the combustor model. The EDB contains reported sea level emission indices corrected to international standard atmosphere (ISA) conditions at four specified thrust settings representing the LTO cycle: 100% thrust (takeoff), 85% thrust (climbout), 30% thrust (approach) and 7% thrust (idle).

A subset of EDB data is used to tune six parameters to make the combustor model represent the CFM56 Tech Insertion combustor. The parameters include $\phi_{\mathrm{PZ,des}}$, V_{PZ} and S_{PZ} which characterize the primary zone, and $\phi_{\mathrm{SZ,des}}$, $\ell_{\mathrm{SA,SM}}$ and $\ell_{\mathrm{SA,FM}}$, which characterize the secondary zone. These six parameters are considered to represent a specific combustor design and the combustor model can be used to represent different (RQL) combustors by changing the values of these parameters based on EDB data for these different combustors.

Since the combustor model can be considered a "black box" function and obtaining a (numerical) gradient is computationally expensive, gradient-free optimization is used to calibrate the model parameters. More specifically, the DIvided RECTangles (DIRECT) method is applied [126]. This global optimization method searches the complete design space by using a hyperdimensional adaptive meshing scheme [126]. The DIRECT method is selected because it rigorously searches through the design space by balancing local and global searches [127]. This is considered important as large gradients and a relatively large number of local minima, caused by the complex relations between the design parameters, are observed when sampling parts of the design space. Furthermore, the relatively low dimensionality of the problem (6) and function evaluation times in the order of minutes make the problem suitable for the use of the DIRECT method [127, 128].

3.9 Model Input Summary

Table 3.5 shows a summary of all the input parameters for the combustor model. The variables are split up into two categories: fixed and calibrated. The former represents variables which are set based on data in literature and are held constant. On the other hand, the group of calibrated parameters consists of the variables which are calibrated based on the available measurement data. There are two groups of calibrated parameters. The first group, described in Section 3.8, is related to the combustor design. The second group, described in Section 2.9, considers the parameters that are varied in generating different soot model configurations.

Table 3.5: Overview of the combustor model input variables.

Combustor Model Inputs				**Fuel Inputs**	**Engine Model Inputs**	**Soot Model Inputs**	
Primary Zone		**Secondary Zone**				Fixed	Calibrated
Fixed	Calibrated	Fixed	Calibrated				
N_{PZ}	$\phi_{\mathrm{PZ,des}}$	A_{SZ}	$\phi_{\mathrm{SZ,des}}$	$\mathrm{X}_{\mathrm{naph}}$	$\dot{m}_{\mathrm{fuel}}$	$c_{p,\mathrm{soot}}$	$\mathrm{nuc}_{\mathrm{fac}}$
	S_{PZ}	L_{SZ}	$\ell_{\mathrm{SA,SM}}$	S1-S5	$\dot{m}_{\mathrm{air}}$	$\mathrm{h}_{\mathrm{ref,soot}}$	$\mathrm{coag}_{\mathrm{fac}}$
	V_{PZ}	$\ell_{\mathrm{DA,start}}$	$\ell_{\mathrm{SA,FM}}$		P_3		$\mathrm{sg}_{\mathrm{fac}}$
		$\ell_{\mathrm{DA,end}}$			T_3		$\mathrm{ox}_{\mathrm{fac}}$
		f_{SM}					$\mathrm{ox}_{\mathrm{num,fac}}$
							sg species
							HACA
							η_{OH}

Chapter 4

Results

The first two parts of this chapter (Sections 4.1 and 4.2) give an overview of the model NO_x, CO and soot predictions, and show the development of emissions, equivalence ratios and temperatures throughout the primary and secondary zone. The third and fourth part (Sections 4.3 and 4.4) each describe results from specific applications of the model. The former quantifies the effects of removing naphthalene from jet fuel, as well as using 50:50 biofuel blends. The latter predicts emissions at cruise.

4.1 NO_x and CO Emissions

4.1.1 Overview

The calibrated model coefficients obtained using NO_x and CO emissions data from the EDB, as described in Chapter 3, are shown in Table 4.1.

Table 4.1: Values of the six calibrated model parameters for the CFM56-7B Tech Insertion combustor.

V_{PZ}	$\phi_{PZ,des}$	S_{PZ}	$\phi_{SZ,des}$	$\ell_{SA,SM}$	$\ell_{SA,FM}$
0.0023 m^3	1.77	0.39	0.70	0.55	0.055

The resulting NO_x and CO predictions are shown Figure 4-1. The model captures the emission trends for both NO_x and CO, with modeled NO_x predictions within 9%

of measurements for all thrust settings. Model CO predictions are within 12% of measurements for thrust settings below 25% and show an average relative error of 32% for thrust settings above 25%. The resulting mean absolute error (MAE) values for NO_x and CO are 0.24 and 0.52, with root mean squared error (RMSE) values of 0.41 (0.22 without 100% thrust point) and 1.0, respectively.

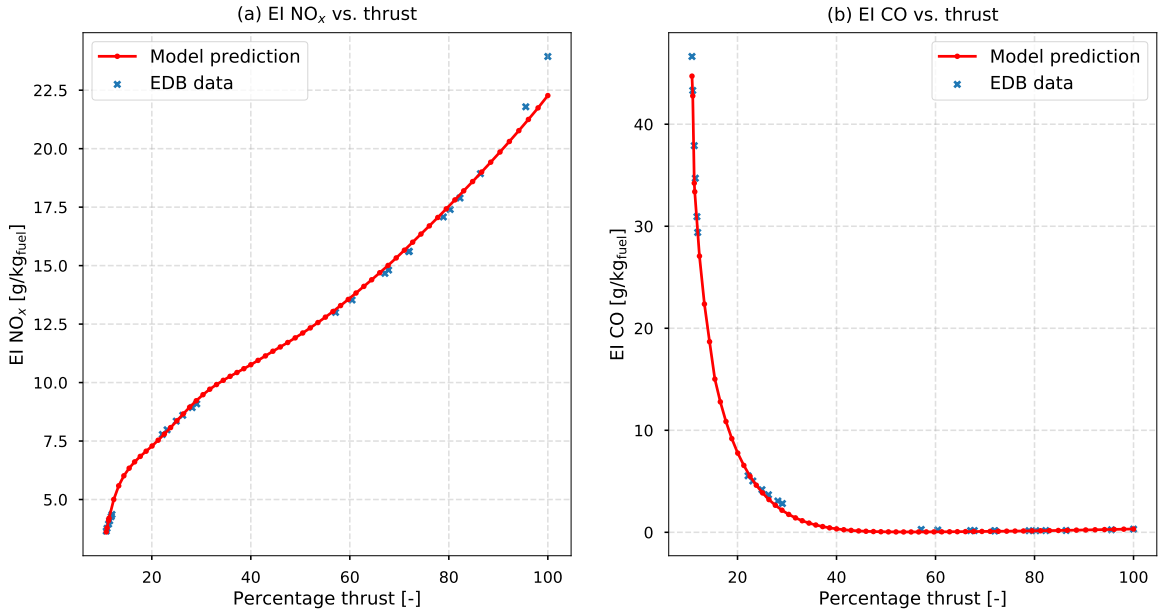

Figure 4-1: Comparison of model (a) NO_x and (b) CO predictions with EDB data.

4.1.2 Primary Zone Analysis

A total of 21 primary zone reactors are selected as the maximum differences in EI observed after increasing the number of reactors beyond 21 are 1.3% for NO_x and 4.3% for CO, with average differences of 0.30% and 0.27% respectively.

Figure 4-2 shows the mean equivalence ratio in the primary zone as a function of thrust setting. The mean primary zone starts out rich ($\phi > 1$) and transitions from being rich to being lean ($\phi < 1$) around 25% thrust. This is in agreement with literature, which suggests that conditions in the primary zone are close to stoichiometric around approach (≈30% thrust) conditions [15].

The resulting distributions of mass flow per primary zone reactor i are shown for five thrust settings in Figure 4-3. The effect of the mixing parameter S_{PZ} is visible

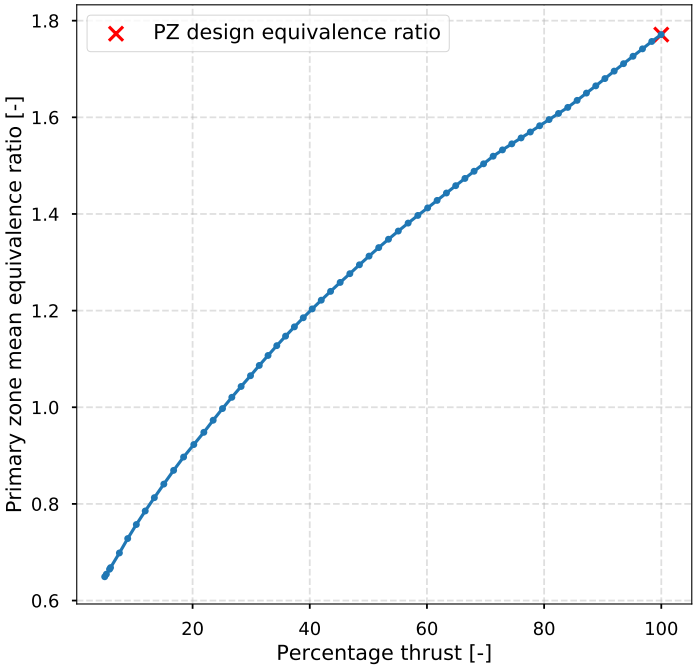

Figure 4-2: Mean primary zone equivalence ratio as function of percentage thrust.

as the standard deviation of the distribution increases with thrust setting (and thus increasing mean primary zone equivalence ratio).

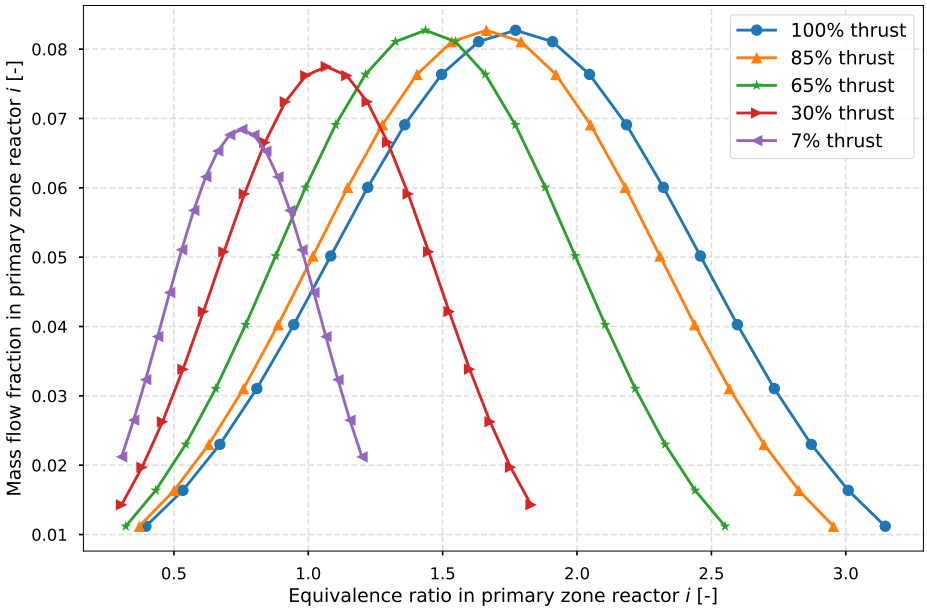

Figure 4-3: Division of mass flow between the 21 PZ reactors for five different thrust settings.

The different equivalence ratios and fuel flows in each reactor result in different

primary zone exit temperatures for each of the reactors. Figure 4-4 shows the exit temperatures of the 21 different reactors for the same five thrust settings. The exit temperature is observed to primarily be a function of equivalence ratio, in combination with thrust setting (and thus T_3). As expected, maximum temperatures occur at equivalence ratios between approximately 1.0 and 1.1. At equivalence ratios below 0.5, exit temperatures drop with ≈1000 K for the 7%, 30%, 65% and 85% thrust conditions. This is caused by blowout, at which no ignition of the fuel in one or more of the primary zone reactors occurs, and unburned fuel therefore enters the SZ. Blowout does not occur at 100% thrust as a result of a sufficiently high T_3 at equivalence ratios below 0.5.

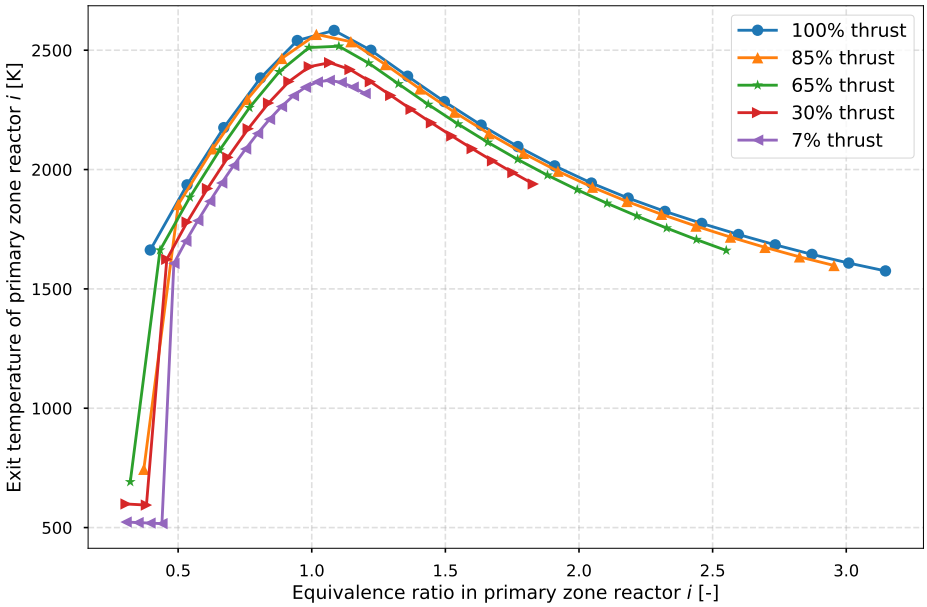

Figure 4-4: Exit temperatures of the 21 PZ reactors for five different thrust settings.

Figure 4-5 shows the emission index of NO_x at the primary zone exit for each individual reactor i. Peak NO_x formation is observed at $\phi \approx 1$, consistent with literature [112, 129].

Figure 4-6 presents the EI CO per reactor i. CO formation rates are observed to be impacted by both the equivalence ratio and the temperature inside the reactor, and show consistent behavior with previous literature [129]. Starting at $\phi \approx 0.5$, the relatively high rates of CO formation here are caused by relatively low temperatures,

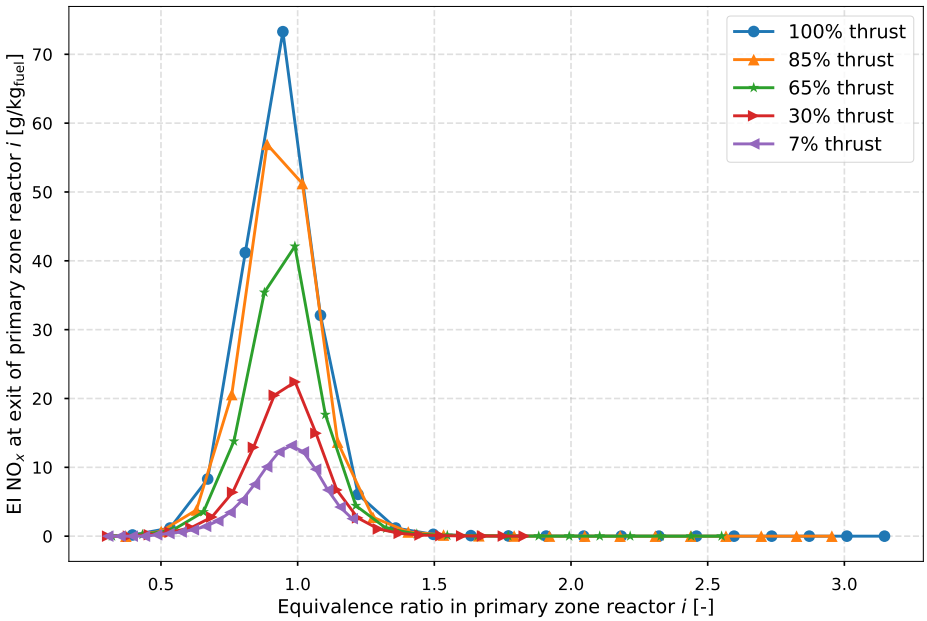

Figure 4-5: EI NO_x of the 21 PZ reactors for five different thrust settings.

resulting in relatively low oxidation rates of CO. As the equivalence ratio increases, CO formation in the primary zone decreases due to increasing temperatures and, correspondingly, higher CO oxidation rates. A minimum is observed at $\phi \approx 0.7$, which is consistent with a value of around 0.8 in literature [5]. Increasing the primary zone equivalence ratio beyond ≈ 0.7 increases the temperature, resulting in an approximately 200 times higher EI CO at $\phi \approx 1.5$ compared to $\phi \approx 0.7$. This is explained by the formation of CO by chemical dissociation of CO_2, which starts to become significant at temperatures above $\approx$1800 K [5]. The peak in CO formation is observed at $\phi \approx 1.75$, after which EI CO decreases. This decrease is ascribed to insufficient oxygen availability to form CO.

4.1.3 Secondary Zone Analysis

Table 4.2 contains an overview of the SZ parameters that are held constant and are thus not part of the calibration. The model is not restricted to a specific secondary zone length or cross-sectional area, as the parameters that affect emissions are the mixing volume and the temperature inside the mixing volume (mixing temperature). The mixing volume is defined as the volume in which mixing of secondary air with the

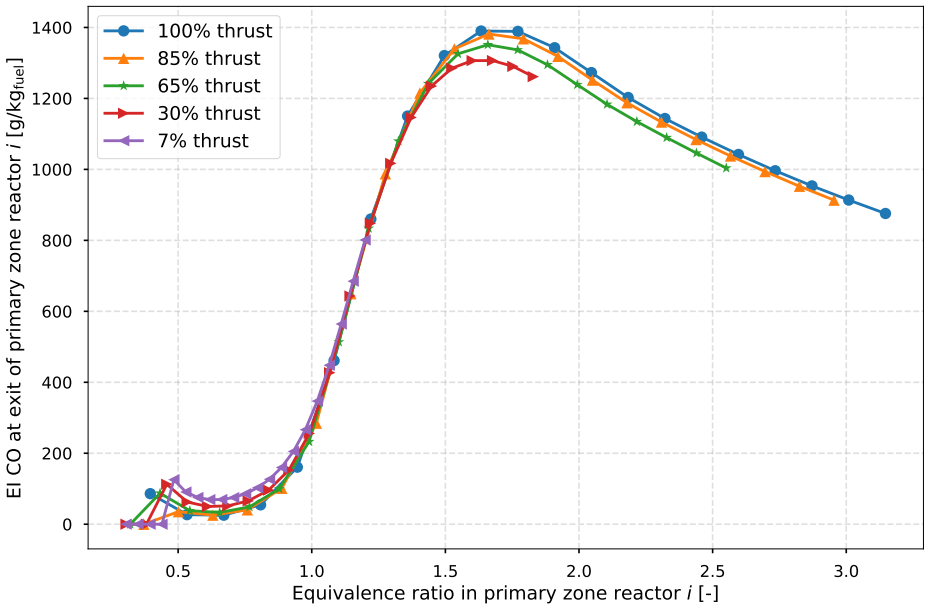

Figure 4-6: EI CO of the 21 PZ reactors for five different thrust settings.

combustion mixture occurs. It is determined by the fractions of secondary zone length over which secondary air is inserted ($\ell_{\mathrm{SA,SM}}$ and $\ell_{\mathrm{SA,FM}}$). The mixing temperature is regulated by the mass flow of secondary air, which is set by the design equivalence ratio in the secondary zone $\phi_{\mathrm{SZ,des}}$.

Table 4.2: Fixed SZ parameters.

A_{SZ}	L_{SZ}	$\ell_{\mathrm{DA,start}}$	$\ell_{\mathrm{DA,end}}$	f_{SM}
0.15 m^2	0.075 m	0.95	1.0	0.50

The development of the equivalence ratio throughout the secondary zone is shown for 100% and 7% thrust in Figure 4-7. Adding air to the mixture decreases the equivalence ratio in the SZ. For 100% thrust, this decrease changes the mixture from being rich, when entering the secondary zone, to being lean at the combustor exit. The transition from rich to lean is especially relevant as peak temperatures — and thus peak NO_x formation rates — occur when $\phi \approx 1$. For 7% thrust, the mixture starts out lean, so no rich-to-lean transition takes place in the SZ.

Peak temperatures in the SZ occurring at close to stoichiometric conditions ($\phi = 1$) for 100% thrust are visible in Figure 4-8. Peak temperatures for the 7% thrust case,

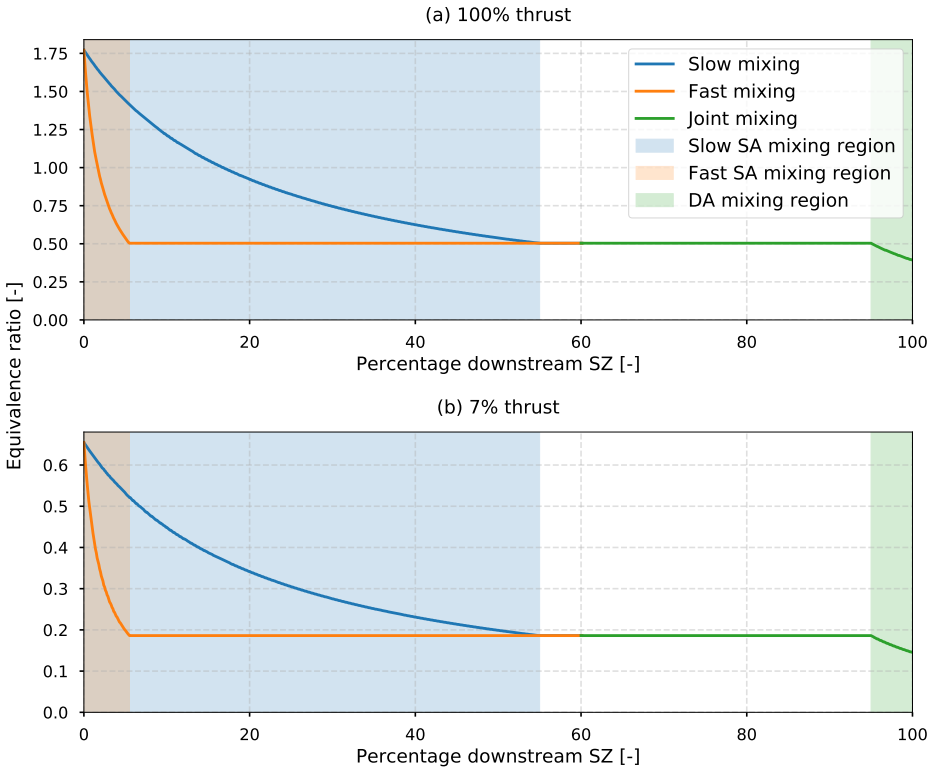

Figure 4-7: Comparison of equivalence ratio development throughout the SZ for (a) 100% thrust and (b) 7% thrust.

where no rich-to-lean transition takes place, are approximately 700 K lower than for 100% thrust. The temperature peak occurring at 7% thrust is explained by rich mixture pockets and unburned fuel coming in from the primary zone and burning up in the secondary zone.

The ≈1% difference between the temperatures at the end of the slow and fast mixing zones at 7% thrust is consistent with the difference in CO mass fractions between the flows exiting the two mixing zones.

Figure 4-9 shows the maximum temperatures in the combustor as a function of thrust. The curve can be split up into two parts: 0%–25% thrust and 25%–100% thrust. The split coincides with the thrust setting at which the mean equivalence ratio in the PZ is ≈ 1 (25% thrust). For equivalence ratios smaller than 1, there is no significant temperature peak in the SZ and therefore the maximum temperature is determined by the PZ exit temperature. For equivalence ratios larger than 1, the maximum temperature is determined by the temperature peak in the SZ. The

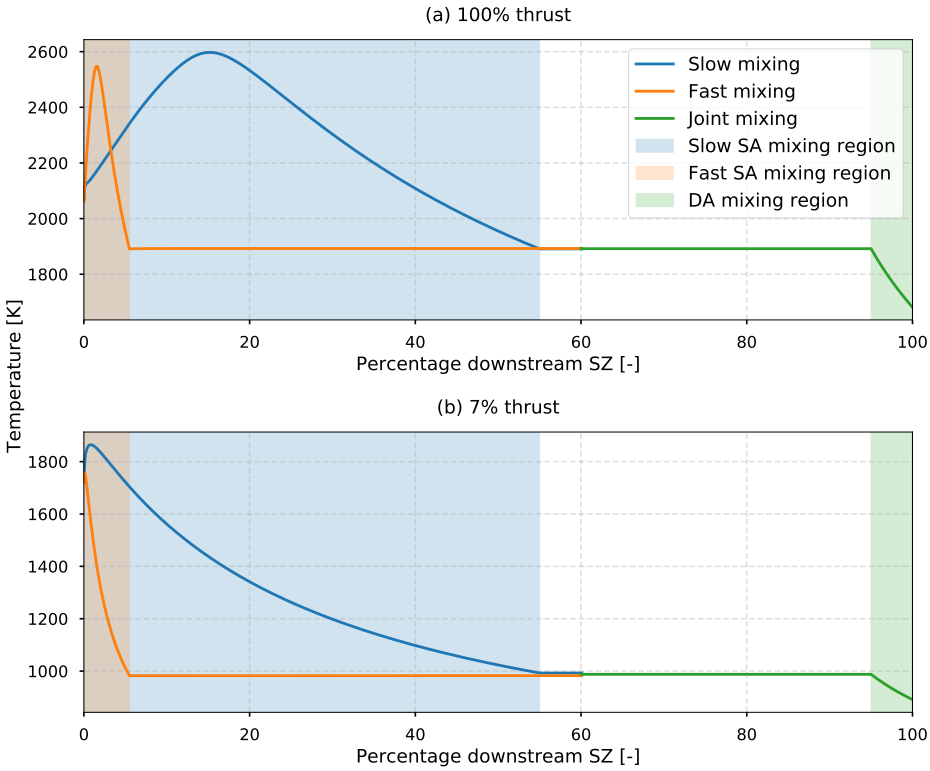

Figure 4-8: Comparison of temperature development throughout the SZ for (a) 100% thrust and (b) 7% thrust.

change in gradient in Figure 4-9 is consistent with the PZ exit temperature being more sensitive to the thrust setting than the peak temperatures in the SZ.

NO_x formation is found to increase with mixing volume and mixing temperature. The equivalence ratio and temperature development throughout the SZ can therefore be related to EI NO_x, as shown in Figure 4-10. For 100% thrust, approximately 80% of the NO_x is formed in the slow mixing zone of the SZ because of the ten times larger mixing volume here compared to the fast mixing zone. The decrease in SZ temperatures — and thus mixing temperatures — with decreasing thrust explains the lower EI NO_x values at 7% thrust compared to the 100% thrust scenario. Whereas the secondary zone is responsible for over 80% of NO_x emissions at 100% thrust, the relatively low SZ temperatures at 7% thrust cause a relatively low NO_x production in the secondary zone. As shown in Figure 4-10(b), over 95% of the NO_x at 7% thrust is formed in the primary zone.

Figure 4-11 shows that CO is mainly formed in the primary zone (>85%) and de-

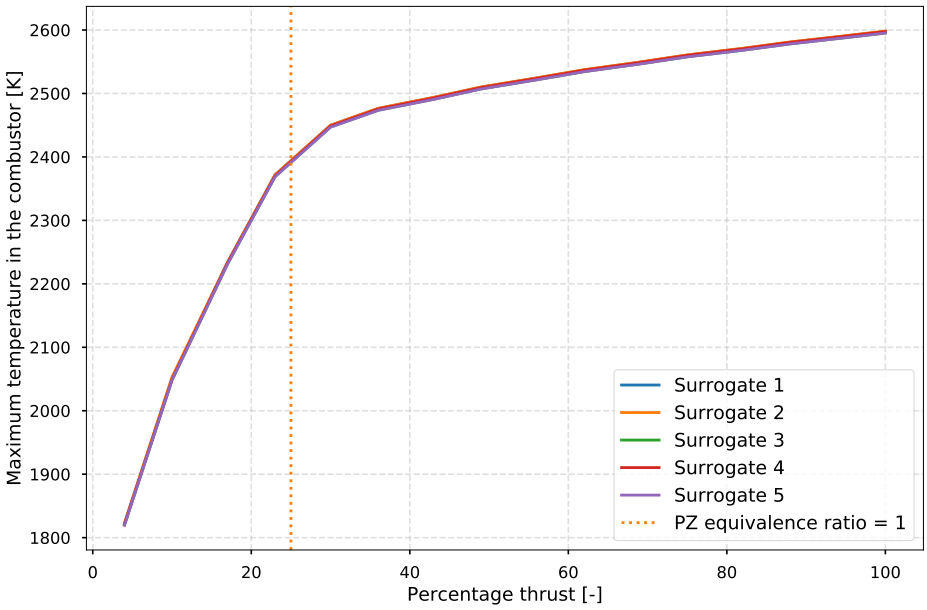

Figure 4-9: Maximum temperatures in the combustor as function of thrust setting for surrogates 1-5. All five surrogates fall onto the same line.

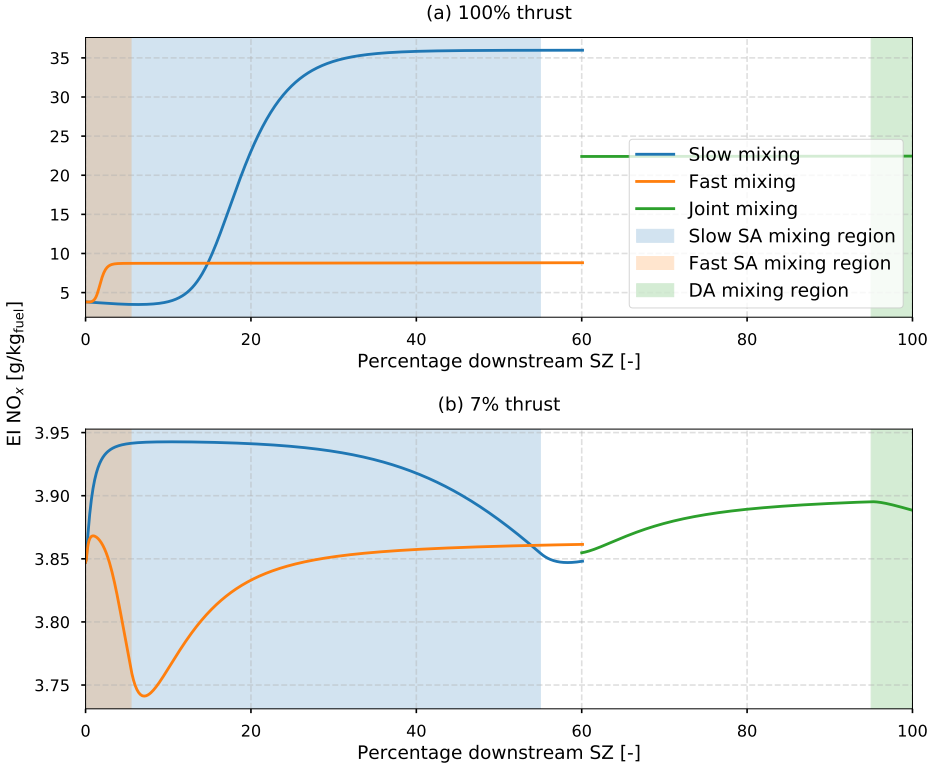

Figure 4-10: Comparison of EI NO_x development throughout the SZ for (a) 100% thrust and (b) 7% thrust.

pleted in the secondary zone. CO depletion increases with increasing mixing volumes and mixing temperatures. Therefore, CO emissions are highest at low thrust, where mixing temperatures are lowest. The amount of depletion ranges from approximately 80% at 7% thrust to over 99% at 100% thrust. Approximately 98% of the remaining CO at the combustor exit comes from the fast mixing zone.

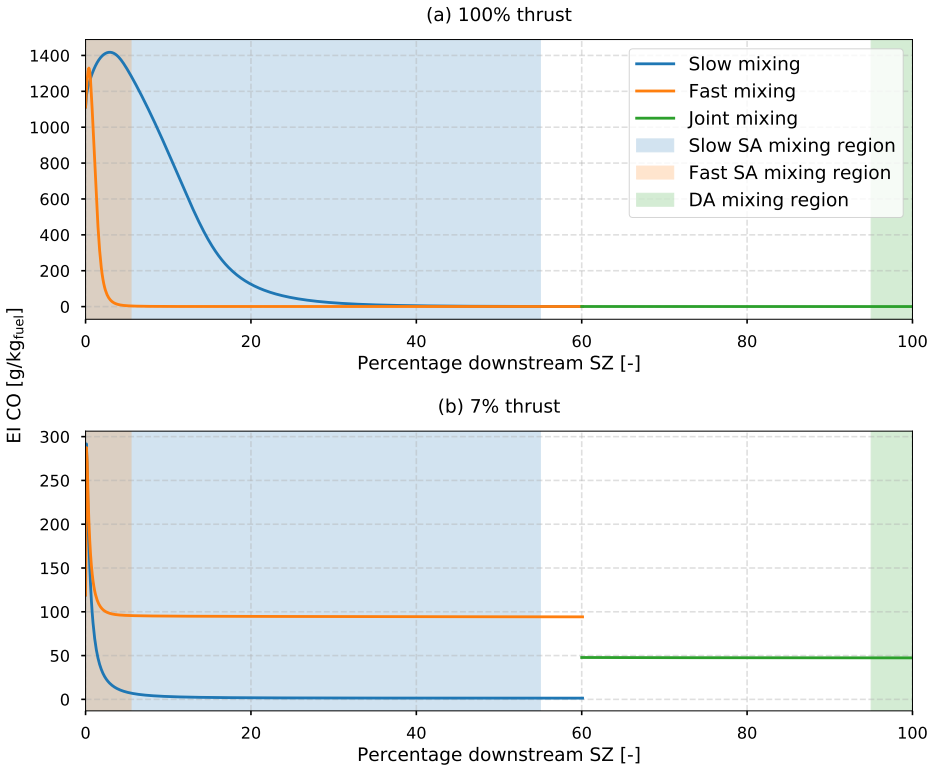

Figure 4-11: Comparison of EI CO development throughout the SZ for (a) 100% thrust and (b) 7% thrust.

To demonstrate the concept of the mixing volume, two secondary zones with different geometries but identical mixing volumes are compared. Figure 4-12 compares design A (baseline geometry) and design B ($A_{SZ}/1.5$). In order to compensate for the decrease in mixing volume due to the smaller cross-sectional area in design B, $\ell_{SA,SM}$ and $\ell_{SA,FM}$ are both multiplied by 1.5 such that the mixing volumes are the same as those in the baseline design. The resulting EI values for NO_x and CO at the combustor exit are within 0.2% of each other and are shown in Figure 4-12. The dilution zone volumes are not scaled here as their effect on NO_x and CO is observed to be $<$0.5%.

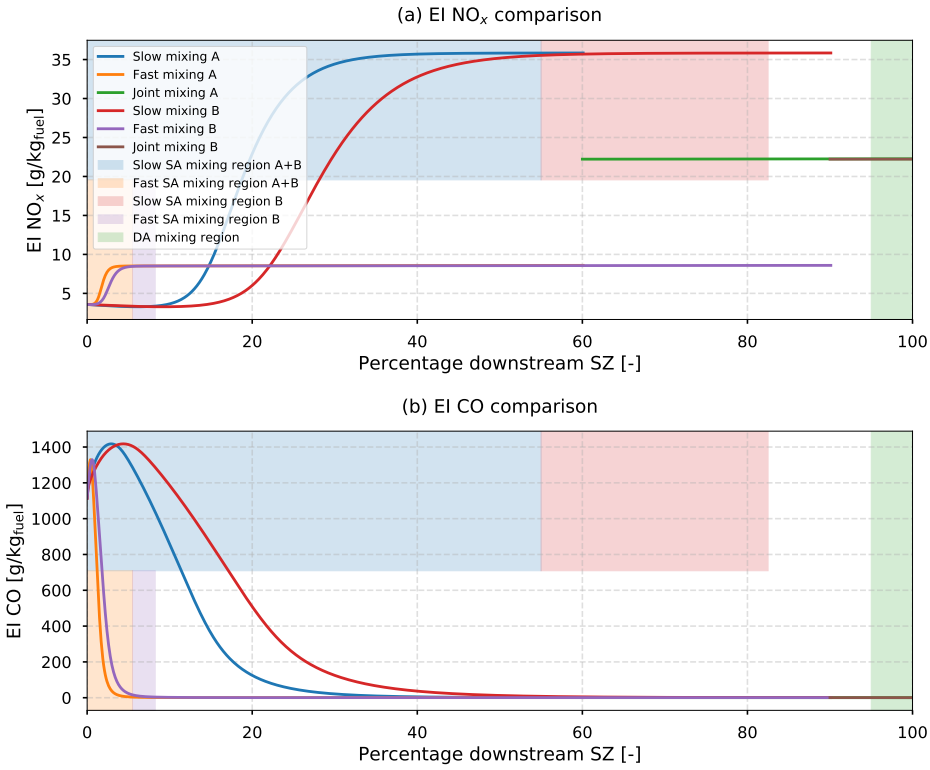

Figure 4-12: Comparison of (a) NO_x and (b) CO developments for combustor geometry A and combustor geometry B. Combustor geometry A represents the baseline combustor geometry. In combustor geometry B, A_{SZ} is divided by 1.5 and $\ell_{SA,SM}$ and $\ell_{SA,FM}$ are multiplied by 1.5.

Combining the primary and secondary zone analyses, the values of EI NO_x and EI CO in Figure 4-1 as well as their gradients, can be explained. The NO_x curve in Figure 4-1(a) can be divided into three parts: 0%–15% thrust, 15%–30% thrust and 30%–100% thrust. The gradient of the NO_x curve is highest in the first part, which is the consequence of blowout. As the PZ exit temperature of blowout reactors is ≈1000 K lower than the reactors without blowout, blowout disproportionately decreases the PZ exit temperature. This causes the PZ exit temperature, and thus the NO_x formation rate, to be most sensitive at thrust settings <15%, where ≈12% of the fuel enters the SZ unburned. Between 15%-30% thrust, the gradient decreases as a consequence of a decreasing number of reactors in which blowout occurs (≈5% of fuel mass). When transitioning from 15%-30% thrust to 30%-100% thrust, the SZ becomes the dominant origin of NO_x formation. The peak temperature in the SZ has a lower gradient for thrust settings >30% than for thrust settings <30% (Figure 4-9). As the

NO_x formation rate in the SZ depends on the SZ peak temperature, the gradient of EI NO_x decreases at the ≈30% thrust transition point as well.

The EI CO values in Figure 4-1(b) can be explained using the development of the maximum combustor temperature with thrust, as shown in 4-9. The higher the temperature in the SZ, the higher the CO depletion rates. The ratio of peak temperatures at 100% thrust and 60% thrust is 1.03 and the ratio of peak temperatures at 60% and 7% thrust is 1.4. This difference in maximum temperatures directly translates to the ratios of EI CO which are 1.3 (absolute difference of 0.08) for 100%/60% and 202 for 7%/60%. This two orders of magnitude difference in ratios is attributed to the decrease in combustor peak temperatures when going from 60% to 7% thrust, as shown in Figure 4-9.

4.2 Soot Emissions

4.2.1 Overview

Six different soot model configurations (C1 – C6) are developed. Each configuration consists of a different set of reaction rate coefficients and/or soot mechanisms, as summarized in Table 4.3.

Table 4.3: Overview of soot model configurations (C1 – C6) used in the combustor model.

	$\mathbf{nuc_{fac}}$	$\mathbf{coag_{fac}}$	$\mathbf{sg_{fac}}$	$\mathbf{ox_{fac}}$	$\mathbf{ox_{num,fac}}$	**HACA**	**sg species**	$\boldsymbol{\eta_{OH}}$
C1	1.0×10^{-5}	49.5	0.25	0.30	0.50	-	C_2H_2 + PAH	0.13
C2	1.0×10^{-5}	47.3	0.23	0.28	0.50	-	C_2H_2 + PAH	0.13
C3	1.0×10^{-6}	49.5	0.45	0.30	0.50	-	C_2H_2	0.13
C4	2.9×10^{-6}	62.7	0.42	0.54	0.63	X	C_2H_2 + PAH	0.13
C5	3.1×10^{-6}	60.0	0.49	0.41	0.61	-	C_2H_2	0.13
C6	7.7×10^{-7}	3.90	0.18	0.18	0.74	-	C_2H_2 + PAH	0.20

These six configurations are selected in order to capture a range of soot mechanisms in literature, as described in Chapter 2, and to quantify the impact and behavior

of each step of the soot formation process. From Table 4.3, it is observed that the smallest scaling is applied to nucleation. This is explained by the assumption made in the soot models that soot directly forms from a sticking collision of two PAH species, resulting in number EIs of approximately 10^{19} to 10^{20} particles/kg_{fuel}. However, in reality, soot particles form after a series of collisions, which explains the correction factor needed.

The performance of the configurations against existing prediction methods and measurements for both EI mass and number is summarized in Figure 4-13. The existing prediction methods and measurements are described in detail in Appendix A.

Starting with EI soot mass, the models are observed to capture the trends in the validation data, with the exception of thrust settings below approximately 35%. Here, the model predicts zero soot emissions while measurements show nonzero EI values. For soot number EI, the models all capture the trend in the validation data of decreasing number EI with increasing thrust between approximately 60% and 100% thrust.

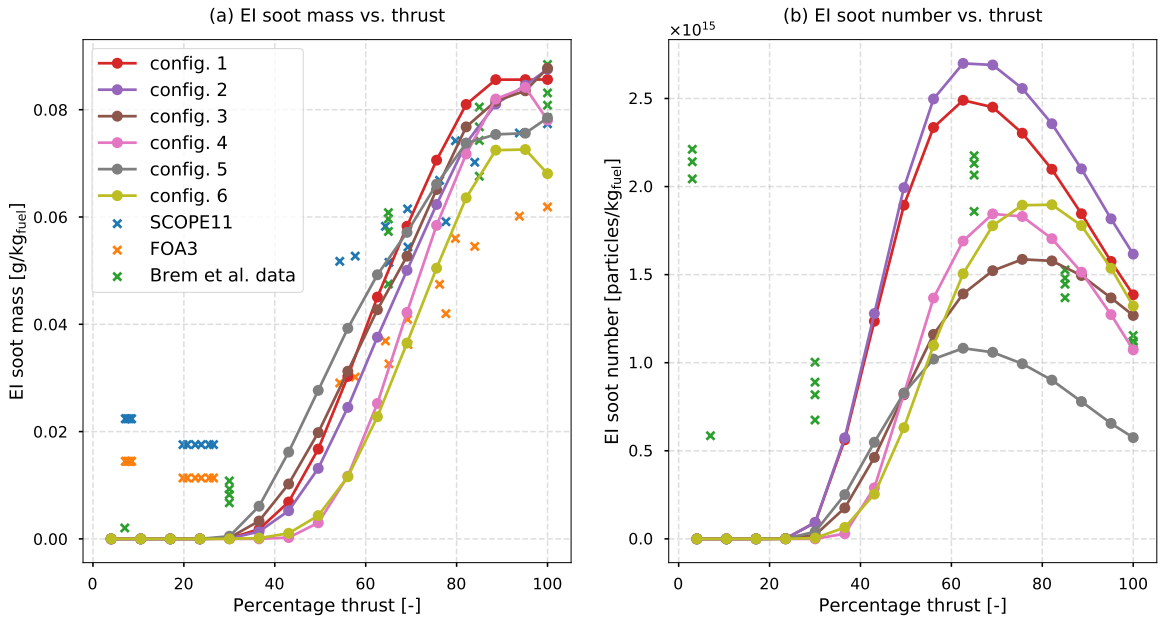

Figure 4-13: Comparison of EI soot (a) mass and (b) number with validation data (surrogate 4).

4.2.2 Primary Zone Analysis

Figure 4-14 shows the EI values for soot mass and number at the primary zone exit. The observed differences between the six configurations can be explained by comparing the different coefficients and soot mechanisms used.

Since soot formation mainly takes place in the primary zone and soot depletion primarily occurs in the secondary zone, the parameters related to nucleation, coagulation and surface growth have the largest impact in the primary zone.

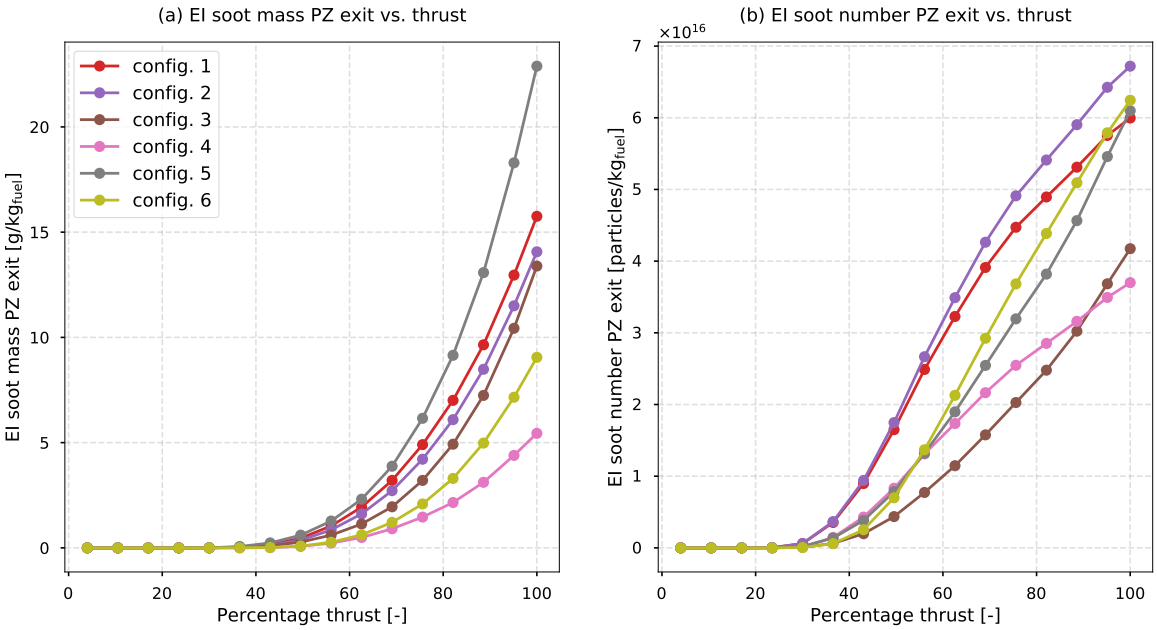

Figure 4-14: EI soot (a) mass and (b) number at primary zone exit (surrogate 4).

The values of EI soot mass at the end of the primary zone can be directly explained by the configuration parameters related to surface growth. For a given surface growth mechanism, a larger value of sg_{fac} leads to higher values of EI soot mass at the end of the primary zone. When distinguishing between surface growth with and without PAH species, it is observed that sg_{fac} is highest for surface growth solely through C_2H_2. This is the consequence of the rate having to be compensated for the absence of growth through PAH species. EI mass values are observed to be lowest for configuration 4, which uses surface growth through the HACA mechanism. This could be explained by a combined effect of the HACA mechanism limiting the available surface sites for growth, as well as the increased coagulation rate in configuration 4, limiting the

number of soot particles and thus the collision rate in surface growth through PAH species.

The observed differences in number emissions at the primary zone exit are explained by differences in nuc_{fac}, coag_{fac} and sg_{fac}. Higher nucleation factors, as well as lower coagulation and surface growth factors, increase the number of soot particles at the PZ exit.

The ratios of EI number at 100% thrust to 60% thrust are approximately twice as high for configurations 3 and 5 compared to configurations 1,2, and 4. Higher temperatures at 100% thrust compared to 60% thrust increase surface growth. For configurations 1,2 and 4 this increases competition for PAH species between surface growth and nucleation. This consequently leads to a relative reduction in EI soot number at 100% thrust compared to configurations without surface growth through PAH species. For configuration 6, which uses surface growth through PAH species, the ratio is approximately equal to those of 3 and 5. This is explained by the ≈15 times smaller coagulation factor. The coagulation rate depends on the soot number density squared and increasing the coagulation rate thus has a larger effect at higher thrust conditions.

Figure 4-15 shows EI soot mass per primary zone reactor i. Soot starts to form at $\phi \approx 1.8$. For the 30% and 7% thrust settings, the mass flow around this equivalence ratio is approximately zero (see Figure 4-3). This explains why the model predicts zero soot emissions at thrust settings below ≈35%. A peak in EI soot mass is observed at an equivalence ratio of ≈2.5. This peak could stem from a trade-off between temperature and concentration of PAH species, which increases with equivalence ratio. When Figure 4-15(a) is compared with 4-15(b), it is observed EI soot mass at ϕ=3 is ≈4 times higher for configuration 1 compared to configuration 3. This difference is explained by the increasing PAH surface growth rates with equivalence ratio caused by increasing PAH concentrations.

The effects of surface growth are also evident in the values of EI soot number per reactor, as shown in Figure 4-16. Here, two main observations are made. The first being the previously described different ratios of EI number at 100% thrust to

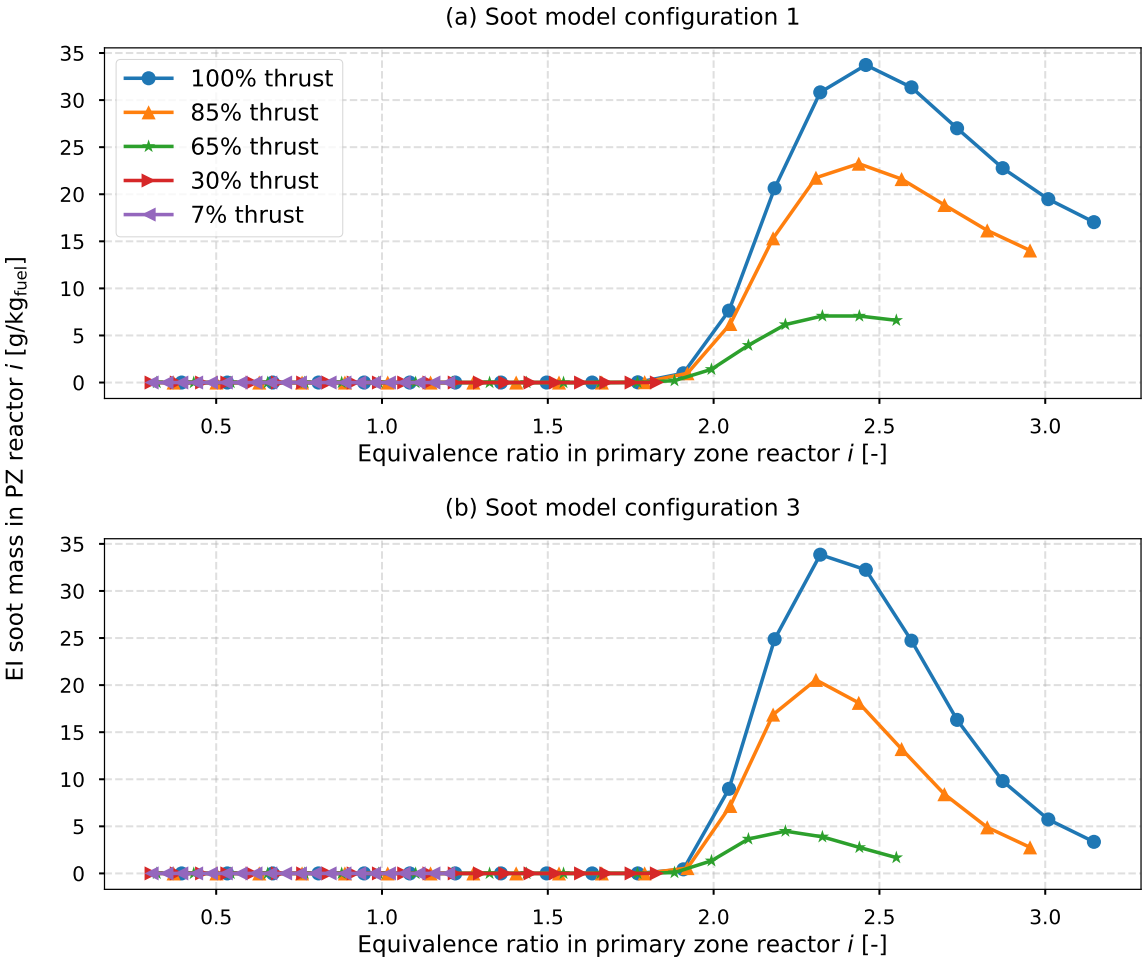

Figure 4-15: EI soot mass per reactor i for configurations (a) with and (b) without surface growth by PAH species (surrogate 4).

60% thrust, explained by consumption of PAH species for surface growth. Second, in Figure 4-16(a) the EI values are largest for 65% thrust. This is explained by lower temperatures and thus lower surface growth rates at lower thrust conditions (see Figure 4-15), resulting in higher available PAH concentrations for nucleation, which is less dependent on temperature.

4.2.3 Secondary Zone Analysis

Adding secondary and dilution air in the secondary zone leads to oxidation of soot, which is the dominant process in this part of the combustor. The soot oxidation rate depends on the temperature, soot surface area and the concentration of the oxidizing

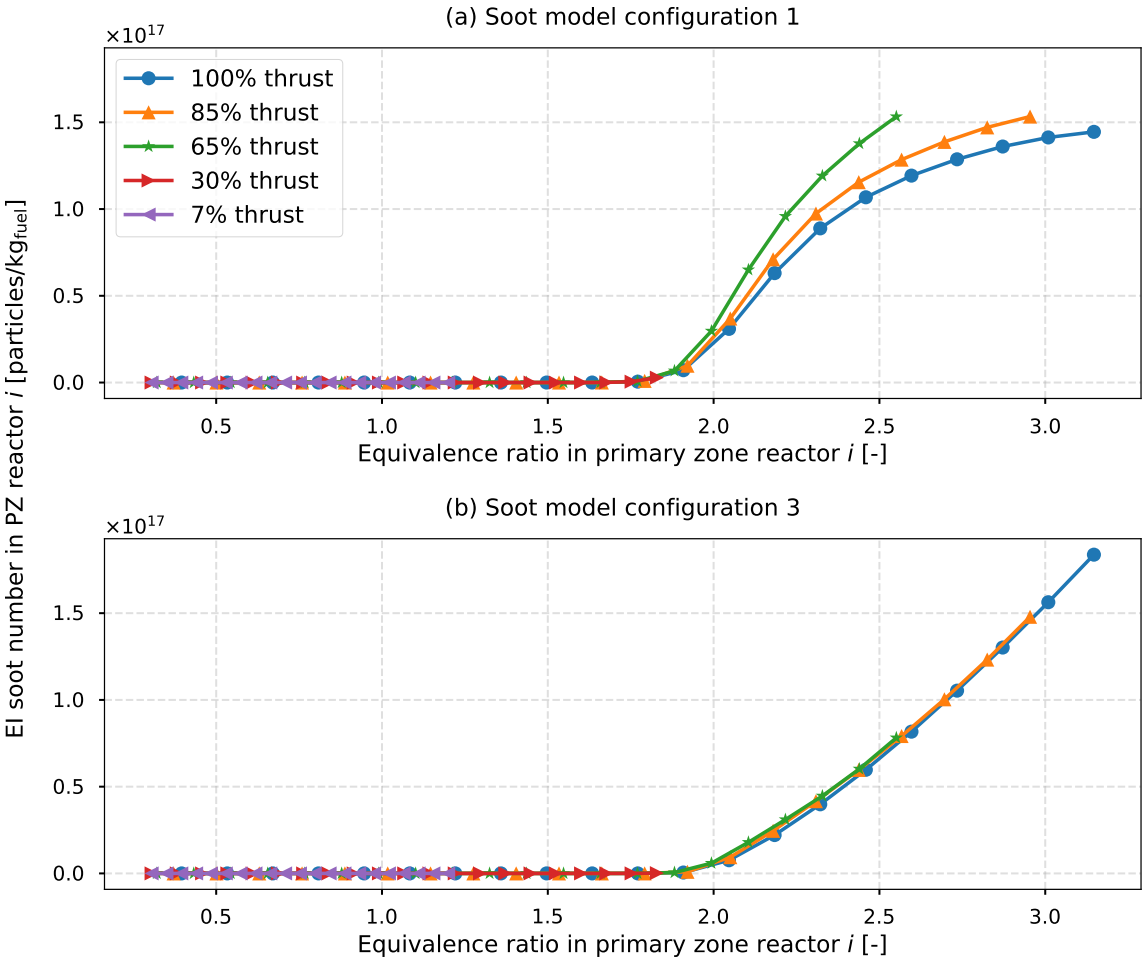

Figure 4-16: EI soot number per reactor i for configurations (a) with and (b) without surface growth by PAH species (surrogate 4).

species.

Figure 4-17 shows the development of EI soot mass and number throughout the SZ. As for CO, the majority of soot is formed in the PZ and destroyed in the SZ. More than 85% of the remaining soot mass and 80% of the remaining soot number come from the fast mixing region. For EI soot mass, a peak in the slow mixing region is visible. As this peak is caused by surface growth, it is not visible for the EI soot number. The soot oxidation reactions are observed to be quenched at the end of the SZ, which makes modeling (part of) the turbine unnecessary as values for EI soot will not change.

For a given model configuration and thrust level, implying fixed temperature and concentrations of oxidizing species, the main factor driving the EI soot mass at the

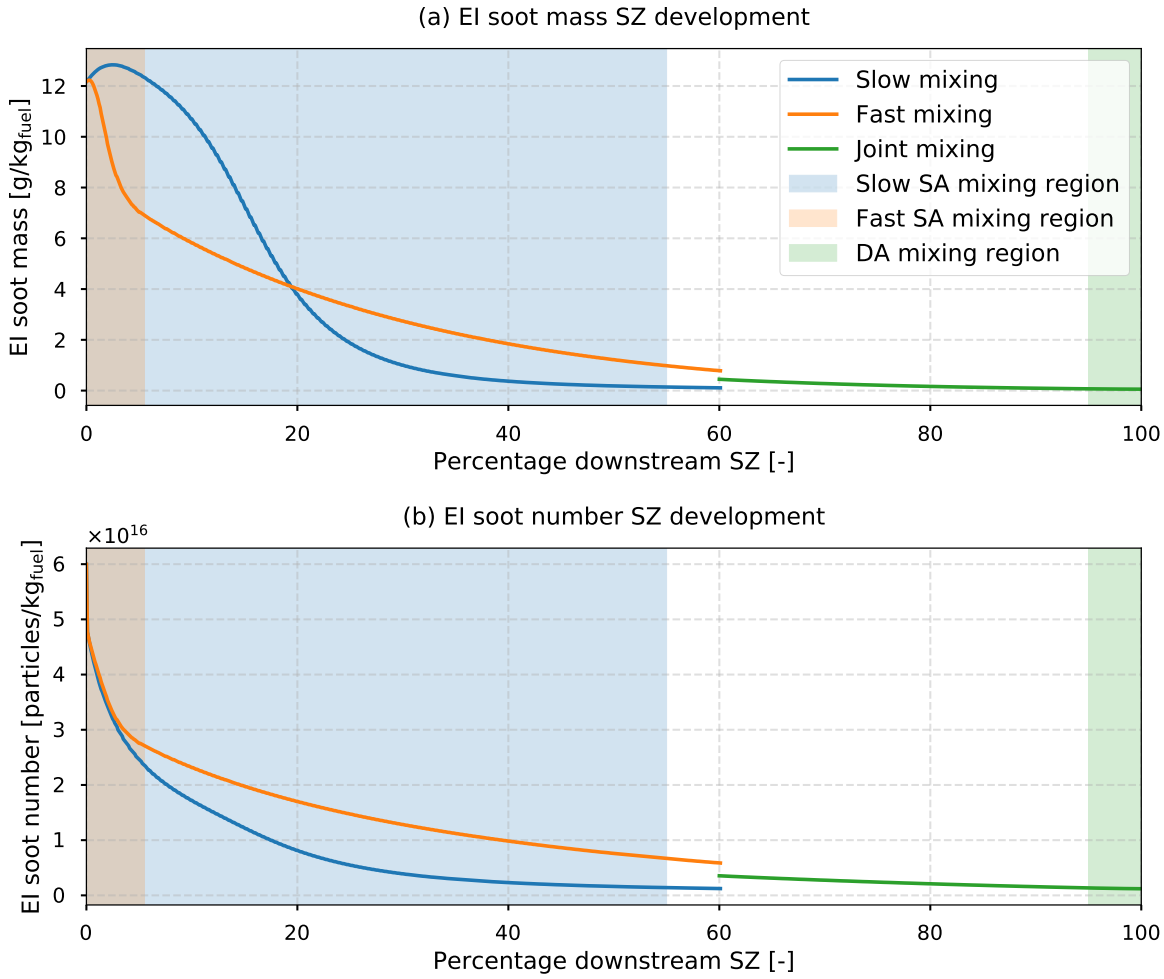

Figure 4-17: EI soot (a) mass and (b) number throughout the SZ for 100% thrust (configuration 3, surrogate 4).

combustor exit is the ratio between M and N (or the ratio between M and A_s) at the start of the secondary zone. A higher ratio of M over N implies a larger average particle size, or, framed differently, that for a given M, A_s — and thus the oxidation rate — is lower. A lower oxidation rate results in a higher EI soot mass.

4.3 Fuel Composition Effects

4.3.1 Comparison with Experimental Data

In order to validate the model predictions for soot in response to changing fuel compositions, a subset of the experiments conducted by Brem et al. [49] are simulated.

The predictions of each of the model configurations for two different fuels are evaluated. The total aromatics % v/v and naphthalene % v/v of these fuels are approximately equal to the values used in experiments by Brem et al. [49]. Tables 4.4 and 4.5 compare the values used in the experiments with those of the fuel surrogates in the model.

Table 4.4: Fuel volume percentage comparison: Jet A-1.

Thrust	**Brem et al. [49]**		**Model**	
	arom. % v/v	naph. % v/v	arom. % v/v	naph. %v/v
0%-100%	17.8	0.78	17.8	0.80

Table 4.5: Fuel volume percentage comparison: high aromatics fuel.

Thrust	**Brem et al. [49]**		**Model**	
	arom. % v/v	naph. % v/v	arom. % v/v	naph. %v/v
30 %	23.4	1.14	23.4	1.20
65 %	23.5	1.16	23.4	1.20
85 %	23.5	1.18	23.4	1.20
100 %	23.5	1.19	23.4	1.20

The resulting changes in EI soot mass and number are shown in Figure 4-18. The data is presented as the change in soot emissions when replacing the high aromatics fuel with Jet A-1. In Figures 4-18(a) and (b), it is observed that configurations 1, 2, 4 and 6 overpredict the percentage change in EI soot mass by 10 to 50 percentage points (p.p.) at 40% thrust and 40 p.p.–50 p.p. at 100% thrust. These discrepancies are explained by the surface growth species used in the soot model configurations. Configurations 1, 2, 4 and 6 all use surface growth through PAH species. A reduction in the concentration of PAH species, caused by a reduction in naphthalene content, or aromatic content in general, directly reduces the EI soot mass for these four configurations. On the other hand, configurations 3 and 5, which only use surface growth by C_2H_2, are less sensitive to the changes in PAH concentrations.

The model predictions for EI number are all within 20 p.p. of the experimental data, with the exception of configurations 4 and 6.

The predicted changes in EI soot mass using configurations 3 and 5 are shown in detail in Figures 4-18(c) and (d). The predicted values show maximum deviations of 5 p.p. with respect to experimental data for thrust settings up to ≈65%. At higher thrust settings, the gradient of the model predictions decreases and a maximum difference of ≈25 p.p. is observed at 100% thrust. This error is the consequence of an overprediction of the oxidation rate in the model.

The predicted values for the percentage change in EI soot number show maximum deviations of 8 p.p. compared to experimental data for thrust settings up to ≈85%. A maximum overprediction by 12 p.p. is observed at 100% thrust.

The results in Figure 4-18 indicate that surface growth through PAH species is overestimated in the model. This hypothesis is supported by findings in literature, which state that surface growth through PAH species is small or insignificant compared to C_2H_2 [96]. A possible explanation for the overprediction in PAH surface growth rates could be that the same value for sg_{fac} is used for both types of surface growth. However, the value for nuc_{fac}, which uses a similar sort of reaction rate as PAH surface growth, based on the collision frequency, is scaled by values ranging from 1.0×10^{-5} to 7.7×10^{-7}. Therefore, a separate value for sg_{fac} should be introduced for surface growth through PAH species.

4.3.2 Naphthalene Removal

The effects of naphthalene removal using extractive distillation and hydrotreating are quantified for each of the six soot model configurations and five jet fuel surrogates. Figure 4-19 shows the computed ranges of soot mass and number emissions reductions associated with the two naphthalene removal processes. These ranges represent both variations in soot model configurations as well as baseline fuel compositions. The naphthalene mole fraction in each of the baseline fuels is 0.02 and the mole fractions of aromatics range between 0.212 and 0.301.

Using the predictions by the configurations assuming only surface growth through

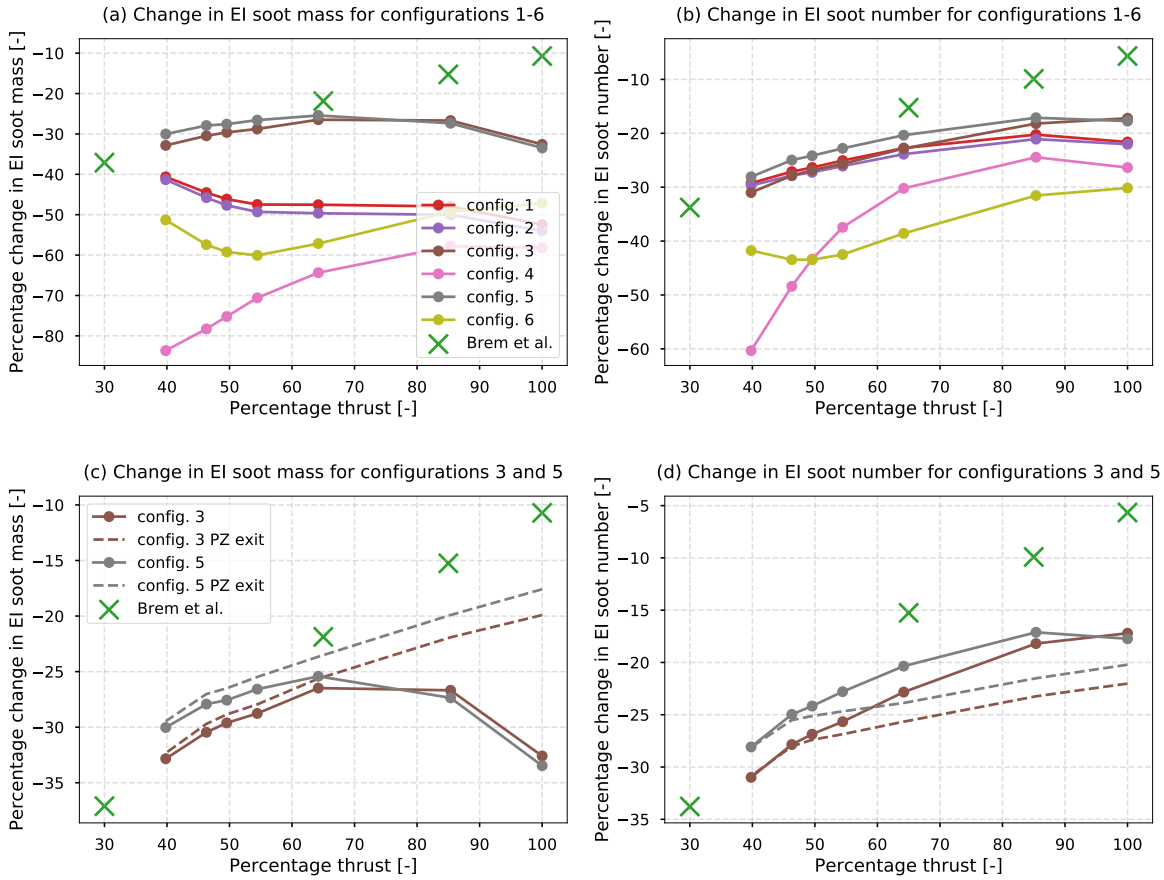

Figure 4-18: Comparison of model predictions with experimental data by Brem et al [49]. Percentage change in EI soot (a) mass and (b) number for all six configurations, as well as percentage change in EI soot (c) mass and (d) number for the configurations with only surface growth through C_2H_2.

acetylene, the mean reductions in EI mass are approximately 20 p.p. higher for extractive distillation than for hydrotreating. For EI soot number, the differences between the means of the two methods range from 11 p.p. at 100% thrust to 23 p.p. at 43% thrust. These differences are explained by tetralin being an aromatic species and having a relatively short pathway to becoming a PAH species. Reductions in mass are predicted to be larger than reductions in number, which is consistent with literature [49, 75]. Furthermore, especially for number emissions, reductions increase with decreasing thrust. This effect is also observed in experiments in literature [49, 50, 75, 130].

In order to explain why the change in soot emissions due to naphthalene removal increases with decreasing thrust, the primary zone is evaluated. Figure 4-20 compares

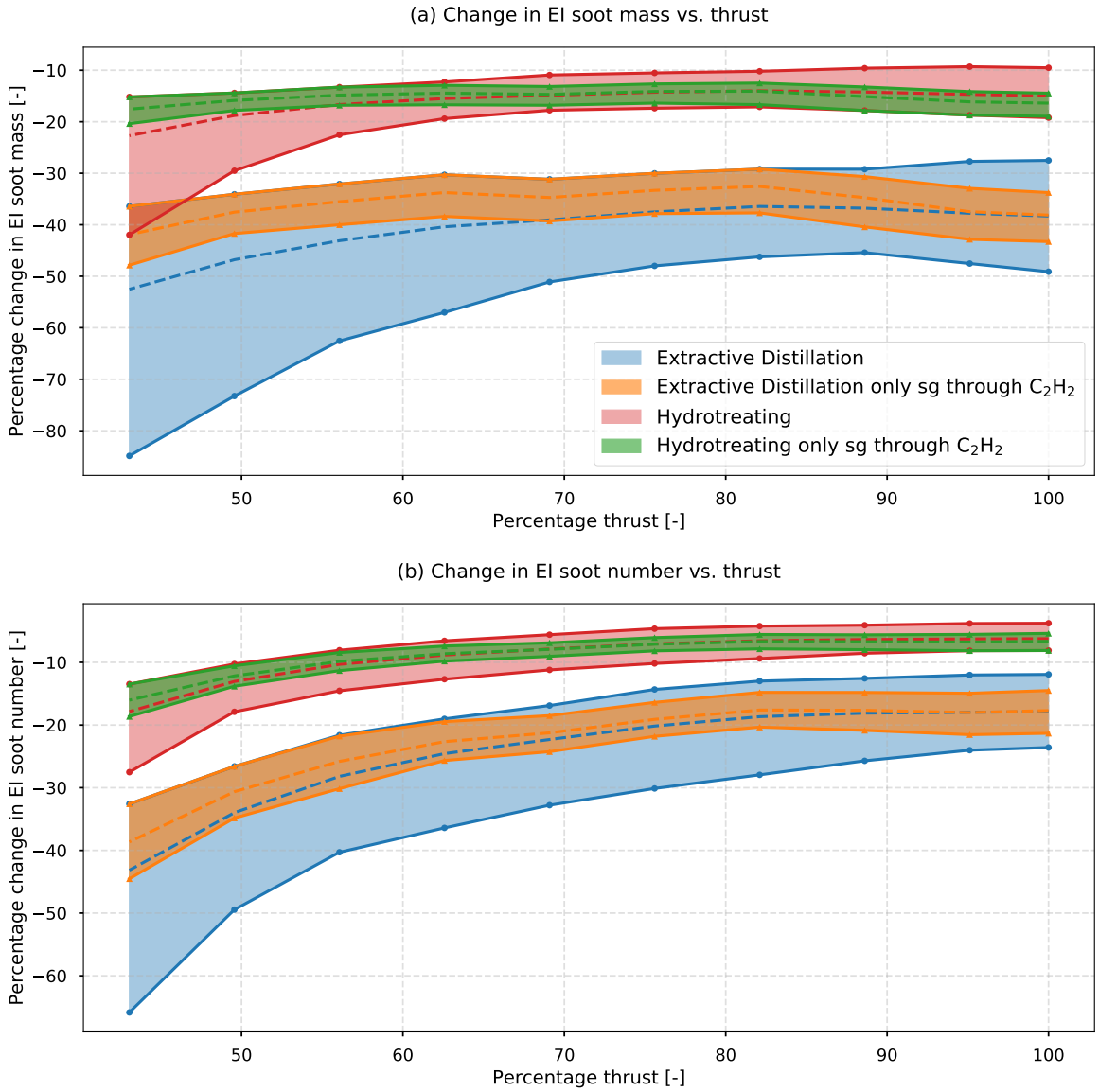

Figure 4-19: Ranges of predicted effects of naphthalene removal from jet fuel on EI soot (a) mass and (b) number. The dashed lines represent the means of the prediction ranges.

the PZ behavior of configurations 1 and 3 for fuel with and without naphthalene (extractive distillation) at 62% and 100% thrust. Two main factors explain the change in sensitivity to naphthalene content with thrust setting. The first one is that all of the soot at 62% thrust is formed at $\phi < 2.6$ whereas at 100% thrust approximately 25% of soot mass is formed at $\phi > 2.6$. Lower equivalence ratios are more sensitive to naphthalene concentration due to their lower fuel flows and therefore lower PAH concentrations. The increasing reduction with decreasing equivalence ratio is visible

in Figures 4-20(c) and (d), where the change in EI soot mass is approximately 1.5 times higher at ϕ=2.2 compared to ϕ=3.0. The factor difference in EI soot number reductions between ϕ=2.2 and ϕ=3.0 ranges from ≈2 for configuration 3 to ≈10 for configuration 1.

Whereas the first factor is related to the increasing sensitivity to fuel composition with decreasing ϕ in reactor i, the second factor concerns the difference in percentage change between the two thrust settings for a given ϕ. As visible in Figure 4-20(c) and (d), the red and orange lines, representing the changes in soot emissions at 62% thrust, are below the green and blue lines, which represent the changes in soot emissions at 100% thrust. This is explained by the temperature difference between the two thrust conditions. Higher temperatures at 100% thrust make the reactor more resilient to changes in naphthalene concentrations.

When configurations 1 and 3 are compared in Figure 4-20(c), a larger decrease in EI soot mass for configuration 1 than for configuration 3 is observed. This is caused by part of the soot mass coming directly from PAH species in configuration 1. The difference in the blue and green lines in Figure 4-20(d), representing the changes in soot number emissions at 100% thrust, is caused by the higher nucleation rate in configuration 1, making EI soot number less sensitive to changes in PAH concentrations.

Figure 4-21 compares the predicted changes at the end of the PZ and SZ for the case of extractive distillation. Two main effects are observed. First, for the change in EI soot mass — and to a lesser extent EI soot number — the (mean) predictions at the end of the PZ and SZ diverge above approximately 65% thrust. The second observation is that the predicted changes in EI soot and their ranges increase when going from the PZ to the SZ. Both could be explained by a disproportionate increase in oxidation rates above approximately 65% thrust, which occurs in the SZ and is therefore not visible in the PZ values. This increase in oxidation rates could be the result of a decreasing average particle size in the case of naphthalene removal. As explained in Section 4.2.3, a smaller average particle size leads to lower soot mass emissions due to a decrease in M/A_s.

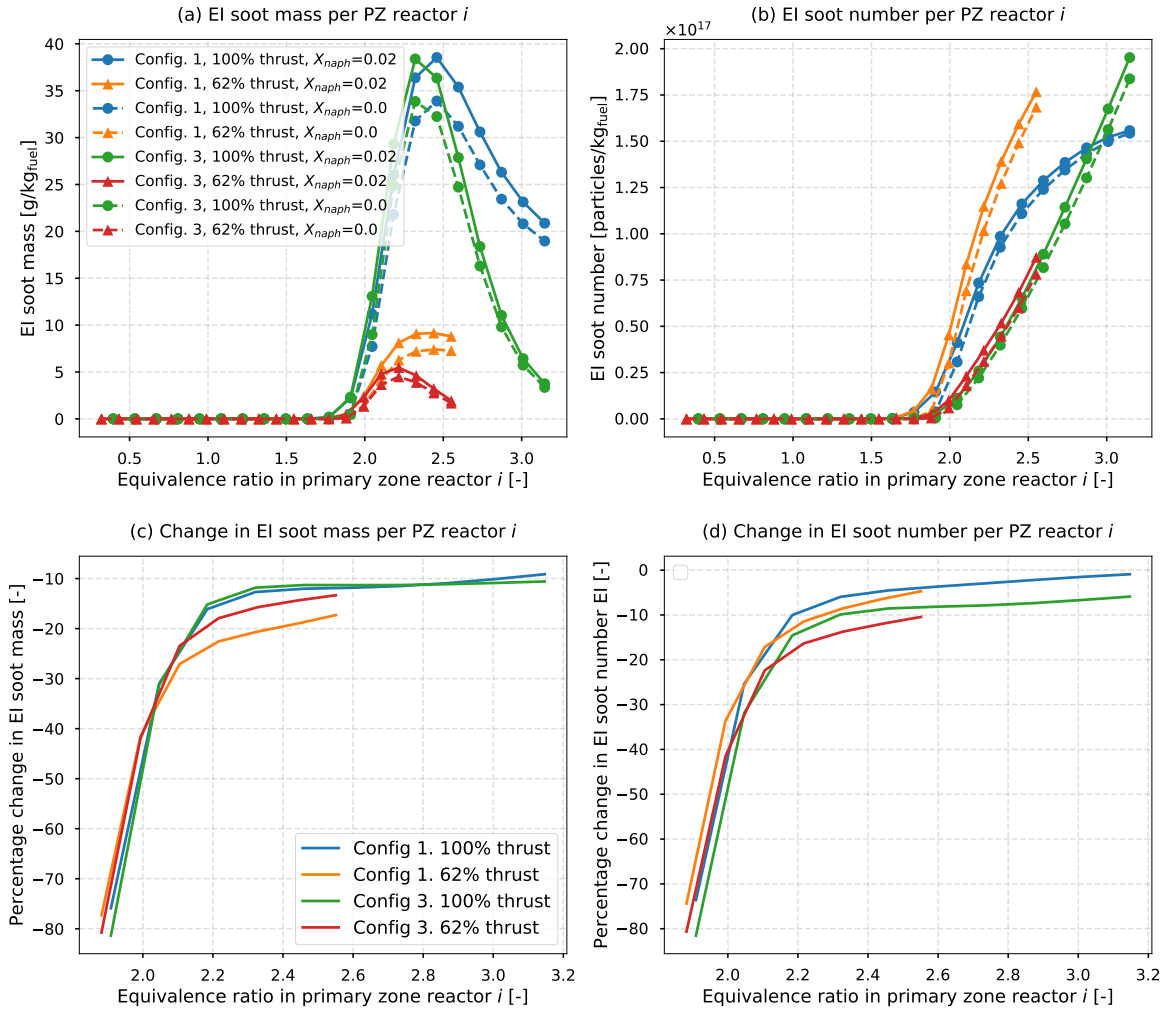

Figure 4-20: Overview of primary zone predictions in response to naphthalene removal (extractive distillation) for configurations 1 and 3. Both predictions of EI soot (a) mass and (b) number per reactor i are shown, as well as the reactor-specific relative change in EI soot (c) mass and (d) number due to naphthalene removal.

4.3.3 Biofuels

Figure 4-22 shows the predicted effects of using 50:50 biofuel blends on NO_x and CO emissions. For NO_x, reductions in EI between approximately 4.5% and 6.5% are observed at thrust settings above 40%. As EI CO values above approximately 40% thrust are below 1 g/kg$_{fuel}$, the observed absolute changes for these thrust conditions are below 0.05 g/kg$_{fuel}$. For thrust settings lower than 40%, where CO EI values are larger than 1 g/kg$_{fuel}$, reductions between approximately 1.5% and 3.0% are observed. The differences between the surrogates are caused by differences in the aromatic

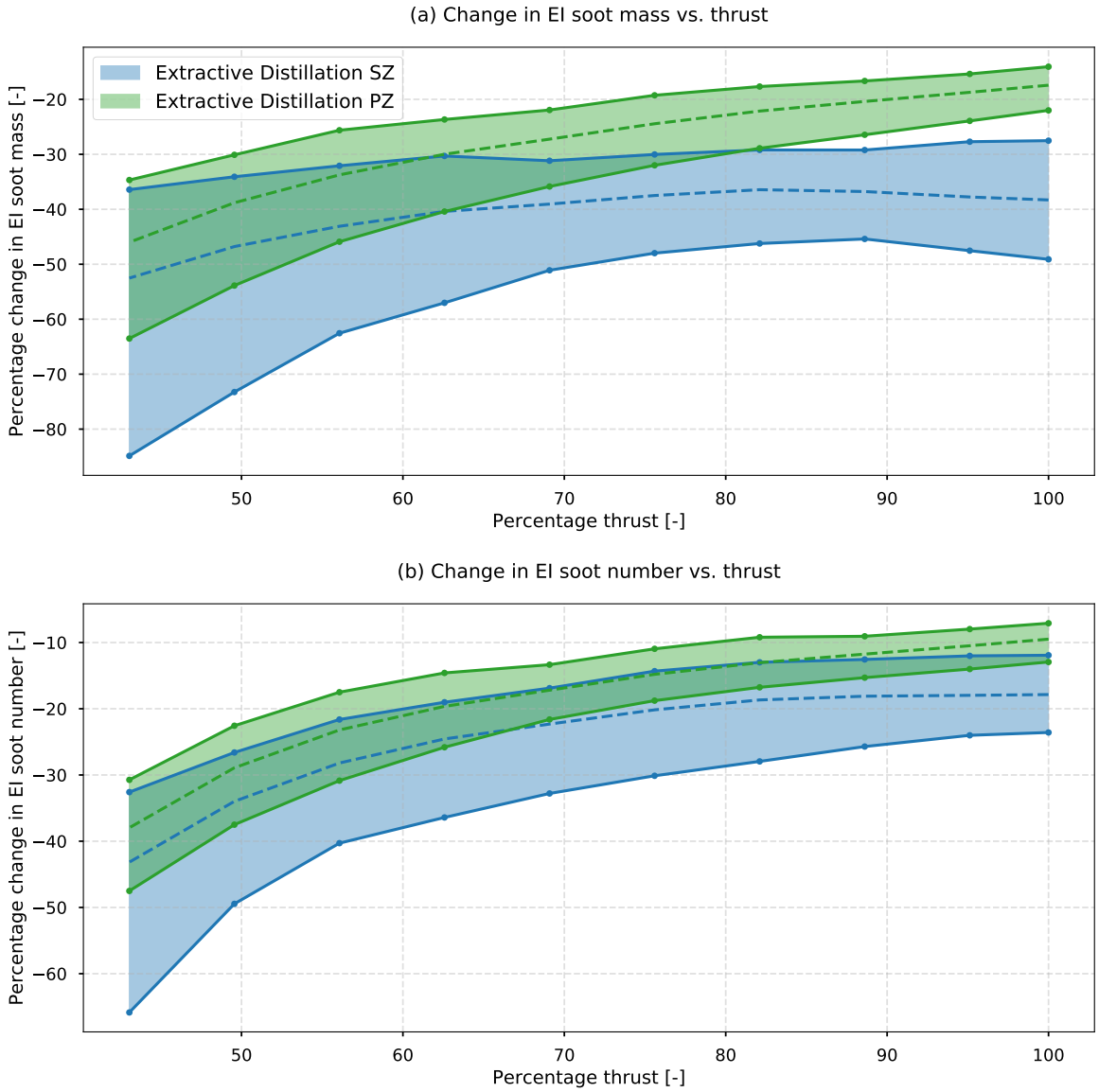

Figure 4-21: Comparison of predicted changes in EI soot (a) mass and (b) number due to extractive distillation at the PZ and SZ exit. The dashed lines represent the means of the prediction ranges.

content in the fuel surrogates. For example, surrogate 2 contains a mole fraction of aromatics of 0.212 compared to 0.301 for surrogate 1. This leads to a larger absolute difference in aromatics mole fraction between the base surrogate and its 50:50 blend for surrogate 1 compared to surrogate 2. A larger change in aromatics fraction is associated with a larger reduction in combustor peak temperatures and therefore in NO_x formation. This indicates that using 50:50 blends for baseline jet fuels having higher aromatic content results in a larger relative decrease in NO_x emissions.

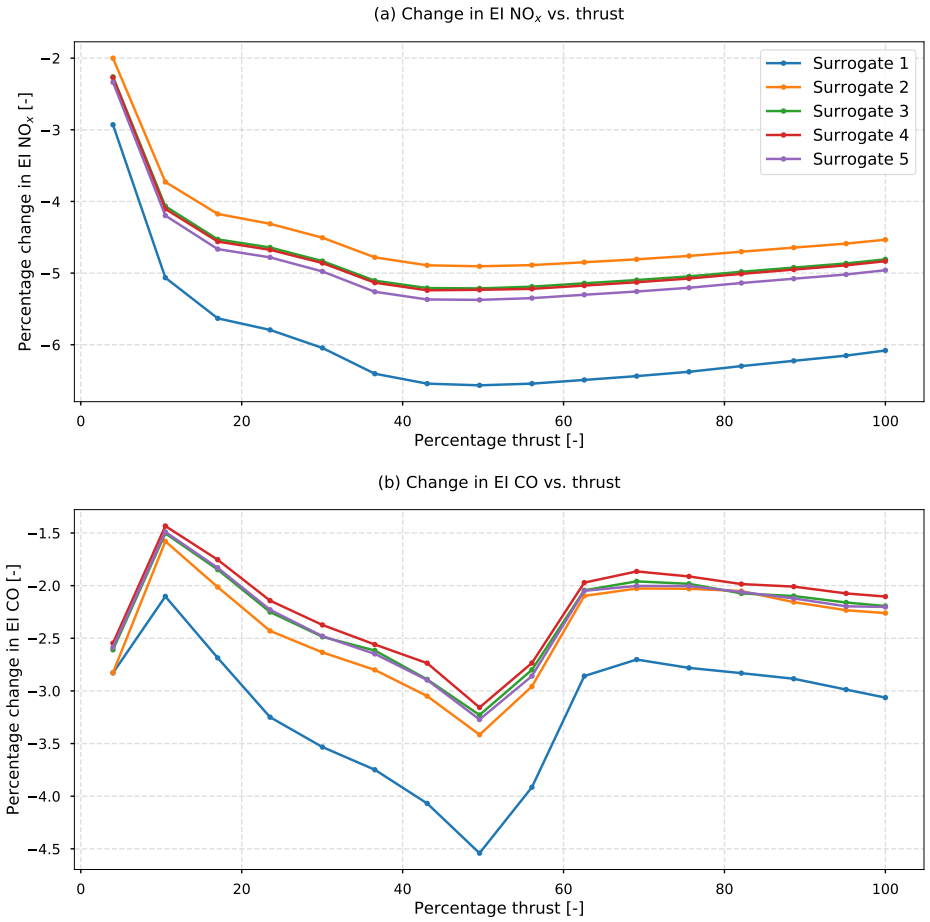

Figure 4-22: Effects of using 50:50 biofuel blends on (a) NO_x and (b) CO emissions for the five surrogates.

Figure 4-23 shows the predicted effects of using biofuels on soot mass and number emissions for the six different soot model configurations and five different surrogates. The predicted values for the selected configurations (only C_2H_2 surface growth) fall within the ranges in literature based on measured values [50, 51, 53, 75, 131, 132].

4.4 Cruise

The model is also used to predict NO_x and CO emissions at cruise. Updated input conditions corresponding to a cruise altitude of 35,000 ft are generated with the engine model. Furthermore, the oxidizer composition in the combustor model is updated for zero humidity, which approximates the humidity at 35,000 ft [54].

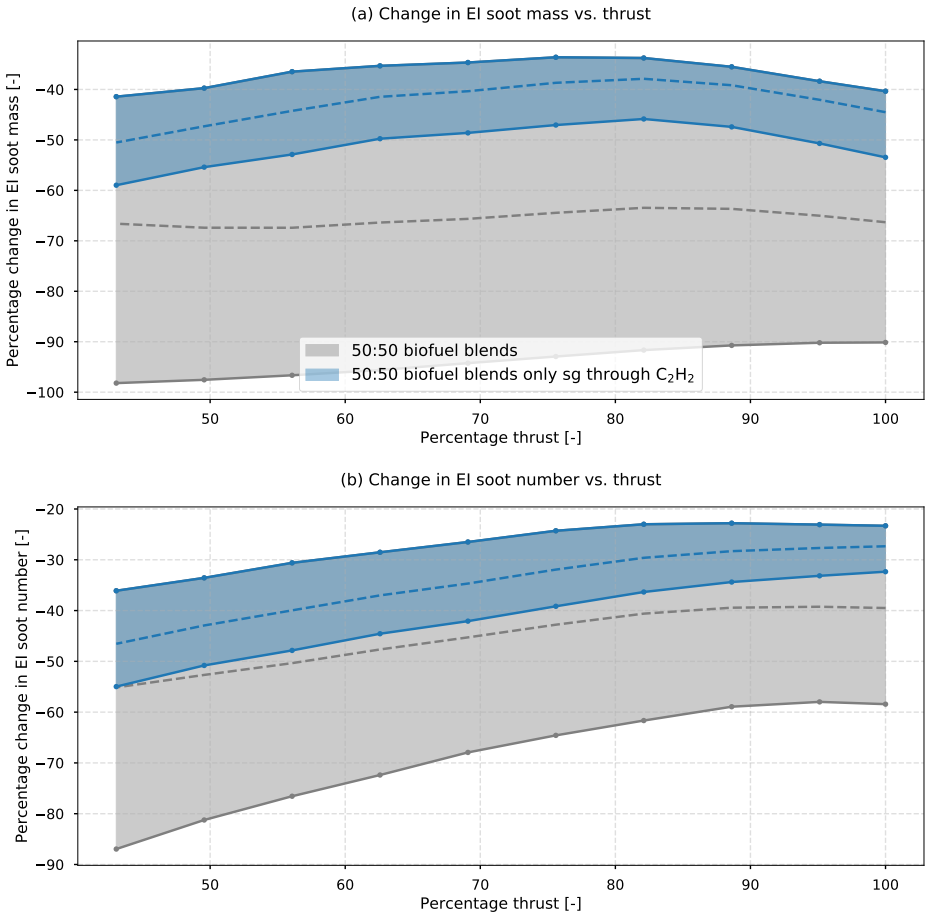

Figure 4-23: Ranges of predicted effects of using 50:50 biofuel blends on EI soot (a) mass and (b) number. The dashed lines represent the means of the prediction ranges.

Figure 4-24 compares the resulting model predictions with the predictions using the estimation methods described in detail in Appendix A. The model predictions for NO_x lie within 5% of the predictions from the P3T3 method and the BFFM2. As CO emissions above 40% thrust have not been considered in the model parameter calibration process, there is a mean 30% difference (MAE of 0.07) between the EI CO values predicted by the model and the values in the EDB data. As these values are scaled to cruise conditions in the P3T3 method and BFFM2, differences between the predictions for CO up to a factor of five are visible in Figure 4-24. However, when correcting for the different CO predictions at sea level by using the model predictions (model inputs) at sea level in the P3T3 method, the three highest fuel flow points are within 30% of the model predictions with a MAE of 0.09. For the lowest fuel flow

point, an error of 27% is observed.

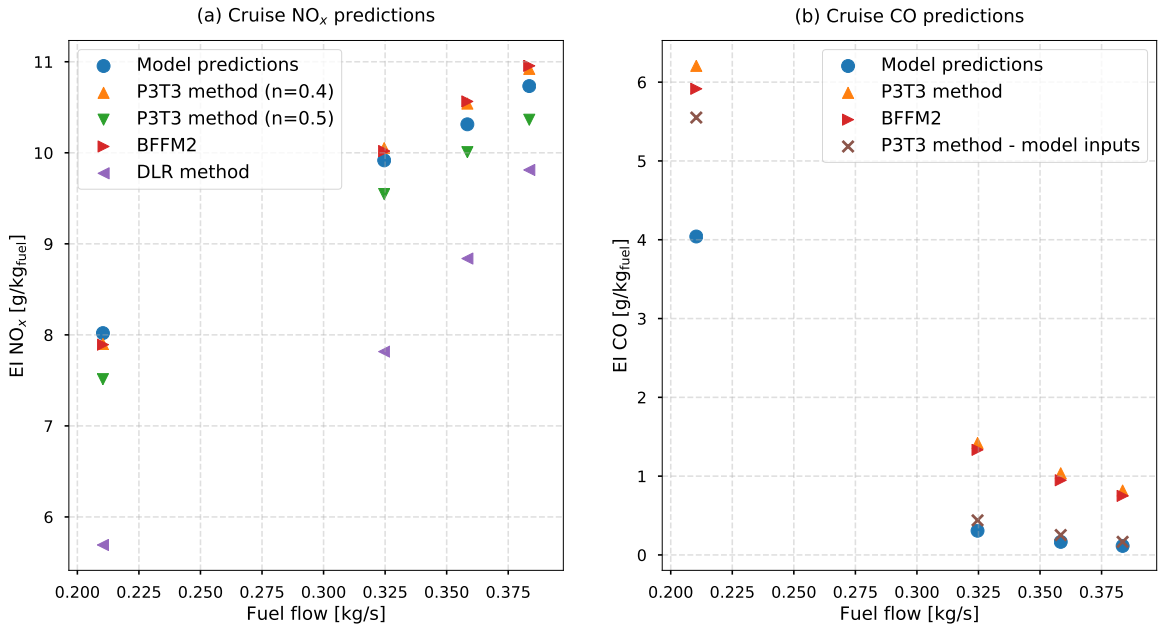

Figure 4-24: Comparison of model cruise predictions for (a) NO_x and (b) CO with the P3T3 method, BFFM2 and DLR method.

Part of validating the response of the model to changes in ambient conditions is to quantify the predicted humidity effects on NO_x emissions. Even though this was already incorporated in comparing the cruise predictions, the humidity effect is quantified separately as well. Figure 4-25 shows the response of the model when decreasing the humidity h from 0.00634 kg_{H_2O}/kg_{dryair} (sea level) to zero. The model response is compared to two methods in literature which estimate the effect of humidity on NO_x emissions. The first method (literature humidity correction 1) is the humidity correction used in ICAO Annex 16: Environmental Protection, Volume II [133]. It is given by

$$EI_{NO_x,2} = EI_{NO_x,1} \exp\left[19(h_1 - h_2)\right], \tag{4.1}$$

where the factor 19 [-] was originally determined by Marchionna et al. [134] through experiments for an advanced annular combustor designed by Pratt & Whitney [135]. Later experiments for 30 engines resulted in a mean estimate of this factor of 18.68, with a range of 12.01 to 24.35 [136].

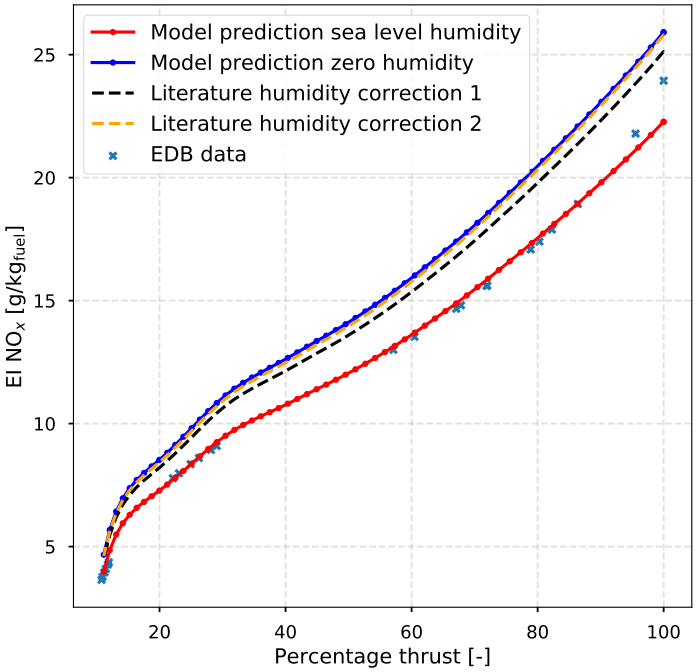

Figure 4-25: Comparison of the humidity effect on NO_x emissions predicted by the model with two NO_x humidity corrections in literature.

The second method (literature humidity correction 2) is a method proposed by Moore [137], which suggests a 25% increase in NO_x emissions per 0.01 kg_{H_2O}/kg_{dryair} decrease in humidity.

The model predictions match literature humidity correction 2 within 1% and deviate approximately 5% from literature humidity correction 1.

Chapter 5

Conclusions

5.1 Using Pycaso to Predict NO_x, CO and Soot Emissions

The main contribution of this thesis is summarized as the development of a gas turbine combustor model (Pycaso) with which the effects of using biofuels on NO_x, CO and soot emissions, as well as the effect of naphthalene removal on soot emissions, have been quantified. The model has also demonstrated its capability of predicting cruise emissions and has contributed to further understanding the relative importance of different formation and depletion processes of NO_x, CO and soot.

5.1.1 NO_x and CO Emissions

This thesis shows that a combustor model using a combination of WSR and PFR can match NO_x measurements of a CFM56-7B engine at sea level within 9% for all thrust settings (RMSE of 0.41). For CO emissions, the model matches measurements within 12% for thrust settings below 25% and shows an average relative error of 32% for thrust settings above 25% (RMSE of 1.0). Local differences in mixing of fuel and air in the primary zone are accounted for by modeling multiple reactors at different equivalence ratios. It is suggested to make a distinction between fast and slow mixing rates in the PFR. The mixing volumes (and thus times) in which the gas mixture

mixes with secondary air in the PFR are shown to be the most important factor in determining emissions, as most of the NO_x formation and CO depletion occurs here.

The model also provides an explanation for the behavior of the measured EI NO_x and EI CO values in the EDB. For NO_x, the decrease in gradient around 30% thrust (approach) is suggested to be the result of shifting from a rich to a lean average primary zone. The sensitivity to thrust at thrust settings below 15% is caused by "cold" unburned fuel entering the secondary zone, decreasing combustor peak temperatures.

The model predicts NO_x reductions of 4%–7% from using 50:50 biofuel blends, depending on the specific blend. Reductions in CO emissions are predicted to lie between 2%–4%. As the model has also been shown to match existing methods for cruise emissions within 5% for NO_x and 30% for CO, the model captures the effect of changing ambient conditions (P_3, T_3 and humidity).

5.1.2 Soot Emissions

Six different soot model configurations, with each using a fixed set of coefficients, have been developed. The coefficients suggest that nucleation, surface growth and oxidation rates in literature have to be scaled down to be used in gas turbine combustors, whereas the coagulation rate is scaled up. For nucleation, factors smaller than 1×10^{-5} are required, indicating that the unscaled rate leads to a significant overprediction in incipient soot particles.

The sensitivities to fuel composition predicted by the two configurations only using surface growth through C_2H_2 show a maximum deviation of 5 p.p. for soot mass and 10 p.p. for soot number compared to experimental values, with the exception of thrust settings above 65% for soot mass and above 90% for soot number. Here, maximum differences with measurements of approximately 25 p.p. and 15 p.p., respectively, are observed. From a comparison with experimental data, it is suggested that the PAH surface growth rate is overestimated. This results in an overprediction of sensitivities of soot emissions to fuel composition for the four configurations that model surface growth through PAH species.

Figure 5-1 summarizes the predicted effects of naphthalene removal through both extractive distillation and hydrotreating, as well as the effects of using five different 50:50 biofuel blends.

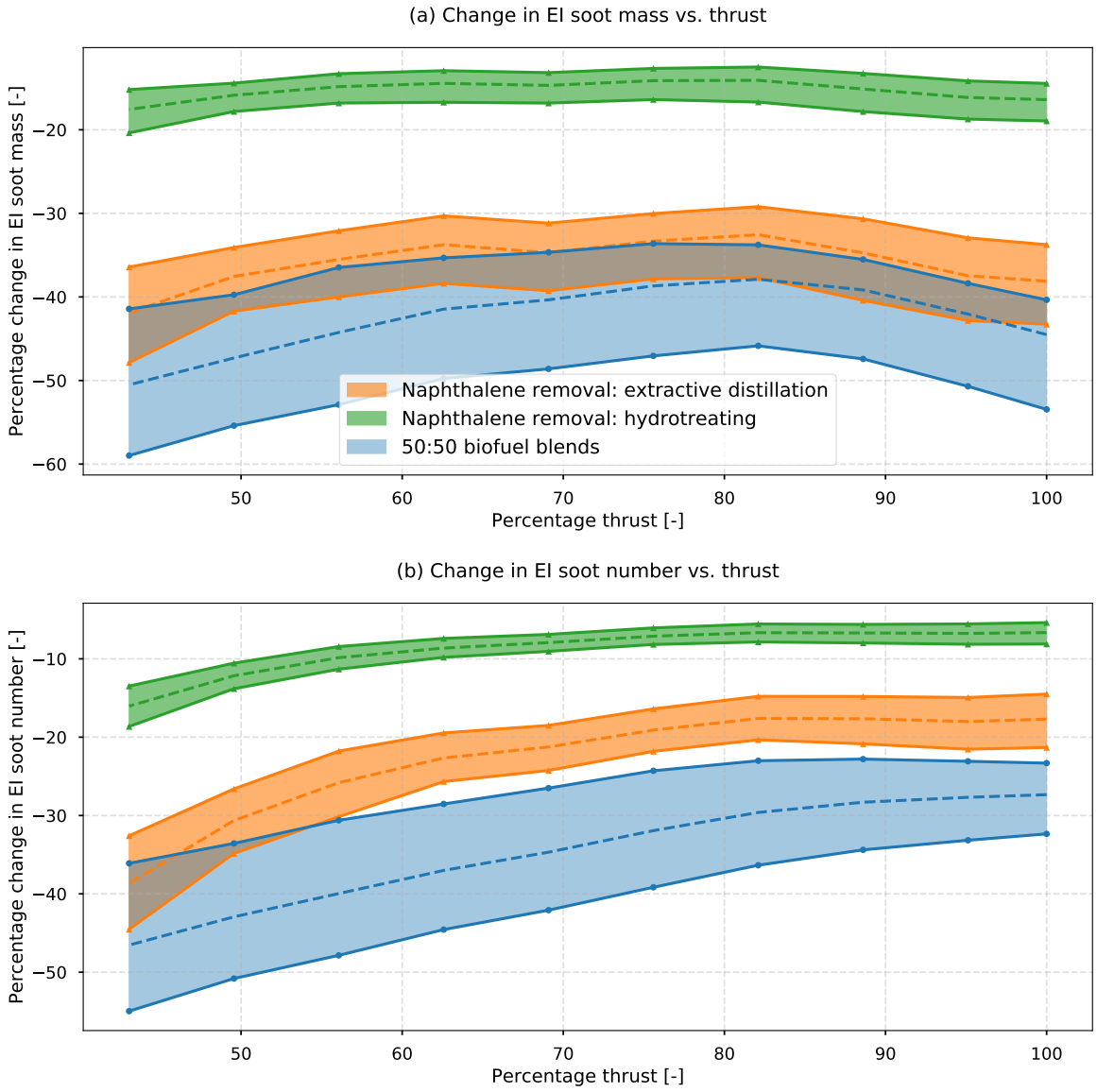

Figure 5-1: Overview of the predicted effects of naphthalene removal and the use of 50:50 biofuel blends on EI soot (a) mass and (b) number for the two soot model configurations only modeling surface growth through C_2H_2. The shaded regions represent the prediction range.

For naphthalene removal through hydrotreating, the model suggests mean reductions ranging from 16% [15%–19%] in mass and 7% [5%–8%] in number at 100% thrust to reductions of 18% [15%–20%] in mass and 16% [14%–19%] in number at

43% thrust (the minimum thrust modeled here). For extractive distillation, reductions of 38% [34%–43%] in mass and 18% [15%–21%] in number at 100% thrust and reductions of 42% [36%–48%] in mass and 39% [33%–45%] in number at 43% thrust are estimated. Lastly, the five different biofuel blends result in reductions ranging from 45% [40%–54%] in mass and 27% [23%–32%] in number at 100% thrust to reductions of 51% [41%–59%] in mass and 47% [36%–55%] in number at 43% thrust. The range captures variations in compositions of the baseline jet fuel and soot model configurations.

5.2 Future Work

5.2.1 NO_x and CO Emissions

Two main improvements relating to NO_x and CO emissions are proposed. First, more weight could be given to matching CO emissions at thrust settings above 40%. Even though emission indices here are generally below 1 g/kg_{fuel}, predicting emission indices at these thrust settings becomes important to predict cruise emissions. Next, this work suggests that NO_x and CO formation are primarily impacted by their mixing volume (or mixing time) and mixing temperature. Therefore, it may be possible to fix the secondary zone equivalence ratio at 0.6–0.8 and not include it in the calibration parameters. The reason for this is that the equivalence ratio determines the amount of secondary air, and therefore the rate at which the temperature decreases. If this rate is higher, the mixing temperature is lower and vice versa. Varying the lengths over which the secondary air is inserted may be enough to control the mixing times and temperatures.

The focus of this thesis has primarily been on using the combustor model for the CFM56-7B engine. In future work, the model will be applied to other aircraft engines. This will firstly be done for engines also containing an RQL combustor. However, the opportunity of changing the model architecture to represent other combustor types also exists.

Another opportunity is to combine the model's capability of predicting cruise emissions with its predictions of change in emissions due to fuel composition. In that way, an estimate of the effect of using various fuel compositions on cruise NO_x and CO emissions could be made. This is especially relevant for NO_x as the majority of its impacts stem from emissions during cruise.

5.2.2 Soot Emissions

Two major improvements to the soot model can be made. First, the prediction capability of the model could be expanded to thrust settings below approximately 35%. Second, further analysis into the behavior of soot mass emissions in response to changing fuel compositions, especially at thrust settings above roughly 65%, could be performed.

Specific improvements related to modeling each of the four steps of soot formation are also identified. For nucleation, more detailed nucleation mechanisms could be implemented. This could decrease the scaling ($<1 \times 10^{-5}$) required in the current model. For surface growth, the mechanism for growth through PAH condensation could be revisited as it has been shown that reaction rates are too high in the current model. Another improvement, related to coagulation, would be to assess the potential of replacing the effect of oxidation on the number of particles by an increased coagulation rate. Lastly, for oxidation, a further analysis into the effect of using different values for the collision efficiency for oxidation by OH could be performed.

An unexplored opportunity of the model is to use it to predict soot emissions at cruise. It is thought that the majority of soot impacts occur due to emissions at cruise altitudes. However, little is known about cruise soot emissions.

Appendix A

Data and Models

In order to evaluate the model for both sea level and cruise emissions, a combination of data and models is used. For NO_x and CO emissions, data from the EDB is used to validate LTO emissions, whereas the P3T3 method, BFFM2 and DLR method are used for cruise validation. Predicted soot emissions are compared to a mixture of data and model values. Furthermore, experimental data relating changes in soot emissions to fuel composition is used to test the models' predictive capability of fuel composition effects.

A.1 NO_x and CO

LTO data for NO_x and CO emissions is available for the CFM56-7B engine in the EDB. This data is used to assess the model's predictive capability at sea level. However, extensive and accurate data for cruise is not available and therefore models are used to predict cruise emissions [54].

The models used for NO_x and CO emissions at cruise are the P3T3 method, BFFM2 and the DLR method. The latter two methods relate in-flight emission indices to emission indices at reference sea level conditions by correcting the in-flight fuel flow to a sea level equivalent [58]. The predicted values using fuel flow methods have been observed to be within 10%–15% from predicted values from the P3T3 method for NO_x, whereas CO predictions might be up to a factor of two different

depending on the engine type and thrust level [57, 58].

In this thesis, both the P3T3 and fuel flow methods are used as comparison with the model predictions at cruise. Since engine data is available from the engine model, all required input conditions for both types of methods are known.

A.1.1 P3T3 Method

The working assumption behind the P3T3 method is that emissions at conditions different than at ISA conditions can be calculated (and vice versa) by correcting data at ISA conditions for the differences in P_3, T_3, FAR and humidity [57].

First, T_3 at the flight condition of interest ("Alt") is used to calculate reference values for EI, P_3 and FAR at sea level standard conditions. After obtaining the reference values, the EIs at the conditions of interest (cruise in this case) are calculated using [57]

$$\mathrm{EI}_{\mathrm{NO}_x,\mathrm{Alt}} = \mathrm{EI}_{\mathrm{NO}_x,\mathrm{SL}} \left(\frac{P_{3,\mathrm{Alt}}}{P_{3,\mathrm{SL}}}\right)^n \left(\frac{\mathrm{FAR}_{\mathrm{Alt}}}{\mathrm{FAR}_{\mathrm{SL}}}\right)^m \exp\left[19(h_{\mathrm{SL}} - h_{\mathrm{Alt}})\right], \tag{A.1}$$

and

$$\mathrm{EI}_{\mathrm{CO},\mathrm{Alt}} = \mathrm{EI}_{\mathrm{CO},\mathrm{SL}} \left(\frac{P_{3,\mathrm{SL}}}{P_{3,\mathrm{Alt}}}\right)^p \left(\frac{\mathrm{FAR}_{\mathrm{SL}}}{\mathrm{FAR}_{\mathrm{Alt}}}\right)^m. \tag{A.2}$$

where coefficients n, m and p are dependent on the specific engine-combustor combination. Experiments have suggested values of 0.2–0.5 for n, with a value of 0.5 suggested by theory [57]. However, a value of 0.4 is supported by experimental data and is the value as agreed through CAEP [15, 54, 57]. The values of m and p are set to 0 and 1.0 respectively [54, 57]. For NO_x, a humidity correction is applied, expressed by the exponential term in Equation A.1. Here, h_{SL} and h_{Alt} represent the humidity ratio of air at sea level and at in-flight conditions respectively [$\mathrm{kg}_{\mathrm{H_2O}}/\mathrm{kg}_{\mathrm{dryair}}$]. This correction is applied since adding water to the air in the engine reduces the peak flame temperature inside the aircraft combustor and thus reduces NO_x formation [57]. The

factor 19 was originally determined by Marchionna et al. [134] through experiments for an advanced annular combustor designed by Pratt & Whitney [135]. Later experiments for 30 engines resulted in a mean value of 18.68, with values ranging from 12.01 to 24.35.

A.1.2 BFFM2

Since data on P_3 and T_3 is assumed not to be available in fuel flow methods, the fuel flow is used to relate reference conditions to in-flight conditions. The fuel flow during flight must be converted to the sea level value corresponding to the same T_3 as the T_3 at flight level conditions (similar to P3T3 method). A fuel flow correlation factor is introduced, which is multiplied with the fuel flow at altitude to result in the equivalent fuel flow at reference conditions [57]. DuBois and Paynter [57] showed that the fuel flow at reference conditions must be approximately $\frac{(\theta_{\text{amb}})^{3.8}}{\delta_{\text{amb}}} \exp(0.2M^2)$ times higher than the fuel flow at altitude in order to get to the same T_3. The mass flow at altitude and sea level are consequently related via

$$\dot{m}_{\text{fuel,SL}} = \dot{m}_{\text{fuel,Alt}} \frac{\theta_{\text{amb}}^{3.8}}{\delta_{\text{amb}}} \exp(0.2M^2), \tag{A.3}$$

where M is the Mach number and θ_{amb} and δ_{amb} are defined as [58]

$$\theta_{\text{amb}} = \frac{T_{\text{amb}}[\text{K}]}{288.15}, \tag{A.4}$$

and

$$\delta_{\text{amb}} = \frac{P_{\text{amb}}[\text{Pa}]}{101,325}, \tag{A.5}$$

where T_{amb} and P_{amb} are the ambient temperature and pressure.

Thrust required during real flight conditions is higher than during engine testing as measurements are taken bleed off (zero horsepower extraction) [57]. Therefore, a correction factor, scaling the reported fuel flows during engine testing in the EDB, is applied [57, 58]. The magnitude of this correction depends on the flight phase and

an overview is provided in Table A.1.

Table A.1: Fuel flow correction factor values [57]

Flight Phase	Correction Factor
Takeoff	1.010
Climbout	1.013
Approach	1.020
Idle	1.100

The corrected fuel flows are then used to determine the reference values for $\mathrm{EI}_{\mathrm{NO}_x}$ and $\mathrm{EI}_{\mathrm{CO}}$ from the EDB using a (bilinear) logarithmic curve fit [57]. These reference values, $\mathrm{EI}_{\mathrm{NO}_x,\mathrm{SL}}$ and $\mathrm{EI}_{\mathrm{CO,SL}}$, are then converted to in-flight emissions using [57]

$$\mathrm{EI}_{\mathrm{CO,Alt}} = \mathrm{EI}_{\mathrm{CO,SL}} \frac{\theta_{\mathrm{amb}}^{3.3}}{\delta_{\mathrm{amb}}^{1.02}}, \tag{A.6}$$

and

$$\mathrm{EI}_{\mathrm{NO}_x,\mathrm{Alt}} = \mathrm{EI}_{\mathrm{NO}_x,\mathrm{SL}} \sqrt{\frac{\delta_{\mathrm{amb}}^{1.02}}{\theta_{\mathrm{amb}}^{3.3}}} \exp\left[19(h_{\mathrm{SL}} - h_{\mathrm{Alt}})\right]. \tag{A.7}$$

A.1.3 DLR Method

The DLR method is only used to predict NO_x emissions and does not provide relations to estimate CO emissions.

First, a corrected fuel mass flow is computed via [58]

$$\dot{m}_{\mathrm{fuel,ref}} = \frac{\dot{m}_f}{\delta_{\mathrm{total}} \sqrt{\theta_{\mathrm{total}}}}, \tag{A.8}$$

where the total pressure and temperature ratios δ_{total} and θ_{total} are defined as [58]

$$\delta_{\mathrm{total}} = \frac{P_{\mathrm{total}}[\mathrm{Pa}]}{101,325}, \tag{A.9}$$

and

$$\theta_{\mathrm{total}} = \frac{T_{\mathrm{total}}[\mathrm{K}]}{288.15}. \tag{A.10}$$

The total pressure (P_{total}) and temperature (T_{total}) are calculated using [58]

$$P_{\text{total}} = P_{\text{amb}}(1 + 0.2M^2)^{3.5}, \tag{A.11}$$

and

$$T_{\text{total}} = T_{\text{amb}}(1 + 0.2M^2). \tag{A.12}$$

Using the value $\text{EI}_{\text{NO}_x,\text{SL}}$, which is the EI at sea level at the corrected fuel mass flow (again obtained from a curve fit), the EI at cruise is computed as

$$\text{EI}_{\text{NO}_x,\text{Alt}} = \text{EI}_{\text{NO}_x,\text{SL}}\delta_{\text{total}}^{0.4}\theta_{\text{total}}^{3}\exp\left[19(h_{\text{SL}} - h_{\text{Alt}})\right]. \tag{A.13}$$

A.2 Soot

The available soot measurements and prediction methods in the literature are used in two ways. First, model predictions at sea level are compared with a combination of measurements of a CFM56-7B engine and statistical relations using the smoke number. Second, the predicted effects of changing the fuel composition are compared with experiments for a CFM56-7B engine in the literature that applies similar fuel composition changes.

A.2.1 Sea Level Comparison

As previously explained, soot emissions are observed to be highly sensitive to combustor and engine design. Therefore, only specific data for the CFM56-7B is deemed suitable for comparison with model predictions. The experimental data used comes from Brem et al. [49], where soot mass and number EI were measured at six different thrust settings for a range of different fuel compositions. The reported values at the instrument are corrected to the engine exit plane using the provided line loss correction factors.

Furthermore, SN values from the ICAO emissions databank are converted into EI

values using relationships based on correlations between existing measurements and smoke numbers. The two relationships used are First Order Approximation 3 (FOA3) and Smoke Correlation for Particle Emissions CAEP11 (SCOPE11) [24, 138].

FOA3, by Wayson et al. [138], uses two different relations, depending on the magnitude of the smoke number. For smoke numbers less than or equal to 30, it relates the SN to the mass per unit volume through

$$\mathrm{EI}_{\mathrm{soot,mass}} = 0.0694\mathrm{SN}^{1.24}Q, \tag{A.14}$$

which is based on a least-squares fit [138]. For smoke numbers larger than 30, the soot mass EI is calculated using

$$\mathrm{EI}_{\mathrm{soot,mass}} = \left(0.0297\mathrm{SN}^2 - 1.802\mathrm{SN} + 31.94\right) Q. \tag{A.15}$$

Q is the volumetric flow rate per kg of fuel burn through the core [m^3/(kg fuel)], and is estimated by [138]

$$Q = 0.776\mathrm{AFR}(1+\beta) + 0.877, \tag{A.16}$$

where AFR is the air-to-fuel ratio [-] and β is the bypass ratio in the case of internally mixed flow turbofan engines [-]. Since the CFM56-7B does not belong to this category of engines, a β value of zero is used [6].

FOA3 only provides estimates for the soot mass EI and not for the number EI. Therefore, Agarwal et al. [24] developed a new method, estimating both soot mass and number EI. This method is referred to as SCOPE11 and will be used in the development of international standards for soot emissions regulations [24].

In SCOPE11, distinctions are made between three different locations: the measurement instrument (subscript i), the engine exit (subscript e) and the combustor (subscript c). In order to calculate the mass EI, the soot mass concentration at the instrument is first calculated from the reported SN using

$$C_{\text{soot},i} = \frac{648.4 \times 10^3 \exp(0.0766\text{SN})}{1 + \exp[-1.098(\text{SN} - 3.064)]}, \tag{A.17}$$

where, C_{soot} is to the mass concentration of soot [$\mu\text{g/m}^3$]. k_{slm} is a correction factor to convert from the instrument to the engine location and is given by [24]

$$k_{\text{slm}} = \ln\left(\frac{3.219 C_{\text{soot},i}(1+\beta) + 312.5}{C_{\text{soot},i}(1+\beta) + 42.6}\right). \tag{A.18}$$

Next, the soot mass concentration at the combustor exit is calculated using [24]

$$C_{\text{soot},c} = C_{\text{soot},e}(1+\beta)\frac{\rho_{t4}}{\rho_a}, \tag{A.19}$$

where ρ_a is the density of ambient air [kg/m^3] and ρ_{t4} is the total density at the exit of the combustor [kg/m^3], which is computed based on simplified engine cycle calculations described in detail by Agarwal et al. [24]. From the soot concentration at the combustor exit, the EI can be computed from [24]

$$\text{EI}_{\text{soot,mass},c} = C_{\text{soot},c} Q. \tag{A.20}$$

where Q is now calculated using

$$Q = 0.776\text{AFR}(1+\beta) + 0.767, \tag{A.21}$$

In order to compute the number EI, the geometric mean diameter (GMD) is computed first using [24]

$$\text{GMD[nm]} = 5.08 C_{\text{soot},c}^{0.185}. \tag{A.22}$$

Now, the number EI is calculated as follows [24]

$$\text{EI}_{\text{soot,number}} = \frac{6\text{EI}_{\text{soot,mass},c}}{\pi \rho_{\text{soot}} \text{GMD}^3 \exp(4.5 \ln(\sigma)^2)}, \tag{A.23}$$

where a value for the geometric standard deviation σ of 1.8 is assumed [24].

A.2.2 Fuel Composition Effects

The main data source used to evaluate the model predictions in response to changing fuel composition are the experiments conducted by Brem et al. [49]. Here, Jet A-1 is mixed with two versions of one solvent. The first version is the baseline version whether the second one represents the naphthalene depleted solvent. The results of this experiment provide an idea of the sensitivity of soot mass and number EI to aromatics content and the specific role of naphthalene in this. The reason for primarily using the experiments by Brem et al. [49] is that specific attention is given to the effect of naphthalenes, and the CFM56-7B engine is used. The latter is significant given the previously described observation that soot emissions are sensitive to combustor design (and thus engine type).

Less is known about the specific effects of biofuels for the CFM56-7B engine combustor. General experiments, conducted for a range of different engines, have suggested reductions of approximately 25%-60% in mass and 10%-40% in number emissions [47, 50–53].

Bibliography

[1] C. Scherer, "Global market forecast cities, airports & aircraft 2019-2038." https://www.airbus.com/aircraft/market/global-market-forecast.html, 2019.

[2] B. Kärcher, "Formation and radiative forcing of contrail cirrus," *Nature Communications*, vol. 9, no. 1, pp. 1–17, 2018.

[3] S. H. L. Yim, G. L. Lee, I. H. Lee, F. Allroggen, A. Ashok, F. Caiazzo, S. D. Eastham, R. Malina, and S. R. H. Barrett, "Global, regional and local health impacts of civil aviation emissions," *Environmental Research Letters*, vol. 10, no. 3, p. 034001, 2015.

[4] S. D. Eastham and S. R. H. Barrett, "Aviation-attributable ozone as a driver for changes in mortality related to air quality and skin cancer," *Atmospheric Environment*, vol. 144, pp. 17–23, 2016.

[5] A. H. Lefebvre and D. R. Ballal, *Gas Turbine Combustion: Alternative Fuels and Emissions*. CRC press, 2010.

[6] International Civil Aviation Organization (ICAO), "Aircraft engine emissions databank." https://www.easa.europa.eu/domains/environment/icao-aircraft-engine-emissions-databank, 2019.

[7] D. S. Lee, G. Pitari, V. Grewe, K. Gierens, J. E. Penner, A. Petzold, M. J. Prather, U. Schumann, A. Bais, T. Berntsen, *et al.*, "Transport impacts on atmosphere and climate: Aviation," *Atmospheric Environment*, vol. 44, no. 37, pp. 4678–4734, 2010.

[8] J. P. Beck, C. E. Reeves, F. A. A. M. De Leeuw, and S. A. Penkett, "The effect of aircraft emissions on tropospheric ozone in the northern hemisphere," *Atmospheric Environment. Part A. General Topics*, vol. 26, no. 1, pp. 17–29, 1992.

[9] R. Sausen, I. Isaksen, V. Grewe, D. Hauglustaine, D. S. Lee, G. Myhre, M. O. Köhler, G. Pitari, U. Schumann, F. Stordal, *et al.*, "Aviation radiative forcing in 2000: An update on ipcc (1999)," *Meteorologische Zeitschrift*, vol. 14, no. 4, pp. 555–561, 2005.

[10] E. K. Bastress, "Impact of aircraft exhaust emissions at airports," *Environmental Science & Technology*, vol. 7, no. 9, pp. 811–816, 1973.

[11] N. Chandrasekaran and A. Guha, "Study of prediction methods for NO_x emission from turbofan engines," *Journal of Propulsion and Power*, vol. 28, no. 1, pp. 170–180, 2012.

[12] H. C. Mongia and W. G. A. E. Dodds, "Low emissions propulsion engine combustor technology evolution past, present and future," in *24th Congress of International Council of the Aeronautical Sciences, Yokohama, Japan, Aug*, pp. 2004–609, 2004.

[13] D. K. Wasiuk, M. A. H. Khan, D. E. Shallcross, and M. H. Lowenberg, "A commercial aircraft fuel burn and emissions inventory for 2005–2011," *Atmosphere*, vol. 7, no. 6, p. 78, 2016.

[14] Federal Aviation Administration (FAA), "Aircraft noise issues." https://www.faa.gov/about/office_org/headquarters_offices/apl/noise_emissions/airport_aircraft_noise_issues/, 2018.

[15] J. Faber, D. Greenwood, D. Lee, M. Mann, P. M. De Leon, D. Nelissen, B. Owen, M. Ralph, J. Tilston, A. van Velzen, *et al.*, "Lower NO_x at higher altitudes policies to reduce the climate impact of aviation NO_x emission," *CE Delft Solutions for Environment, Economy and Technology*, 2008.

[16] S. Freeman, D. S. Lee, L. L. Lim, A. Skowron, and R. R. De Leon, "Trading off aircraft fuel burn and NO_x emissions for optimal climate policy," *Environmental Science & Technology*, vol. 52, no. 5, pp. 2498–2505, 2018.

[17] N. Cumpsty, D. Mavris, and M. Kirby, "Aviation and the environment: Outlook," tech. rep., International Civil Aviation Organization (ICAO), 2019.

[18] G. M. Faeth and Ü. Ö. Köylü, "Soot morphology and optical properties in nonpremixed turbulent flame environments," *Combustion Science and Technology*, vol. 108, no. 4-6, pp. 207–229, 1995.

[19] B. Martini, "Development and assessment of a soot emissions model for aircraft gas turbine engines," Master's thesis, Massachusetts Institute of Technology, 2008.

[20] H. Omidvarborna, A. Kumar, and D. Kim, "Recent studies on soot modeling for diesel combustion," *Renewable and Sustainable Energy Reviews*, 2015.

[21] B. R. Stanmore, J. Brilhac, and P. Gilot, "The oxidation of soot: a review of experiments, mechanisms and models," *Carbon*, vol. 39, no. 15, pp. 2247–2268, 2001.

[22] H. G. Wagner, "Soot formation—an overview," in *Particulate Carbon*, pp. 1–29, Springer, 1981.

[23] T. Rindlisbacher and S. D. Jacob, "New particulate matter standard for aircraft gas turbine engines," report, International Civil Aviation Organization (ICAO), 2019.

[24] A. Agarwal, R. L. Speth, T. M. Fritz, S. D. Jacob, T. Rindlisbacher, R. Iovinelli, B. Owen, R. C. Miake-Lye, J. S. Sabnis, and S. R. H. Barrett, "SCOPE11 method for estimating aircraft black carbon mass and particle number emissions," *Environmental Science & Technology*, vol. 53, no. 3, pp. 1364–1373, 2019.

[25] B. T. Brem, L. Durdina, F. Siegerist, P. Beyerle, K. Bruderer, T. Rindlisbacher, S. Rocci-Denis, M. G. Andac, J. Zelina, O. Penanhoat, *et al.*, "Effects of fuel aromatic content on nonvolatile particulate emissions of an in-production aircraft gas turbine," *Environmental Science & Technology*, vol. 49, no. 22, pp. 13149–13157, 2015.

[26] C. Grobler, P. J. Wolfe, K. Dasadhikari, I. C. Dedoussi, F. Allroggen, R. L. Speth, S. D. Eastham, A. Agarwal, M. D. Staples, J. Sabnis, *et al.*, "Marginal climate and air quality costs of aviation emissions," *Environmental Research Letters*, vol. 14, no. 11, p. 114031, 2019.

[27] G. Hoek, R. M. Krishnan, R. Beelen, A. Peters, B. Ostro, B. Brunekreef, and J. D. Kaufman, "Long-term air pollution exposure and cardio-respiratory mortality: a review," *Environmental Health*, vol. 12, no. 1, p. 43, 2013.

[28] J. I. Levy, D. Diez, Y. Dou, C. D. Barr, and F. Dominici, "A meta-analysis and multisite time-series analysis of the differential toxicity of major fine particulate matter constituents," *American Journal of Epidemiology*, vol. 175, no. 11, pp. 1091–1099, 2012.

[29] N. A. Janssen, M. E. Gerlofs-Nijland, T. Lanki, R. O. Salonen, F. Cassee, G. Hoek, P. Fischer, B. Brunekreef, and M. Krzyzanowski, "Health effects of black carbon (2012)," tech. rep., World Health Organization (WHO), 2012.

[30] D. S. Lee, D. W. Fahey, P. M. Forster, P. J. Newton, R. C. N. Wit, L. L. Lim, B. Owen, and R. Sausen, "Aviation and global climate change in the 21st century," *Atmospheric Environment*, vol. 43, no. 22-23, pp. 3520–3537, 2009.

[31] M. Stettler, S. Eastham, and S. R. H. Barrett, "Air quality and public health impacts of uk airports. part i: Emissions," *Atmospheric Environment*, vol. 45, no. 31, pp. 5415–5424, 2011.

[32] J. E. Penner, D. H. Lister, D. J. Griggs, D. J. Dokken, and M. McFarland, "Ipcc special report on aviation and the global atmosphere," *Intergovernmental Panel on Climate Change: Geneva, Switzerland*, 1999.

[33] P. Chylek and J. Hallett, "Enhanced absorption of solar radiation by cloud droplets containing soot particles in their surface," *Quarterly Journal of the Royal Meteorological Society*, vol. 118, no. 503, pp. 167–172, 1992.

[34] M. E. J. Stettler, A. M. Boies, A. Petzold, and S. R. H. Barrett, "Global civil aviation black carbon emissions," *Environmental Science & Technology*, vol. 47, no. 18, pp. 10397–10404, 2013.

[35] B. Kärcher and F. Yu, "Role of aircraft soot emissions in contrail formation," *Geophysical Research Letters*, vol. 36, no. 1, 2009.

[36] P. Minnis, D. F. Young, D. P. Garber, L. Nguyen, W. L. Smith, and R. Palikonda, "Transformation of contrails into cirrus during success," *Geophysical Research Letters*, vol. 25, no. 8, pp. 1157–1160, 1998.

[37] U. Burkhardt and B. Kärcher, "Global radiative forcing from contrail cirrus," *Nature Climate Change*, vol. 1, no. 1, pp. 54–58, 2011.

[38] L. Bock and U. Burkhardt, "Contrail cirrus radiative forcing for future air traffic," *Atmospheric Chemistry and Physics (ACP)*, no. 19, pp. 8163–8174, 2019.

[39] U. Burkhardt, L. Bock, and A. Bier, "Mitigating the contrail cirrus climate impact by reducing aircraft soot number emissions," *Climate and Atmospheric Science*, vol. 1, no. 1, pp. 1–7, 2018.

[40] R. H. Moore, M. Shook, A. Beyersdorf, C. Corr, S. Herndon, W. B. Knighton, R. Miake-Lye, K. L. Thornhill, E. L. Winstead, Z. Yu, *et al.*, "Influence of jet fuel composition on aircraft engine emissions: a synthesis of aerosol emissions data from the nasa apex, aafex, and access missions," *Energy & Fuels*, vol. 29, no. 4, pp. 2591–2600, 2015.

[41] T. F. Stocker, D. Qin, G. Plattner, M. Tignor, S. K. Allen, J. Boschung, A. Nauels, Y. Xia, V. Bex, P. M. Midgley, *et al.*, "Climate change 2013: the physical science basis," 2013.

[42] S. Twomey *et al.*, "Pollution and the planetary albedo," *Atmospheric Environment*, vol. 8, no. 12, pp. 1251–1256, 1974.

[43] B. A. Albrecht, "Aerosols, cloud microphysics, and fractional cloudiness," *Science*, vol. 245, no. 4923, pp. 1227–1230, 1989.

[44] K. P. Geigle, J. Zerbs, M. Köhler, M. Stöhr, and W. Meier, "Experimental analysis of soot formation and oxidation in a gas turbine model combustor using laser diagnostics," *Journal of Engineering for Gas Turbines and Power*, vol. 133, no. 12, 2011.

[45] S. W. Radcliffe and J. P. Appleton, "Soot oxidation rates in gas turbine engines," *Combustion Science and Technology*, vol. 4, no. 1, pp. 171–175, 1971.

[46] H. T. Bocklehurst, C. H. Priddin, and J. B. Moss, "Soot predictions within an aero gas turbine combustion chamber," *International Gas Turbine & Aeroengine Congress & Exhibition*, 1997.

[47] M. T. Timko, T. B. Onasch, M. J. Northway, J. T. Jayne, M. R. Canagaratna, S. C. Herndon, E. C. Wood, R. C. Miake-Lye, and W. B. Knighton, "Gas turbine engine emissions—part ii: Chemical properties of particulate matter," *Journal of Engineering for Gas Turbines and Power*, vol. 132, no. 6, 2010.

[48] N. Dickson, "ICAO standards and recommended practices on local air quality." https://www.icao.int/Meetings/ENVSymposium/Pages/Presentations.aspx, 2019.

[49] B. T. Brem, L. Durdina, F. Siegerist, P. Beyerle, K. Bruderer, T. Rindlisbacher, S. Rocci-Denis, M. G. Andac, J. Zelina, O. Penanhoat, *et al.*, "Effects of fuel aromatic content on nonvolatile particulate emissions of an in-production aircraft gas turbine," *Environmental Science & Technology*, vol. 49, no. 22, pp. 13149–13157, 2015.

[50] E. Corporan, M. J. DeWitt, V. Belovich, R. Pawlik, A. C. Lynch, J. R. Gord, and T. R. Meyer, "Emissions characteristics of a turbine engine and research combustor burning a fischer- tropsch jet fuel," *Energy & Fuels*, vol. 21, no. 5, pp. 2615–2626, 2007.

[51] R. H. Moore, K. L. Thornhill, B. Weinzierl, D. Sauer, E. D'Ascoli, J. Kim, M. Lichtenstern, M. Scheibe, B. Beaton, A. J. Beyersdorf, *et al.*, "Biofuel blending reduces particle emissions from aircraft engines at cruise conditions," *Nature*, vol. 543, no. 7645, pp. 411–415, 2017.

[52] A. J. Beyersdorf, M. T. Timko, L. D. Ziemba, D. Bulzan, E. Corporan, S. C. Herndon, R. Howard, R. Miake-Lye, K. L. Thornhill, E. Winstead, *et al.*, "Reductions in aircraft particulate emissions due to the use of fischer–tropsch fuels," *Atmospheric Chemistry and Physics*, vol. 14, no. 1, pp. 11–23, 2014.

[53] H. R. Jonsdottir, M. Delaval, Z. Leni, A. Keller, B. T. Brem, F. Siegerist, D. Schönenberger, L. Durdina, M. Elser, H. Burtscher, *et al.*, "Non-volatile particle emissions from aircraft turbine engines at ground-idle induce oxidative stress in bronchial cells," *Communications Biology*, vol. 2, no. 1, pp. 1–11, 2019.

[54] P. D. Norman, D. H. Lister, M. Lecht, P. Madden, K. Park, O. Penanhoat, C. Plaisance, and K. Renger, "Development of the technical basis for a new emissions parameter covering the whole aircraft operation: Nepair," *European Commission, Final TR G4RD-CT-2000-00182, Brussels, Belgium*, 2003.

[55] N. Rizk and H. Mongia, "Semianalytical correlations for NO_x, co, and uhc emissions," in *Turbo Expo: Power for Land, Sea, and Air*, vol. 78958, p. V003T06A023, American Society of Mechanical Engineers, 1992.

[56] A. M. Danis, B. A. Pritchard, and H. C. Mongia, "Empirical and semi-empirical correlation of emissions data from modern turbopropulsion gas turbine engines," in *ASME 1996 International Gas Turbine and Aeroengine Congress and Exhibition*, American Society of Mechanical Engineers Digital Collection, 1996.

[57] D. DuBois and G. C. Paynter, ""Fuel flow method2" for estimating aircraft emissions," *SAE Transactions*, pp. 1–14, 2006.

[58] M. Schaefer and S. Bartosch, "Overview on fuel flow correlation methods for the calculation of NO_x, co and hc emissions and their implementation into aircraft performance software," *Institut für Antriebstechnik, Köln*, 2013.

[59] H. Pitsch, "Large-eddy simulation of turbulent combustion," *Annual Review of Fluid Mechanics*, vol. 38, pp. 453–482, 2006.

[60] M. E. Mueller and H. Pitsch, "Large eddy simulation of soot evolution in an aircraft combustor," *Physics of Fluids*, vol. 25, no. 11, p. 110812, 2013.

[61] D. L. Allaire, "A physics-based emissions model for aircraft gas turbine combustors," Master's thesis, Massachusetts Institute of Technology, 2006.

[62] C. G. Moniruzzaman and F. Yu, "A 0D aircraft engine emission model with detailed chemistry and soot microphysics," *Combustion and Flame*, vol. 159, no. 4, pp. 1670–1686, 2012.

[63] J. Bisson, P. Seers, M. Huegel, and F. Garnier, "Numerical prediction of gaseous aerosol precursors and particles in an aircraft engine," *Journal of Propulsion and Power*, vol. 32, no. 1, pp. 918–928, 2016.

[64] D. G. Goodwin, R. L. Speth, H. K. Moffat, and B. W. Weber, "Cantera: An object-oriented software toolkit for chemical kinetics, thermodynamics, and transport processes." https://www.cantera.org, 2018. Version 2.4.0.

[65] J. B. Moss, C. D. Stewart, and K. J. Young, "Modeling soot formation and burnout in a high temperature laminar diffusion flame burning under oxygen-enriched conditions," *Combustion and Flame*, 1995.

[66] M. Di Domenico, P. Gerlinger, and M. Aigner, "Development and validation of a new soot formation model for gas turbine combustor simulations," *Combustion and flame*, vol. 157, no. 2, pp. 246–258, 2010.

[67] G. Bulat, E. Fedina, C. Fureby, W. Meier, and U. Stopper, "Reacting flow in an industrial gas turbine combustor: Les and experimental analysis," *Proceedings of the Combustion Institute*, vol. 35, no. 3, pp. 3175–3183, 2015.

[68] A. K. Tolpadi, A. M. Danis, H. C. Mongia, and R. P. Lindstedt, "Soot modeling in gas turbine combustors," in *ASME 1997 International Gas Turbine and Aeroengine Congress and Exhibition*, American Society of Mechanical Engineers Digital Collection, 1997.

[69] G. Blanquart and H. Pitsch, "A joint volume-surface-hydrogen multi-variate model for soot formation," *Combustion Generated Gine Carbonaceous Particles*, pp. 437–463, 2009.

[70] C. A. Schuetz and M. Frenklach, "Nucleation of soot: molecular dynamics simulations of pyrene dimerization," *Proceedings of the Combustion Institute*, vol. 29, no. 2, pp. 2307–2314, 2002.

[71] R. A. Dobbins, R. A. Fletcher, and H. Chang, "The evolution of soot precursor particles in a diffusion flame," *Combustion and Flame*, vol. 115, no. 3, pp. 285–298, 1998.

[72] H. I. Abdel-Shafy and M. S. M. Mansour, "A review on polycyclic aromatic hydrocarbons: source, environmental impact, effect on human health and remediation," *Egyptian Journal of Petroleum*, vol. 25, no. 1, pp. 107–123, 2016.

[73] H. Richter and J. B. Howard, "Formation of polycyclic aromatic hydrocarbons and their growth to soot—a review of chemical reaction pathways," *Progress in Energy and Combustion Science*, vol. 26, no. 4-6, pp. 565–608, 2000.

[74] S. J. Harris and A. M. Weiner, "Surface growth of soot particles in premixed ethylene/air flames," *Combustion Science and Technology*, vol. 31, no. 3-4, pp. 155–167, 1983.

[75] R. L. Speth, C. Rojo, R. Malina, and S. R. H. Barrett, "Black carbon emissions reductions from combustion of alternative jet fuels," *Atmospheric Environment*, vol. 105, pp. 37–42, 2015.

[76] K. G. Neoh, J. B. Howard, and A. F. Sarofim, "Soot oxidation in flames," in *Particulate Carbon*, pp. 261–282, Springer, 1981.

[77] S. Louloudi, *Transported probability density function: modelling of turbulent jet flames*. PhD thesis, Imperial College London (University of London), 2003.

[78] B. Toone, "A review of aero engine smoke emission," in *Combustion in Advanced Gas Turbine Systems*, pp. 271–296, Elsevier, 1968.

[79] P. R. Lindstedt, "Simplified soot nucleation and surface growth steps for non-premixed flames," in *Soot Formation in Combustion*, pp. 417–441, Springer, 1994.

[80] M. A. Schiener and R. P. Lindstedt, "Joint-scalar transported pdf modelling of soot in a turbulent non-premixed natural gas flame," *Combustion Theory and Modelling*, vol. 22, no. 6, pp. 1134–1175, 2018.

[81] S. J. Brookes and J. B. Moss, "Predictions of soot and thermal radiation properties in confined turbulent jet diffusion flames," *Combustion and Flame*, vol. 116, no. 4, pp. 486–503, 1999.

[82] M. E. Mueller, G. Blanquart, and H. Pitsch, "Hybrid method of moments for modeling soot formation and growth," *Combustion and Flame*, vol. 156, no. 6, pp. 1143–1155, 2009.

[83] R. S. Mehta, *Detailed Modeling of Soot Formation and Turbulence–Radiation Interactions in Turbulent Jet Flames*. PhD thesis, Pennsylvania State University, 2008.

[84] F. Gelbard and J. H. Seinfeld, "Simulation of multicomponent aerosol dynamics," *Journal of Colloid and Interface Science*, vol. 78, no. 2, pp. 485–501, 1980.

[85] H. Guo, P. M. Anderson, and P. B. Sunderland, "Optimized rate expressions for soot oxidation by OH and O_2," *Fuel*, vol. 172, pp. 248–252, 2016.

[86] K. J. Syed, C. D. Stewart, and J. B. Moss, "Modelling soot formation and thermal radiation in buoyant turbulent diffusion flames," in *Symposium (International) on Combustion*, vol. 23, pp. 1533–1541, Elsevier, 1991.

[87] Y. An, X. Li, S. Teng, K. Wang, Y. Pei, J. Qin, and H. Zhao, "Development of a soot particle model with pahs as precursors through simulations and experiments," *Fuel*, vol. 179, pp. 246–257, 2016.

[88] J. B. Moss, C. D. Stewart, and K. J. Syed, "Flowfield modelling of soot formation at elevated pressure," in *Symposium (International) on Combustion*, vol. 22, pp. 413–423, Elsevier, 1989.

[89] P. R. Lindstedt, "Simplified soot nucleation and surface growth steps for non-premixed flames," in *Soot Formation in Combustion*, pp. 417–441, Springer, 1994.

[90] A. Garo, J. Lahaye, and G. Prado, "Mechanisms of formation and destruction of soot particles in a laminar methane-air diffusion flame," *Symposium (International) on Combustion*, vol. 21, no. 1, pp. 1023–1031, 1988.

[91] J. B. Moss, C. D. Stewart, and K. J. Young, "Modeling soot formation and burnout in a high temperature laminar diffusion flame burning under oxygen-enriched conditions," *Combustion and Flame*, vol. 101, no. 4, pp. 491–500, 1995.

[92] Z. Wen, S. Yun, M. J. Thomson, and M. F. Lightstone, "Modeling soot formation in turbulent kerosene/air jet diffusion flames," *Combustion and Flame*, vol. 135, no. 3, pp. 323–340, 2003.

[93] American Society for Testing and Materials International, "ASTM D 1655. standard specification for aviation turbine fuels," ASTM West Conshohockan, PA, 2003.

[94] P. W. Atkins, J. De Paula, and J. Keeler, *Atkins' Physical Chemistry*. Oxford University Press, 2018.

[95] A. D'Alessio, A. Barone, R. Cau, A. D'Anna, and P. Minutolo, "Surface deposition and coagulation efficiency of combustion generated nanoparticles in the size range from 1 to 10 nm," *Proceedings of the Combustion Institute*, vol. 30, no. 2, pp. 2595–2603, 2005.

[96] H. Richter, S. Granata, W. H. Green, and J. B. Howard, "Detailed modeling of pah and soot formation in a laminar premixed benzene/oxygen/argon low-pressure flame," *Proceedings of the Combustion Institute*, vol. 30, no. 1, pp. 1397–1405, 2005.

[97] U. Vandsburger, I. Kennedy, and I. Glassman, "Sooting counterflow diffusion flames with varying oxygen index," *Combustion Science and Technology*, vol. 39, no. 1-6, pp. 263–285, 1984.

[98] R. Puri, T. F. Richardson, R. J. Santoro, and R. A. Dobbins, "Aerosol dynamic processes of soot aggregates in a laminar ethene diffusion flame," *Combustion and Flame*, vol. 92, no. 3, pp. 320–333, 1993.

[99] C. P. Fenimore and G. W. Jones, "Oxidation of soot by hydroxyl radicals," *The Journal of Physical Chemistry*, vol. 71, no. 3, pp. 593–597, 1967.

[100] R. Puri, R. J. Santoro, and K. C. Smyth, "The oxidation of soot and carbon monoxide in hydrocarbon diffusion flames," *Combustion and Flame*, vol. 97, no. 2, pp. 125–144, 1994.

[101] H. Ghiassi, D. Lignell, and J. S. Lighty, "Soot oxidation by oh: theory development, model, and experimental validation," *Energy & Fuels*, vol. 31, no. 3, pp. 2236–2245, 2017.

[102] M. Frenklach and H. Wang, "Detailed modeling of soot particle nucleation and growth," in *Symposium (International) on Combustion*, vol. 23, pp. 1559–1566, Citeseer, 1991.

[103] J. Appel, H. Bockhorn, and M. Frenklach, "Kinetic modeling of soot formation with detailed chemistry and physics: laminar premixed flames of C_2 hydrocarbons," *Combustion and Flame*, vol. 121, no. 1-2, pp. 122–136, 2000.

[104] A. Kazakov, H. Wang, and M. Frenklach, "Detailed modeling of soot formation in laminar premixed ethylene flames at a pressure of 10 bar," *Combustion and Flame*, vol. 100, no. 1-2, pp. 111–120, 1995.

[105] F. Tao, V. I. Golovitchev, and J. Chomiak, "A phenomenological model for the prediction of soot formation in diesel spray combustion," *Combustion and Flame*, vol. 136, no. 3, pp. 270–282, 2004.

[106] S. Rigopoulos, "Modelling of soot aerosol dynamics in turbulent flow," *Flow, Turbulence and Combustion*, vol. 103, no. 3, pp. 565–604, 2019.

[107] B. Gunston, *Jane's Aero-Engines*. Jane's Information Group, 2007.

[108] CFM International, "CFM56-7B Engine." https://www.cfmaeroengines.com/engines/cfm56/, 2016.

[109] S. A. Mosier and R. M. Pierce, "Advanced combustion systems for stationary gas turbine engines: volume I. review and preliminary evaluation," *Environmental Protection Agency, Washington, D.C., EPA/600/7-80/017A*, 1980.

[110] S. Samuelsen, "Rich burn, quick-mix, lean burn (RQL) combustor," *The Gas Turbine Handbook*, pp. 227–233, 2006.

[111] J. Li, J. Chen, L. Yuan, G. Hu, and J. Feng, "Flow characteristics of a rich-quench-lean combustor-combined low-emission and high-temperature rise combustion," *International Journal of Aerospace Engineering*, 2019.

[112] J. B. Heywood and T. Mikus, "Parameters controlling nitric oxide emissions from gas turbine combustors," tech. rep., National Aeronautics and Space Administration (NASA), 1973.

[113] G. Sturgess, J. Zelina, D. T. Shouse, and W. Roquemore, "Emissions reduction technologies for military gas turbine engines," *Journal of Propulsion and Power*, vol. 21, no. 2, pp. 193–217, 2005.

[114] Z. Saboohi and F. Ommi, "Emission prediction in conceptual design of the aircraft engines using augmented crn," *The Aeronautical Journal*, vol. 121, no. 1241, pp. 1005–1028, 2017.

[115] Engineering ToolBox, "Specific heat of some common substances." https://www.engineeringtoolbox .com/specific-heat-capacity-d391.html, 2020.

[116] M. F. Jörg Appel, Henning Bockhorn, "Kinetic modeling of soot formation with detailed chemistry and physics: Laminar premixed flames of C_2 hydrocarbons," *Combustion and Flame*, 2000.

[117] E. Ranzi, A. Frassoldati, A. Stagni, M. Pelucchi, A. Cuoci, and T. Faravelli, "Reduced kinetic schemes of complex reaction systems: fossil and biomass-derived transportation fuels," *International Journal of Chemical Kinetics*, vol. 46, no. 9, pp. 512–542, 2014.

[118] G. P. Smith, D. M. Golden, M. Frenklach, N. W. Moriarty, B. Eiteneer, M. Goldenberg, C. T. Bowman, R. K. Hanson, S. Song, J. William C. Gardiner, V. V. Lissianski, and Z. Qin. http://www.me.berkeley.edu/gri_mech/.

[119] W. Yu, K. Tay, F. Zhao, W. Yang, H. Li, and H. Xu, "Development of a new jet fuel surrogate and its associated reaction mechanism coupled with a multistep soot model for diesel engine combustion," *Applied Energy*, vol. 228, pp. 42–56, 2018.

[120] S. Dooley, S. H. Won, J. Heyne, T. I. Farouk, Y. Ju, F. L. Dryer, K. Kumar, X. Hui, C. Sung, H. Wang, *et al.*, "The experimental evaluation of a methodology for surrogate fuel formulation to emulate gas phase combustion kinetic phenomena," *Combustion and Flame*, vol. 159, no. 4, pp. 1444–1466, 2012.

[121] K. Narayanaswamy, H. Pitsch, and P. Pepiot, "A component library framework for deriving kinetic mechanisms for multi-component fuel surrogates: Application for jet fuel surrogates," *Combustion and Flame*, vol. 165, pp. 288–309, 2016.

[122] "Kerosene/jet fuel category assessment document," tech. rep., The American Petroleum Institute Petroleum HPV Testing Group, 2010.

[123] D. Kim, J. Martz, and A. Violi, "A surrogate for emulating the physical and chemical properties of conventional jet fuel," *Combustion and Flame*, vol. 161, no. 6, pp. 1489–1498, 2014.

[124] P. Prakash. personal communication.

[125] E. S. Hendricks and J. S. Gray, "pycycle: A tool for efficient optimization of gas turbine engine cycles," *Aerospace*, vol. 6, no. 8, p. 87, 2019.

[126] J. Hicken, J. Alonso, and C. Farhat, "Introduction to multidisciplinary design optimization: Chapter 6: Gradient-free optimization," tech. rep., Stanford University, 2012.

[127] D. R. Jones, "Direct global optimization algorithm.," *Encyclopedia of Optimization*, vol. 1, no. 1, pp. 431–440, 2009.

[128] D. Finkel, "Direct optimization algorithm user guide," tech. rep., North Carolina State University. Center for Research in Scientific Computation, 2003.

[129] J. Heywood and P. Heywood, *Internal Combustion Engine Fundamentals*. Automative technology series, McGraw-Hill Education, 1988.

[130] D. W. Naegeli and C. A. Moses, "Effect of fuel molecular structure on soot formation in gas turbine engines," in *ASME 1980 International Gas Turbine Conference and Products Show*, American Society of Mechanical Engineers Digital Collection, 1980.

[131] A. Beyersdorf and B. Anderson, "An overview of the NASA alternative aviation fuel experiment (AAFEX)," *TAC-2 Proc*, pp. 21–32, 2009.

[132] M. T. Timko, S. C. Herndon, E. De La Rosa Blanco, E. C. Wood, Z. Yu, R. C. Miake-Lye, W. B. Knighton, L. Shafer, M. J. DeWitt, and E. Corporan, "Combustion products of petroleum jet fuel, a fischer–tropsch synthetic fuel, and a biomass fatty acid methyl ester fuel for a gas turbine engine," *Combustion Science and Technology*, vol. 183, no. 10, pp. 1039–1068, 2011.

[133] "ICAO annex 16: Environmental protection, volume II–aircraft engine emissions," tech. rep., International Civil Aviation Organization (ICAO), 2017.

[134] N. R. Marchionna, L. A. Diehl, and A. M. Trout, "Effect of inlet-air humidity, temperature, pressure, and reference mach number on the formation of oxides of nitrogen in a gas turbine combustor," tech. rep., National Aeronautics and Space Administration (NASA), 1973.

[135] J. P. Rusnak and J. H. Shadowen, "Development of an advanced annular combustor," tech. rep., National Aeronautics and Space Administration (NASA), 1969.

[136] P. Donovan and T. Cackette, "The Effects of Ambient Conditions on Gas Turbine Emissions—Generalized Correction Factors," *Journal of Engineering for Power*, vol. 100, pp. 640–646, 10 1978.

[137] J. Moore, "The effects of atmospheric moisture on nitric oxide production," *Combustion and Flame*, vol. 17, no. 2, pp. 265–267, 1971.

[138] R. L. Wayson, G. G. Fleming, and R. Iovinelli, "Methodology to estimate particulate matter emissions from certified commercial aircraft engines," *Journal of the Air & Waste Management Association*, vol. 59, no. 1, pp. 91–100, 2009.